89/50

EISCAT SCIENTIFIC ASSOCIATION

EISCAT
TECHNICAL
NOTE

PROCEEDINGS OF THE EISCAT SUMMER SCHOOL

Tromsö, Norway, Aug. 1986

Editors

Cesar La Hoz
Asgeir Brekke

KIRUNA
Sweden

Proceedings of the EISCAT summer school

Tromsö, Norway, Aug. 1986

Editors

Cesar La Hoz
Asgeir Brekke

EISCAT Scientific Association
Box 812, S-981 28 Kiruna
Sweden
September 1989
EISCAT Technical Note 89/50
Printed in Sweden
ISSN 0349-2710

THE EISCAT SUMMER SCHOOL 1986

The University of Tromsö organized the first EISCAT summer school in June, 1975, made possible through a grant from The Nordic Council. The school was a great success and many of the participants at that time are now active scientists in the EISCAT community.

A solar cycle later it was felt that a new generation had grown up in Scandinavia, who were potential users of the EISCAT facility. Thanks to a new grant from The Nordic Council, The University of Tromsö was able to arrange the second EISCAT summer school in Aug. 1986.

The following is a collection of some of the tutorial lectures given during the school. We thank all the lecturers for their contribution to the success of the school and a special thanks is given to the EISCAT staff at Ramfjordmoen who helped the students to get their first experience with performing their own experiments.

Cesar La Hoz *Asgeir Brekke*

Proceedings of the EISCAT summer school

Tromsö, Norway, Aug. 1986

Contents *Page*

Björnå, N.	Effects of Suprathermal Particles on the plasma lines	7
Fontaine, D.	EISCAT Experiments of Elevation Scan (CP-3): Examples of Investigations of the Auroral Electrodynamics	31
Jörgensen, T.S.	High Latitude Problems to be studied by Incoherent Scatter Radars	51
Kelley, J.	The Sondrestrom Incoherent Scatter Radar Facility	77
Kofman, W.	Data Analysis	93
Nygrén, T.	On the Theory of Sporadic E	105
Schmidt, W.	Radar Software for Tristatic Incoherent Scatter Experiments	123

EFFECTS OF SUPRATHERMAL PARTICLES ON THE PLASMA LINES

N. Bjørnå
The Auroral Observatory
University of Tromsø
N-9001 TROMSØ
Norway

Abstract

A review is given of the theory of the enhancement effects of suprathermal particles on the plasma lines of the incoherently scattered spectrum. The theory is followed by numerical calculations showing the effects of a given photoelectron flux and the effects from an incident proton beam with its induced secondary electron population. The calculations are carried out for the EISCAT UHF and VHF radars under relevant ionospheric conditions, with the suprathermal particle fluxes represented by a power-law dependence on energy.

1. INTRODUCTION

In an ionospheric incoherent scatter experiment most of the returned power lies in the ion-line component of the frequency spectrum. The much smaller amount of power contained in the plasma lines makes this component difficult to observe. The ratio of the effective scattering cross section of the thermal plasma line, σ_p^{th}, to that of the ion line, σ_i, is

$$\sigma_p^{th}/\sigma_i \approx \frac{1}{2}\,\alpha^2 \qquad (1)$$

where

$$\alpha^2 \equiv K^2\lambda_D{}^2 = K^2\varepsilon_o\kappa T_e/N_e e^2 \qquad (2)$$

is a small number. K is the wave number of the scattering wave, λ_D is the electron Debye length, T_e is the electron temperature, and N_e is the electron number density. The thermal plasma line is the spectrum of density fluctuations of thermal (Maxwellian) electrons with energies typically in the range 0.02-0.25 eV.

Suprathermal particles are fast particles not belonging to the Maxwellian distribution, with energies greater than the thermal energies. In the low and mid latitude ionosphere these suprathermal particles are photoelectrons created by solar EUV radiation. In the auroral ionosphere there are in addition the precipitating protons and electrons, and the secondary electrons produced by these precipitating particles. Table I lists the types of suprathermal particles together with their main energy domains.

Table I. Suprathermal particles and their main energy domains.

SUPRATHERMAL PARTICLES	TYPICAL ENERGIES
Precipitating electrons	2-20 keV
Precipitating protons	1-100 keV
Secondary electrons	1-100 eV
Photoelectrons	1-30 eV

The importance of suprathermal particles for plasma-line observations is due to the fact that the presence of a small number of such particles may substantially enhance the plasma-line power above its thermal level. Thus, a relative density of suprathermal particles of only 10^{-6} - 10^{-5} can cause enhancements of 1-2 orders of magnitude. The mechanism is one of wave-particle interaction, where the particles interacting with the plasma wave along <u>K</u> are those having a velocity component in this direction, $v_{||}$, matching the phase velocity of the wave, v_φ:

$$v_{||} \approx v_\varphi = \omega_r/K \tag{3}$$

where ω_r is the plasma-line resonance frequency. It follows from Eq. (3) that the upshifted plasma line (ω_r positive) is influenced by a downward particle flux and the downshifted line (ω_r negative) by an upward flux.

Corresponding to the phase velocity in (3) one defines the "phase energy" of the plasma wave, E_φ, by

$$E_\varphi \equiv \frac{1}{2} m v_\varphi^2 \tag{4}$$

where m is the particle mass. Table II gives plasma-wave phase energies for electrons and protons for typical ionospheric densities, in the case of backscatter with the EISCAT UHF (933 MHz) and VHF (224 MHz) radars.

Table II. Phase energies of electrons and protons for backscatter with the EISCAT radars. N_e is the electron density (in m^{-3}) and f_p is the corresponding plasma frequency.

	ELECTRONS		PROTONS	
	N_e = 1.E11 $f_p \approx$ 3 MHz	N_e = 1.E12 $f_p \approx$ 9 MHz	N_e = 1.E11 $f_p \approx$ 3 MHz	N_e = 1.E12 $f_p \approx$ 9 MHz
UHF	0.66 eV	6.6 eV	1.2 keV	12 keV
VHF	11.5 eV	115 eV	21 keV	210 keV

Clearly, the suprathermal particles must have energies exceeding the phase energy in order to enhance the plasma lines. On the other hand, particles with energies much greater than E_φ will not be effective in producing an enhancement, since there will usually be very few of them having the proper parallel velocity required by Eq. (3). It follows from Tables I and II that precipitating electrons have too high energies to have any direct effect on the plasma lines, whereas precipitating protons, secondary electrons, and photoelectrons have energies in the proper range. Photoelectron enhanced plasma lines have been reported for various low and mid latitude radars (e.g. Perkins et al., 1965; Yngvesson and Perkins, 1968; Fremouw et al., 1969; Evans and Gastman, 1970; Cicerone and Bowhill, 1971; Wickwar, 1971; Vidal-Madjar et al., 1975) and also for the EISCAT UHF radar (Kofman et al., 1982; Folkestad et al., 1983; Bjørnå and Kirkwood, 1986). Enhancement by secondary electrons has been observed with the Chatanika radar (Wickwar, 1978; Kofman and Wickwar, 1980).

Since precipitating protons are present in the ionosphere only as a downward directed flux they will only contribute to the upshifted plasma line. Proton enhanced plasma lines have not yet been observed. As will become clear from the numerical simulations presented in Section 4, such observations would require a VHF radar in the auroral zone, like the EISCAT VHF radar. The proton enhancement phenomenon may be viewed in the following way (Bjørnå et al., 1982). When subject to the electric field of the radar beam only electrons due to their smaller mass will be effective reradiators. The protons do not reradiate themselves but are effective in producing electron correlations in the plasma. The role of the protons is similar to that played by the thermal ions in the case of the ion-line spectrum, where the scattering signal is due to electrons making up the Debye screening polarization clouds of the ions.

2. OUTLINE OF THEORY

In the following we give an outline of the theory leading to the formulas for the plasma-line enhancement effects and a qualitative discussion of these effects.

2.1 Effects of suprathermal electrons

Consider a collisionless electron plasma and the case of backscatter along the magnetic field. The differential incoherent scattering cross section, $d^2\sigma/d\Omega d\omega$, takes the simple form (Sheffield, 1975)

$$d^2\sigma/d\Omega d\omega \propto f_e(\omega/K) \; / \; K \cdot |D(\underline{K},\omega)|^2 \tag{5}$$

where ω and $\underline{K}$ are the frequency and wave vector shifts, D is the plasma dispersion function, and f_e is the one-dimensional velocity distribution for electrons along $\underline{K}$. In the neighbourhood of the plasma line resonance frequency ω_r the right hand side of (5) can be approximated by (Perkins and Salpeter, 1965)

$$I(\omega) = \frac{f_e(v_\varphi)/K}{\frac{4}{\omega_r^2}(\omega-\omega_r)^2 + \left[\pi\left(\frac{\omega_{pe}}{K}\right)^2 \left(\frac{d}{dv} f_e(v)\right)_{v_\varphi}\right]^2} \tag{6}$$

where $\omega_{pe} \equiv (N_e e^2/m_e \varepsilon_o)^{\frac{1}{2}}$ is the plasma frequency. The first term in the denominator in (6) results from expanding the real part of D about ω_r, while the second term is the imaginary part of D. The intensity of the plasma line, I_p, we find by integrating $I(\omega)$ over the frequency range about ω_r. We assume that the Landau damping is weak and that the velocity distribution f_e is basically Maxwellian but with a high-energy tail representing suprathermal electrons. The result is

$$I_p = \frac{1}{2}\alpha^2 \frac{C_m f_m(v_\varphi) + C_s f_s(v_\varphi)}{C_m f_m(v_\varphi) - C_s \frac{v_{th}^2}{v_\varphi}\left(\frac{d}{dv} f_s(v)\right)_{v_\varphi}} \tag{7}$$

where f_m denotes the normalized Maxwellian velocity distribution of ambient electrons and f_s is the normalized velocity distribution for suprathermal electrons. C_m and C_s denote the fractional concentrations of Maxwellian electrons and suprathermal electrons, respectively ($C_m + C_s = 1$). $v_{th} \equiv (\kappa T_e/m_e)^{\frac{1}{2}}$ is the electron thermal velocity.

Eq. (7) can be generalized to include the effects of electron collisions. The importance of these effects depends on the ionospheric conditions and on the radar wave length. Fokker-Planck theory has been used to discuss the effects of Coulomb collisions (Perkins and Salpeter, 1965). At low altitudes electron-neutral collisions are important (Oran et al., 1981; Newman and Oran, 1981), which can be represented by a BGK type collision term in the Boltzmann equation. The differential scattering cross section in this case gets slightly more complicated than the collisionless cross section but can be integrated in the same way to give the plasma-line intensity (Newman and Oran, 1981). The result is

$$I_p = \frac{1}{2}\alpha^2 \frac{C_m f_m(v_\varphi) + C_s f_s(v_\varphi) + \chi}{C_m f_m(v_\varphi) - C_s \frac{v_{th}^2}{v_\varphi}\left(\frac{d}{dv} f_s(v)\right)_{v_\varphi} + \chi} \tag{8}$$

with

$$\chi \equiv \frac{v_{th}^2}{v_\varphi^4} \frac{\nu_e}{\pi K}, \tag{9}$$

where ν_e is the electron collision frequency. Note that the effect of including collisions is simply that of adding the new term χ in the numerator and denominator in (8).

The first terms in the numerator and denominator of Eq. (8) represent the collisionless excitation and damping effects of the ambient electrons. Similarly, the second terms describe the collisionless excitation and damping due to suprathermal electrons. The term χ describes the effects of electron collisions on the plasma-line intensity.

In the absence of suprathermal electrons Eq. (8) reduces to the familiar result $I_p = \frac{1}{2}\alpha^2$ for the intensity of the thermal plasma line. When there are suprathermal electrons present whose velocity along $\underline{K}$ matches the phase velocity v_φ there is a possible enhancement. A large enhancement will result if the suprathermal excitation term is the dominating term in the numerator in (8) and at the same time the suprathermal damping is weak. If the suprathermal tail to the distribution function dominates both the excitation and the damping the enhancement ratio is seen to be inversely proportional to the logarithmic derivative of f_s at the phase velocity. Finally, when the collisional term χ dominates there will be no enhancement.

2.2 Effects of precipitating protons

Consider a plasma consisting of thermal and suprathermal electrons as well as suprathermal protons, and consider again the case of backscatter along the magnetic field. The thermal ions we know do not contribute to the plasma line and can be safely omitted. Also we can neglect proton collisions. If we assume that also electron collisions can be neglected the differential scattering cross section has the form (Sheffield, 1975)

$$d^2\sigma/d\Omega d\omega \propto \frac{|1-Z_p(\underline{K},\omega)|^2 f_e(\omega/K) + |Z_e(\underline{K},\omega)|^2 C_p f_p(\omega/K)}{K\cdot|D(\underline{K},\omega)|^2} \tag{10}$$

in which f_e and f_p are the normalized one-dimensional velocity distributions for electrons and protons along $\underline{K}$, $C_p \equiv N_p/N_e$ is the fractional concentration of protons, and

$$D(\underline{K},\omega) \equiv 1 - Z_e(\underline{K},\omega) - Z_p(\underline{K},\omega) \ ,$$

$$Z_j(\underline{K},\omega) \equiv \frac{\omega_{pj}^2}{K^2} \int_L \frac{\underline{K}\cdot(\partial/\partial\underline{v})F_j(\underline{v})}{\underline{K}\cdot\underline{v}-\omega}\, d^3\underline{v} \qquad (j = e,p) \tag{11}$$

where ω_{pj} and F_j denote the plasma frequency and normalized three-dimensional distribution function for particle species j. L denotes the Landau contour.

At the plasma-line frequency the proton contribution to the dispersion function, $Z_p(\underline{K},\omega)$, is usually negligible compared with the electron contribution, $Z_e(\underline{K},\omega)$ (Bjørnå et al., 1982). Thus, when suprathermal protons are present in the ionosphere they produce secondary electrons whose number density is of the same order of magnitude as that of the protons and whose velocity distribution is very similar to the proton distribution, having about the same slope at the phase velocity. It follows from (11) that in the source region of secondary electrons the contribution from the protons is smaller than that of the secondary electrons by a factor of the order of the electron to the proton mass. Hence, we set $Z_p \approx 0$. If we further assume that the electron Landau damping is weak we have $|Z_e| \approx 1$. With these simplifications the differential cross section can be integrated in the same way as in Section 2.1, and taking into account also the effects of electron collisions we get

$$I_p = \frac{1}{2}\alpha^2 \frac{C_m f_m(v_\varphi) + C_s f_s(v_\varphi) + C_p f_p(v_\varphi) + \chi}{C_m f_m(v_\varphi) - C_s \frac{v_{th}^2}{v_\varphi}\left(\frac{d}{dv} f_s(v)\right)_{v_\varphi} + \chi} \tag{12}$$

with χ defined by (9). The proton contribution is thus proportional to the number of protons with parallel velocity matching the phase velocity of the plasma wave. These protons are fully Debye screened by electrons which are responsible for the scattered signal with a Doppler shift corresponding to the proton parallel velocity v_φ. Since the precipitating protons are present only as a downward flux they will contribute only to the upshifted plasma line.

3. POWER-LAW DISTRIBUTION

For the quantitative discussion of the effects of suprathermal particles we shall choose to represent them by so-called power-law distribution functions to be introduced in the following.

Theoretical calculations as well as numerous rocket and satellite observations indicate that the differential directional flux of suprathermal particles, $J(E,\theta)$, varies approximately with energy according to a power-law dependence,

$$J(E,\theta) = CE^{-\gamma}P(\theta) \tag{13}$$

within a certain limited energy range $E_1 \leqq E \leqq E_2$ (cf. e.g., Stamnes and Rees, 1983; Banks et al., 1974; Wrenn, 1974; Søraas et al., 1974; Bjørnå et al., 1982). C and γ are positive constants and $P(\theta)$ is the pitch-angle distribution a general form of which is $P(\theta) = |\cos\theta|^n$ with n an integer. The corresponding normalized velocity distribution function is

$$F(\underline{v}) = \frac{m}{v^2}\frac{1}{N}\,CE^{-\gamma}|\cos\theta|^n\,, \qquad E_1 \leqq E \leqq E_2 \tag{14}$$

with $E \equiv \frac{1}{2} mv^2$. m is the particle mass and N is the number density for particles in the given energy interval. As an example of a power-law differential flux we show in Fig. 1 the energy dependence for a proton flux measured in a rocket experiment (Søraas et al., 1974). The pitch-angle distribution in this case was almost isotropic over the downward hemisphere.

For backscatter along the magnetic field all integrals involved in the calculation of the scattering cross section can be performed analytically when γ is an integer or half integer (Bjørnå and Trulsen, 1986). In particular, Eq. (14) can be integrated over the velocity components perpendicular to the magnetic field to give the one-dimensional distribution function in the field direction. We quote the result for the isotropic case ($n = 0$; $0 \leqq \theta \leqq \pi$):

$$f(v_{\parallel}) = \frac{q-1}{q} \, \frac{1}{v_1^{1-q} - v_2^{1-q}} \cdot \begin{cases} v_1^{-q} - v_2^{-q} , & |v_{\parallel}| \leqq v_1 \\ |v_{\parallel}|^{-q} - v_2^{-q}, & v_1 < |v_{\parallel}| \leqq v_2 \end{cases} \qquad (15)$$

where $v_1 \equiv (2E_1/m)^{\frac{1}{2}}$, $v_2 \equiv (2E_2/m)^{\frac{1}{2}}$, and $q \equiv 2\gamma$, $(\gamma \neq \frac{1}{2})$. We also give the integral

$$\int \frac{\partial F(\underline{v})}{\partial v_{\parallel}} \, d^2 \underline{v}_{\perp} = - \frac{(q-1) v_{\parallel}}{v_1^{1-q} - v_2^{1-q}} \cdot \begin{cases} v_1^{-q-2} - v_2^{-q-2} , & |v_{\parallel}| \leqq v_1 \\ |v_{\parallel}|^{-q-2} - v_2^{-q-2}, & v_1 < |v_{\parallel}| \leqq v_2 \end{cases} \qquad (16)$$

appearing in the plasma dispersion function (cf. Eq. (11)). It should be noted that this quantity does not equal $df(v_{\parallel})/dv_{\parallel}$, due to the fact that the integration limits in (16) depend on $v_{\parallel}$. Hence, for the power-law distribution the derivative appearing in the denominators in Eqs. (7), (8), and (12) has to be replaced by the integral (16).

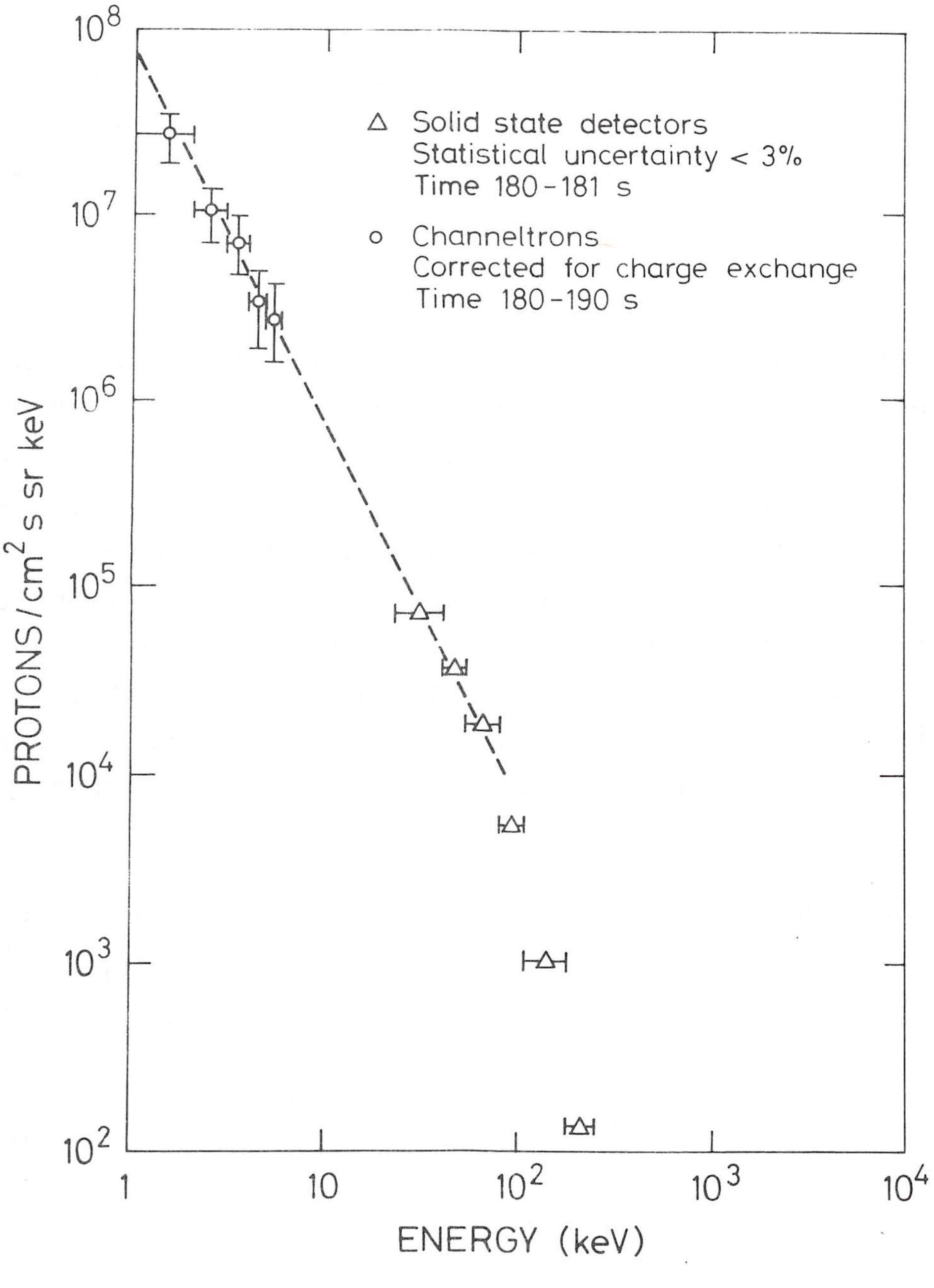

Figure 1. Energy dependence of differential proton flux at 220 km (Søraas et al., 1974). $C = 8 \cdot 10^7$, $\gamma = 2$ (cf. Eq. (13)).

4. NUMERICAL CALCULATIONS

Below we present the results of full numerical calculations of the effects on the plasma line from a photoelectron flux and from an incident proton beam and the secondary electrons produced by this beam. The calculations apply to ionospheric conditions relevant for the EISCAT radars.

4.1 Photoelectrons

The power-law photoelectron flux parameters we have used in the calculations are listed in Table III. They have been derived from theoretical energy spectra given by Stamnes and Rees (1983). We have approximated the spectra by a flat ($\gamma = 0.5$) low-energy part plus a much steeper ($\gamma = 2.5$) high-energy part. The pitch-angle distribution has been taken to be isotropic. For the ambient electrons we have used parameter values taken from an EISCAT experiment in July 1984 (Bjørnå and Kirkwood, 1986). They represent typical daytime values as measured by EISCAT in the summer season.

Table III. Photoelectron flux parameters for various altitudes, as derived from the spectra given by Stamnes and Rees (1983). At each altitude the spectrum has been approximated by the sum of two fluxes of the form of Eq. (13).

Altitude km	C $(\mathrm{cm}^2\ \mathrm{s\ sr\ keV})^{-1}$	γ	Energy range eV
125	$1.76 \cdot 10^9$	0.5	0.6 - 2.0
	$1.50 \cdot 10^4$	2.5	2.0 - 60
140	$8.56 \cdot 10^9$	0.5	0.9 - 2.0
	$3.90 \cdot 10^4$	2.5	2.0 - 60
200	$8.56 \cdot 10^9$	0.5	1.5 - 7.0
	$7.80 \cdot 10^4$	2.5	7.0 - 60
300	$8.56 \cdot 10^9$	0.5	1.5 - 7.0
	$7.80 \cdot 10^4$	2.5	7.0 - 60

Fig. 2 (a)-(d) shows the results for four different altitudes with the VHF (224 MHz) plasma lines to the left and the UHF (933 MHz) plasma lines to the right in each panel. For the UHF radar we show both the thermal and the enhanced lines. For the VHF radar the thermal line is extremely narrow, due to the very weak Landau damping, and cannot be resolved in the figure except at the lowest altitude 125 km where the width is determined by electron-neutral collisional damping. Only the high-energy part of the photoelectron flux is effective in producing the enhancement in the VHF case, since the phase energy of plasma waves at VHF wave lengths lies well above the upper limit of the low-energy flux given in Table III.

At 125 km the enhancement ratios are about the same for the two radars. The dominating excitation term in Eq. (8) is the photoelectron contribution $C_s f_s$. For the VHF radar the damping is controlled by the collision term χ while for the UHF radar the χ-term and the photoelectron damping term are about the same size. At higher altitudes the thermal Landau damping becomes important for the UHF line as the Debye length increases with height. At the same time the photoelectron excitation becomes less dominant. Thus, at 200 km the excitation terms $C_m f_m$ and $C_s f_s$ in (8) are close to being equal while $C_m f_m$ is the dominating damping term. This prevents any significant enhancement of the UHF line above 200 km. For the VHF radar the parameter $K^2 \lambda_D{}^2$ is small enough at all altitudes so that the term $C_m f_m$ is negligible both with respect to excitation and damping. The enhancement ratio which lies between 30 and 40 above 140 km is much greater than for the UHF line. However, at 140 km the intensity of the enhanced VHF line is smaller than that of the UHF line by a factor of 5, due to the much smaller intensity of the thermal VHF line. At 200 and 300 km it is larger by a factor of 2-3. Thus, under the ionospheric conditions on which we have based our calculations the VHF system seems to be preferable

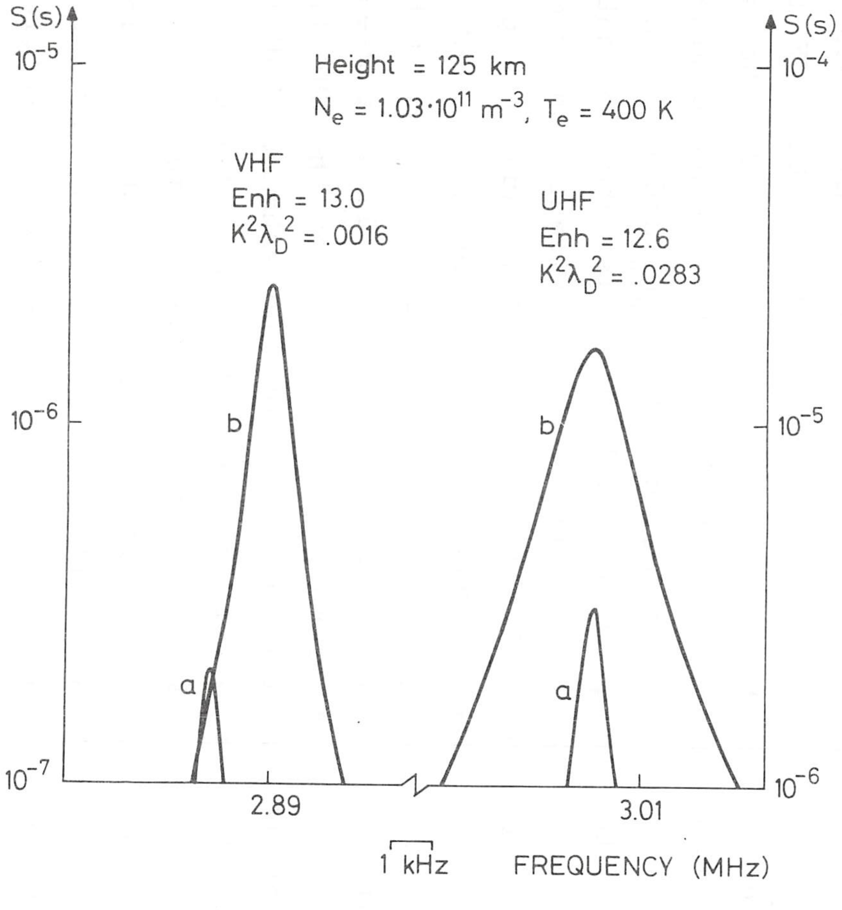
S(s)
10^-5
10^-6
10^-7
S(s)
10^-4
10^-5
10^-6
Height = 125 km
N_e = 1.03·10^11 m^-3, T_e = 400 K
VHF
Enh = 13.0
K^2λ_D^2 = .0016
UHF
Enh = 12.6
K^2λ_D^2 = .0283
b
a
b
a
2.89
3.01
1 kHz
FREQUENCY (MHz)

(a)

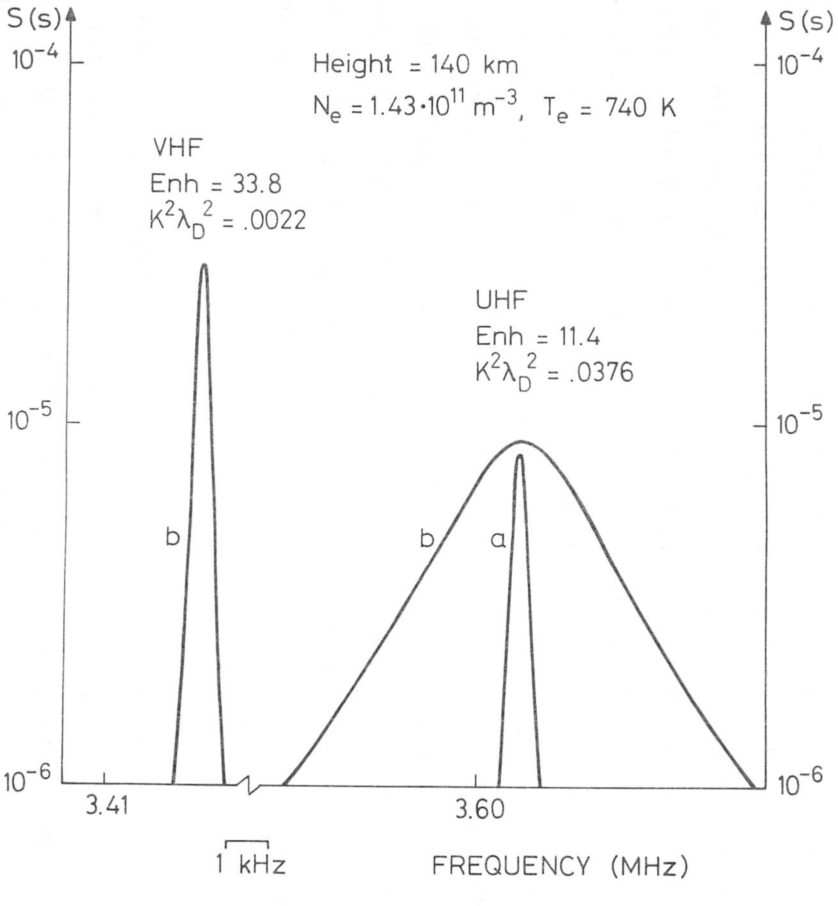
S(s)
10^-4
10^-5
10^-6
S(s)
10^-4
10^-5
10^-6
Height = 140 km
N_e = 1.43·10^11 m^-3, T_e = 740 K
VHF
Enh = 33.8
K^2λ_D^2 = .0022
UHF
Enh = 11.4
K^2λ_D^2 = .0376
b
b
a
3.41
3.60
1 kHz
FREQUENCY (MHz)

(b)

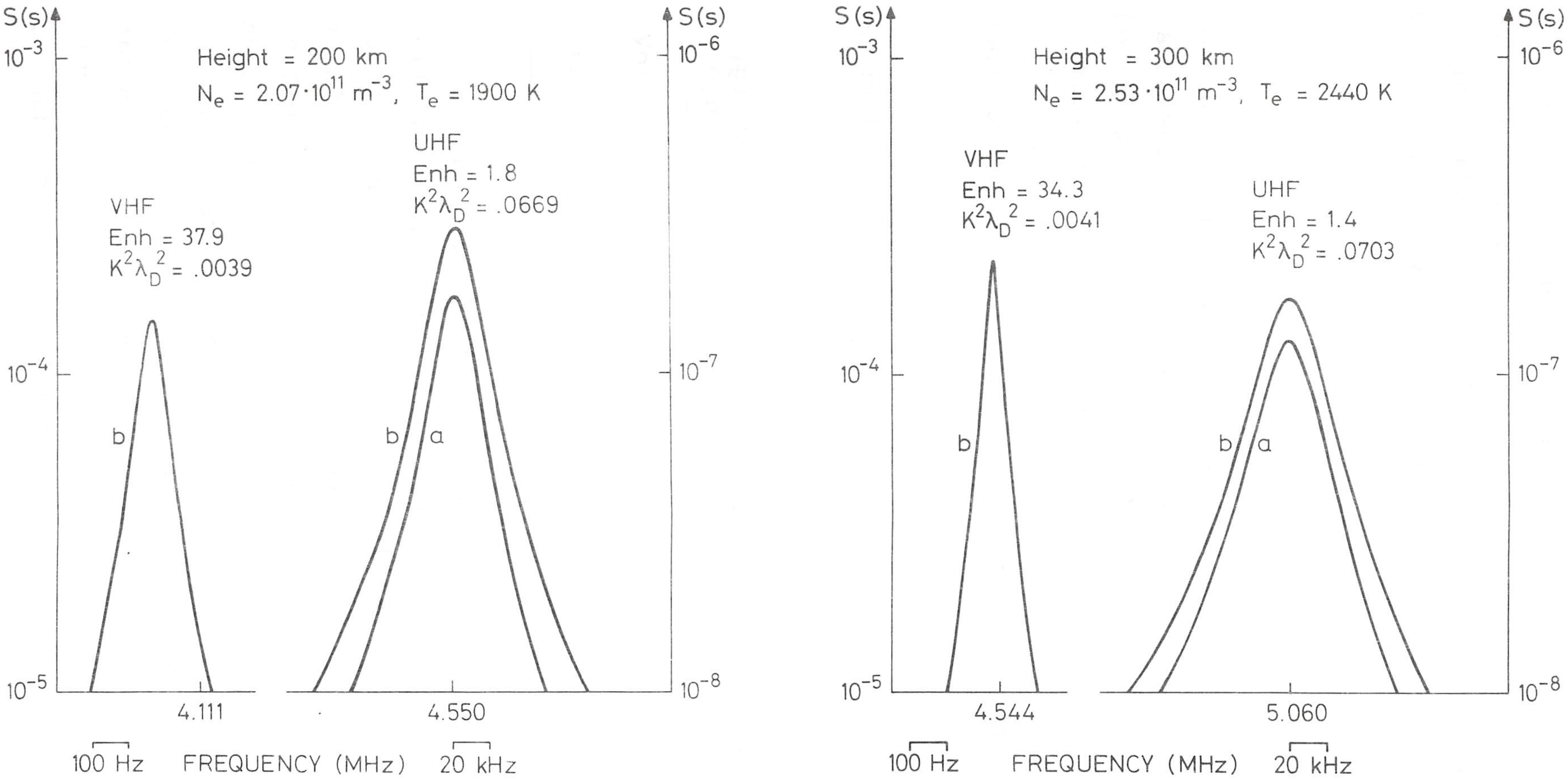

(c)

(d)

Figure 2. Effects of photoelectrons on the plasma line cross section. Flux parameters are given in Table III. a: Thermal cross section, b: enhanced cross section. Enh is the enhancement ratio, K the length of the scattering wave vector and λ_D the electron Debye length. N_e and T_e is the density and temperature of thermal electrons, respectively. $S \equiv (\sqrt{\pi}/N_e r_o^2)(d^2\sigma/d\Omega d\omega)$.

above 200 km while the UHF system can be used successfully below this height. Our calculated UHF intensities are in good agreement with the plasma-line intensities which were actually observed under these conditions (Bjørnå and Kirkwood, 1986).

4.2 Protons and secondary electrons

Table IV lists the flux parameters for the measured proton beam shown in Fig. 1. Also given in Table IV are the parameters for the induced secondary electron flux calculated with the incident proton beam as the primary source (Bjørnå et al., 1982). The proton pitch-angle distribution we take to be isotropic over the downward hemisphere (see Søraas et al., 1974).

Table IV. Proton flux parameters and secondary electron flux parameters at 200 km altitude.

	C $(\mathrm{cm}^2\ \mathrm{s\ sr\ keV})^{-1}$	γ	Energy range
Protons	$8.00 \cdot 10^7$	2.0	5-100 keV
Secondary electrons	$1.34 \cdot 10^7$	1.5	3-30 eV

Figs. 3 and 4 show the effects of these fluxes on the up-shifted plasma line at 200 km altitude. The curves labelled *a* are the thermal plasma lines, curves *b* show the effects of the proton beam alone, and curves *c* show the joint effects of protons and secondary electrons. The pitch-angle distribution of the secondary electrons has been assumed isotropic, which is a reasonable assumption at this altitude. For the VHF calculations in Fig. 3 we have adopted the same set of parameter values for the ambient electrons as in Fig. 2(c). For the UHF radar there would be no enhancement effects under these conditions, due to

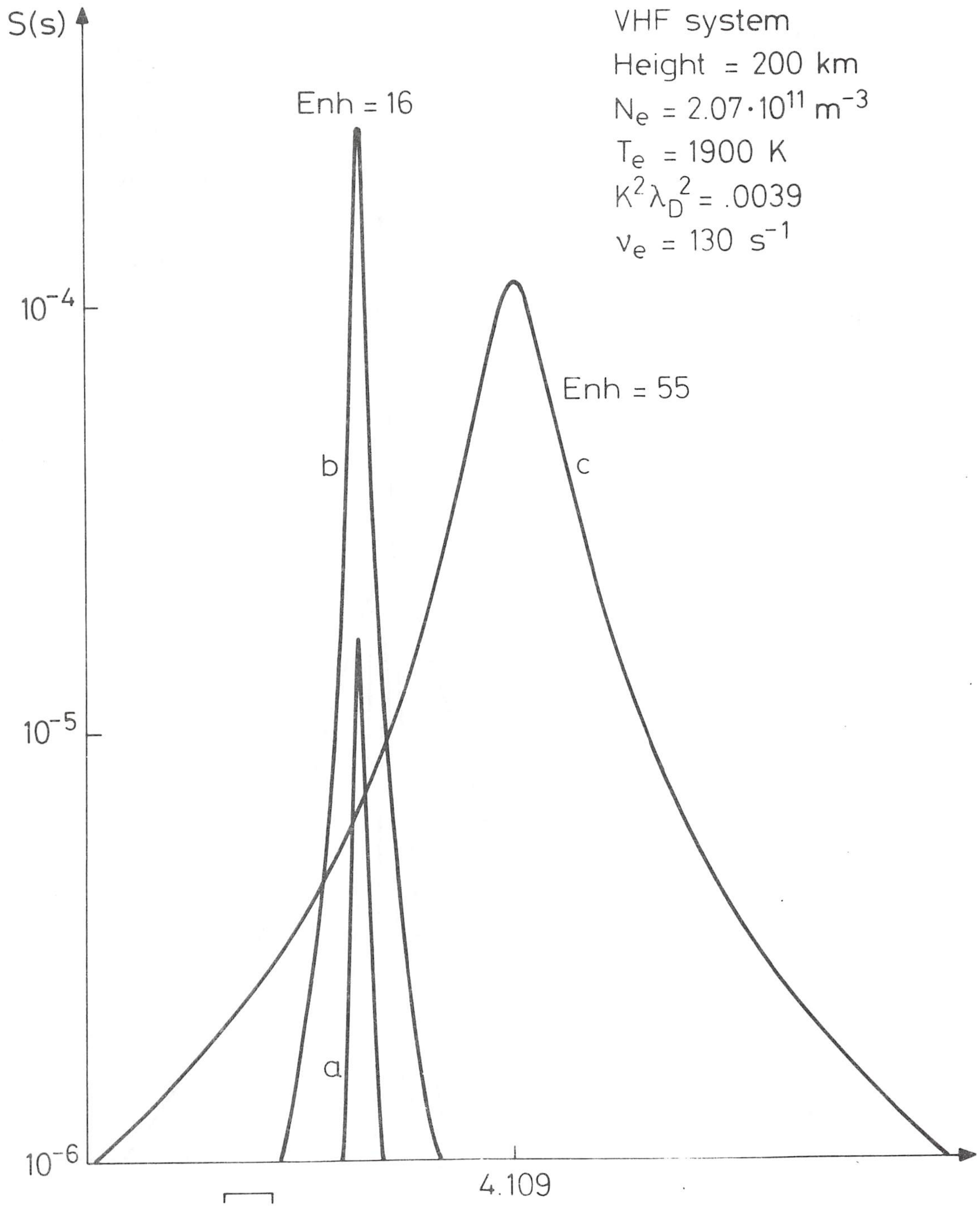

Figure 3. Effects of proton flux and induced secondary electron flux on the upshifted VHF plasma line at 200 km. a: Thermal line, b: effects of proton beam alone, c: joint effects of protons and secondary electrons. ν_e is the electron collision frequency. Flux parameters are given in Table IV.

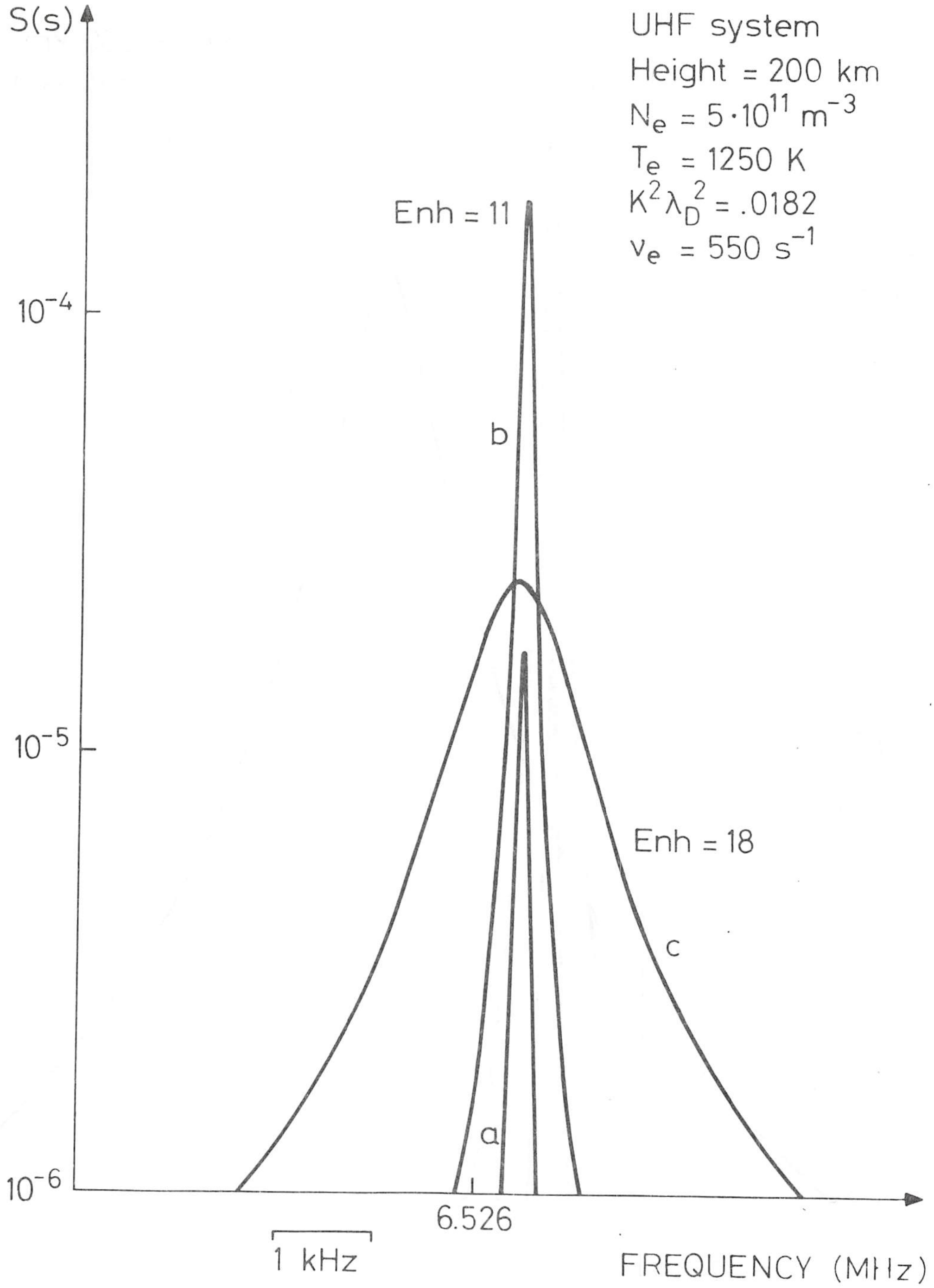

Figure 4. Effects of proton flux and induced secondary electron flux on the upshifted UHF plasma line at 200 km. a: Thermal line, b: effects of proton beam alone, c: joint effects of protons and secondary electrons. Flux parameters are given in Table IV.

the strong Landau damping. However, when the electron density is increased and the temperature decreased as in Fig. 4 the Debye length becomes small enough that there is a significant effect on the UHF line. One striking feature present in Figs. 3 and 4 is that the protons contribute only to the excitation and not to the damping while the secondary electrons contribute to both. The increase in damping caused by the secondary electrons, which shows up as a broadening of the plasma line, has the effect of eliminating the proton enhancement. Thus the joint effects of protons and secondary electrons shown by curves *c* are essentially the effects that would be produced by the secondary electrons alone. The direct effects of the precipitating protons are thus completely masked by the effects of the secondary electrons they produce.

Fig. 5 shows the upshifted plasma line at a scattering height of 500 km. The secondary electron flux now can be assumed to be upwards directed, since we are well above the main source region of these electrons. So they have no effect on the upshifted plasma line. The proton beam, which is taken to be the same as at 200 km, in this case produces a 75 fold increase in the intensity. The enhanced intensity amounts to about 90% of the corresponding ion-line intensity. Since the ion line is easily observed we believe it should be possible to detect the proton excited plasma line under the conditions assumed in Fig. 5. The experiment should be run at a time when there can be no contributions from photoelectrons. In particular, one must avoid the effects of photoelectrons incident from the conjugate point. So the conjugate hemisphere should not be sunlit.

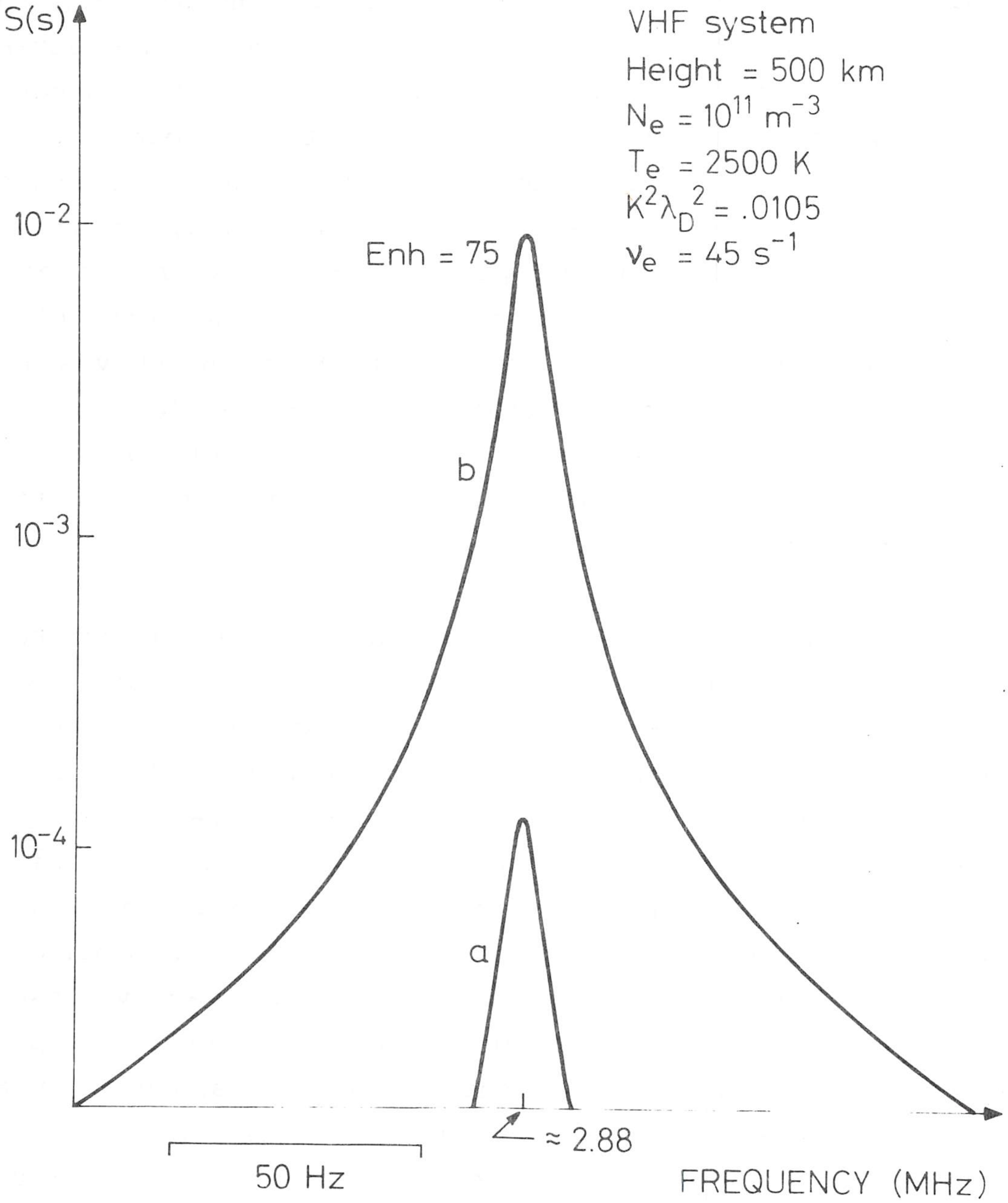

Figure 5. Effects of proton flux on the upshifted VHF plasma line at 500 km. a: Thermal line, b: enhanced line. Flux parameters are given in Table IV.

5. CONCLUSION

We have discussed the enhancement effects of suprathermal particles on the plasma lines in an ionospheric incoherent scatter experiment. The discussion includes an outline of the general theory together with numerical calculations demonstrating the effects of photoelectrons, secondary electrons and precipitating protons. The calculations have been carried out for ionospheric conditions relevant for the EISCAT radars, with the suprathermal particles represented by distribution functions of power-law form.

We have limited our discussion to the case of a monostatic radar looking up along the geomagnetic field. The generalization of the results in Section 2.1 to include scattering geometries with the wave vector shift at an angle with the magnetic field has been given by Yngvesson and Perkins (1968).

REFERENCES

Banks, P.M., Chappell, C.R., and Nagy, A.F. 1974. A new model for the interaction of auroral electrons with the atmosphere: spectral degradation, backscatter, optical emission, and ionization, J. Geophys. Res. 79, 1459.

Bjørnå, N., Havnes, O., Jensen, J.O., and Trulsen, J. 1982. Enhancement of the incoherent scattering plasma lines due to precipitating protons and secondary electrons, Physica Scripta 25, 632.

Bjørnå, N. and Kirkwood, S. 1986. Observations of natural plasma lines in the E region and lower F region with the EISCAT UHF radar, Ann. Geophysicae 4 A, 137.

Bjørnå, N. and Trulsen, J. 1986. Effect of a power law particle flux on the ionospheric incoherent scattering cross section, Physica Scripta 33, 284.

Cicerone, R.J. and Bowhill, S.A. 1971. Photoelectron fluxes measured at Millstone Hill, Radio Sci. 6, 957.

Evans, J.V. and Gastman, I.J. 1970. Detection of conjugate photoelectrons at Millstone Hill, J. Geophys. Res. 75, 807.

Folkestad, K., Hagfors, T., and Westerlund, S. 1983. EISCAT: An updated description of technical characteristics and operational capabilities, Radio Sci. 18, 867.

Fremouw, E.J., Petriceks, J., and Perkins, F.W. 1969. Thomson scatter measurements of magnetic field effects on the Landau damping and excitation of plasma waves, Phys. Fluids 12, 869.

Kofman, W., Lejeune, G., Bauer, P., Folkestad, K., and Hagfors, T. 1982. EISCAT first plasma-line experiment, Ann. Géophys. 38, 461.

Kofman, W. and Wickwar, V.B. 1980. Plasma line measurements at Chatanika with high-speed correlator and filter bank, J. Geophys. Res. 85, 2998.

Newman, A.L. and Oran, E.S. 1981. The effects of electron-neutral collisions on the intensity of plasma lines, J. Geophys. Res. 86, 4790.

Oran, E.S., Wickwar, V.B., Kofman, W., and Newman, A. 1981. Auroral plasma lines: A first comparison of theory and experiment, J. Geophys. Res. 86, 199.

Perkins, F. and Salpeter, E.E. 1965. Enhancement of plasma density fluctuations by nonthermal electrons, Phys. Rev. 139 A, 55.

Perkins, F.W., Salpeter, E.E., and Yngvesson, K.O. 1965. Incoherent scatter from plasma oscillations in the ionosphere, Phys. Rev. Letters 14, 579.

Sheffield, J. 1965. Plasma scattering of electromagnetic radiation, Sect. 6.3, Academic, New York.

Stamnes, K. and Rees, M.H. 1983. Inelastic scattering effects on photoelectron spectra and ionospheric electron temperature, J. Geophys. Res. 88, 6301.

Søraas, F., Lindalen, H.R., Måseide, K., Egeland, A., Sten, T.A., and Evans, D.S. 1974. Proton precipitation and the Hβ emission in a postbreakup auroral glow. J. Geophys. Res. 79, 1851.

Vidal-Madjar, D., Kofman, W., and Lejeune, G. 1975. Mesures de la raie de plasma par diffusion incohérente à Nançay, et premiers résultats morphologiques, Ann. Géophys. 31, 227.

Wickwar, V.B. 1971. Photoelectrons from the magnetic conjugate point studied by means of the 6300 Å predawn enhancement and the plasma-line enhancement, Ph.D. thesis, Rice Univ., Houston, Tex.

Wickwar, V.B. 1978. Plasma lines in the auroral E layer, J. Geophys. Res. 83, 5186.

Wrenn, G.L. 1974. Satellite measurements of photoelectron fluxes, Ann. Géophys. 30, 49.

Yngvesson, K.O. and Perkins, F.W. 1968. Radar Thomson scatter studies of photoelectrons in the ionosphere and Landau damping, J. Geophys. Res. 73, 97.

EISCAT EXPERIMENTS OF ELEVATION SCAN (CP-3) : EXAMPLES OF INVESTIGATIONS OF THE AURORAL ELECTRODYNAMICS

Dominique Fontaine
CRPE/CNET, Observatoire de St. Maur
4, avenue de Neptune, 94107 St. Maur Cedex, France.

Abstract

EISCAT experiments of elevation scan were designed to explore the latitudinal structure of the auroral ionosphere. Some examples taken from recent studies of electrodynamics of the auroral plasma are chosen to illustrate the capabilities of this operating mode, the derivation of physical parameters from radar measurements, and the discussion of the results.

1. INTRODUCTION

Since the first experiments of the European Incoherent Scatter radar EISCAT at the fall of 1981, a large amount of time was devoted to the mode of elevation scan operated as well as a Common Programme (CP-3) as similar Special Programmes. Involving antenna motions approximately in the magnetic meridian plane, these experiments were designed to explore the latitudinal structure of the ionospheric layer.

An exhaustive review of the results obtained in different fields (neutral atmosphere, ion composition, plasma dynamics...) is clearly out of the scope of this brief report. We made the choice to concentrate upon one topic alone: the electrodynamics of the auroral plasma. Already widely investigated, it is actually best suited to be tackled with EISCAT due to its major advantage over other radars to observe the plasma flow in 3-dimensions. In particular, the distribution at the planetary-scale of electric fields and plasma flow forms the subject of section 3. The study of the large-scale morphology of the auroral ionosphere is pursued in section 4 by the investigation of the signature of the electric current system. Finally, section 5 deals with auroral structures of smaller scale. It reports the electrodynamic behaviour of the plasma and the current circulation inferred from the observation of a stable auroral arc. Before going into the details of these examples, section 2 briefly summarizes the geometry of the elevation scan experiments.

2. GEOMETRY OF THE ELEVATION SCAN EXPERIMENTS

The tristatic U.H.F. system of EISCAT sounds the auroral ionospheric layer from about 80 km up to more than 600 km of altitude. The height-profiles of plasma density and temperatures are deduced from line-of-sight power and spectral measurements performed from the transmitting-receiving system at Tromsö (Norway). In addition of the backscattered signal recorded at Tromsö, two other antennae equipped with a receiving system at Kiruna (Sweden) and Sodankyla (Finland) intercept the Tromsö beam, providing a measurement of three components of the ion drift at the intersection point (Folkestadt et al.,1983).

The considered experiments of elevation scan were designed to explore the latitudinal structure of the ionosphere in addition of the vertical sounding just mentioned. The antenna motion is programmed to describe a set of fixed positions approximately aligned along the magnetic meridian, and then to come back to the first position. The large-scale studies are well supported by the experiments of extended scanning from North to South of the radar, covering in 1/2 hour a latitudinal range of about 10° with 0°.5 to 1° resolution. In contrast, the experiments suitable to the description of smaller scale structures require rather limited scans over a latitudinal range of 1° or 2°, but with a much thiner horizontal resolution typically 0.1° and also a better time resolution (the total cycle duration is typically 10 minutes).

3. PLANETARY-SCALE DISTRIBUTION OF ELECTRIC FIELDS AND PLASMA FLOW

3.1. Ion velocity measurements

This first study is entirely based on three-dimension measurements of ion velocities in F-region. The top diagram of Figure 1 displays an example of velocity distribution in an ionospheric map of the northern hemisphere between 75° (inner circle) and 60° (outer circle) of invariant latitude. The experiment started on 26 January 1982 at about 18:00 MLT (Magnetic Local Time) in an extended scanning mode and was running for 24 hours.

Such maps are not to be regarded as an instantaneous picture of the plasma flow but rather as a convenient representation, built one scan after the other over a period of 24 hours. However, on that day, the magnetic conditions approached the stationary state as indicated by the magnetic activity index Kp slightly fluctuating around 3. In consequence, the time dependence of the data being estimated to be small in first approximation, the map appears as essentially representative of the spatial distribution of the plasma flow. The pattern reproduces the usual plasma motion of sunward convection from the nightside through the evening and morning sectors. On occasion, early in the morning and in the afternoon, the flow intensity increases.

3.2. Electric field pattern over the auroral zone

In F-region , where the electromagnetic effects strongly dominate the effects of collisions upon neutrals, the convection electric field $\vec{E}$ can be directly computed from the ion velocity $\vec{V}_i$ by the following relationship (where $\vec{B}$ is the magnetic field) :

$$\vec{E} = -\vec{V}_i \times \vec{B}$$

In stationary conditions, the convection electric field can be represented as the gradient of a scalar potential Φ such as :

$$\vec{E} = -\vec{\nabla}\Phi$$

With its capability to measure the 3 components of the velocity vector, the EISCAT radar offers favourable conditions to the description of the electric field and scalar potential pattern. Different methods were developed to extract the potential information from observations of Millstone Hill and Chatanika radars (Evans et al., 1980 ; Foster et al., 1981 ; Holt et al., 1984). The method presented here, and proposed by Alcaydé et al. (1986) for EISCAT data, intends to compute the electrostatic potential distribution over the auroral zone under the assumption of stationarity over 24 hours. Briefly, it assumes that the electric field results from the sum of two contributions :

$$\vec{E} = \vec{E}_\Phi + \vec{E}_\Psi = -\vec{\nabla}\Phi - \vec{B} \times \vec{\nabla}(\Psi/|\vec{B}|)$$

The first contribution represents the electrostatic component to find out and

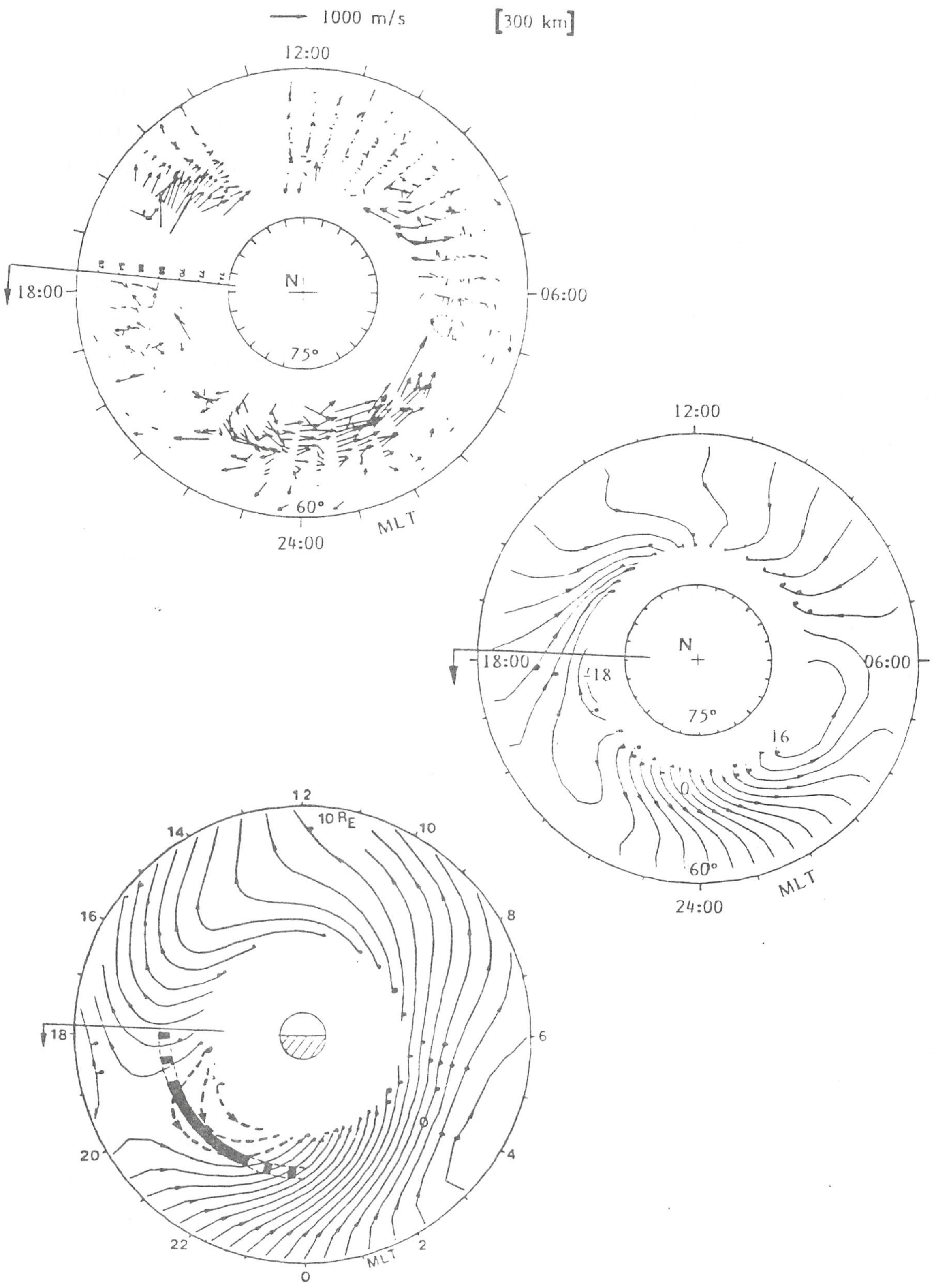

Figure 1. 26 January, 1982. Ionospheric maps of convection velocities measured by EISCAT (top diagram), of the electrostatic convection potential deduced from EISCAT data (middle diagram), and the corresponding magnetospheric projection of the convection and corotation potential (bottom diagram). The orbit of the spacecraft GEOS 2 is indicated by the thick curve.

expected to be dominant. The residual term, depending on a potential Ψ, gives an indication of the variability of the data and therefore constitutes a test on the method and on the assumption of stationarity. A theoretical form is then assumed for the potential Φ as a combination of series of Legendre polynomials (P_n) depending on the latitude Λ and of a Fourier analysis in magnetic local time :

$$\Phi_{th} = \sum_{n=0}^{N} \sum_{m=0}^{M} \Phi_{n,m} P_n(\Lambda) \exp(im\varphi)$$

The coefficients $\Phi_{n,m}$ are computed by fitting to the observed electric field the theoretical electrostatic electric field deduced from Φ_{th}. The same procedure is finally applied to the residual potential Ψ.

The middle diagram of Figure 1 shows, in the same ionospheric representation than the top diagram, the resulting distribution of the electrostatic potential Φ obtained for the considered experiment on 26 January 1982. The equipotential lines trace the flow of the ionospheric plasma. The sunward convection motion over the auroral zone can be clearly evidenced in the form of two vortices located in the morning and evening sectors. The convection intensification observed early in the morning and in the afternoon tends to compress the equipotential lines. The residual potential Ψ, although maximum at these periods of time, remains weak, less than 5% of the potential Φ. This result leads to the conclusion that the global electric field pattern observed over 24 hours on 26/27 January 1982 can be described by a steady state electrostatic potential alone.

3.3. Comparison with simultaneous magnetospheric observations

The last step of this study intends to test the accuracy of the potential pattern derived from EISCAT data by comparison to independent observations. This was achieved by Fontaine et al. (1986) by making use of simultaneous measurements performed by the European geostationary spacecraft GEOS 2 in the equatorial magnetosphere and close to the apex of EISCAT magnetic field line.

The electric field measured in auroral zone is directly transmitted into the equatorial plane along magnetic field lines, generally assumed to be equipotential. However this mapping requires to take precautions. The ionospheric maps are obtained in the frame of reference co-rotating with the Earth, which is the natural frame of reference of ground-based measurements. In contrast, magnetospheric observations are generally discussed relative to the frame of reference fixed relative to the sun. In consequence, the electric field mapping into the equatorial plane should be accompanied by an additional transformation of frame of reference. This can be achieved by taking into account the existence in the equatorial plane of the corotation electric field, which is induced by dragging with the Earth rotation of conducting bodies such as the ionosphere and magnetic field lines. It is expressed as : $\vec{E}_{cor} = - \vec{V}_{cor} \times \vec{B}$, with $\vec{V}_{cor} = \vec{\omega} \times \vec{r}$ where the corotation velocity $\vec{V}_{cor}$ depends on the Earth angular velocity $\vec{\omega}$ and on the radial distance to the Earth center $\vec{r}$.

The bottom diagram of Figure 1 displays the potential pattern resulting from the mapping into the equatorial plane and the transformation of frame of reference in a magnetospheric representation from the Earth's center to a distance of 10 terrestrial radii. Following the predictions of the magnetic field model IGS80, the projection of EISCAT field of view maps over a wide magnetospheric region approximately comprised between 4 to 10 terrestrial radii. The external regions are essentially dominated by the convection transport from the nightside toward the sun. The major part of the flow drifts through the morning sector due to the influence of the eastward corotation motion. Convection through the evening sector can be identified, confined around 18:00 MLT. Inside these external regions, appears in the evening sector between 18:00 MLT and 22:00 MLT an inner region (dashed lines) dominated by the corotation electric field. In fact, the corotation equipotential lines close around the Earth, but in regions inaccessible to the observations. At the boundary between these two regions, the so-called last closed equipotential line separates the closed lines dominated by corotation effects from open lines of sunward convection.

A part of GEOS 2 orbit is plotted in the bottom diagram of Figure 1 by the thick dashed curve. In the evening sector, the spacecraft generally crosses the plasmaspheric bulge filled with cold plasma of ionospheric origin. The location of the cold plasmaspheric plasma detected on that day is indicated by the continuous thick part of the orbit. At both ends, sharp gradients in the plasma density mark the plasmapause crossings.

More accurate magnetic field models (Olson and Pfitzer, 1974 ; Kosik, 1978) were used to compare observations of GEOS 2 and EISCAT. The results reveal that the plasmaspheric bulge coincides with the corotation region and the plasmapause with the last closed equipotential line. This effect, confirmed by other observations, has two consequences :

First, the potential pattern derived from EISCAT data in stationary conditions can be validated by simultaneous and independent observations at least concerning one of its most characteristic features : the plasmasphere/corotation region. This outlines the capability of the radar to produce potential maps of the flow pattern over a wide magnetospheric region from 4 to 10 Earth radii.

Secondly, this result also outlines the close relationship between the distributions of electric fields and plasma in the magnetosphere that can be regarded as responsible for the coincidence observed in stationary conditions. Of course, in more disturbed periods, this coincidence is not expected to occur because of the differences in the respective dynamics of particles and fields.

4. MORPHOLOGY OF THE PLANETARY-SCALE CURRENT SYSTEM

4.1. Current density

The current density flowing in a fluid composed of s species of charged particles, with a density n_s and a charge q_s, is obtained from the relationship :

$$\vec{j} = \sum_s n_s q_s \vec{V}_s$$

The velocity $\vec{V}_s$ of the species s is solution of the momentum equation which can be written in a simple hydrodynamic description neglecting the viscosity term as :

$$n_s m_s \frac{d\vec{V}_s}{dt} = - \vec{\nabla} P + n_s m_s \vec{g} - \sum_t n_s m_s \nu_{st} (\vec{V}_s - \vec{V}_t)$$

$$- n_s m_s \nu_{sN} (\vec{V}_s - \vec{V}_N) + n_s q_s (\vec{E} + \vec{V}_s \times \vec{B})$$

where m_s, ν_{st}, ν_{sN} represent respectively the mass and the collision frequencies of the particles of species s upon other charged particles and upon the neutral component. This equation prescribes the motion of the particles s under the influence of different forces that can be separated in 3 classes depending on their origin (Blanc, 1980) :

The first class includes all internal forces $\vec{I}_s$ of the plasma, namely the inertial-acceleration term on the left-hand side of the momentum equation, and the first terms on the right-hand side : pressure (P) gradients, gravity (g) and collisions upon other charged particles : $\vec{I}_s = n_s m_s \frac{d\vec{V}_s}{dt} + \vec{\nabla} P - n_s m_s \vec{g} + n_s m_s \nu_{st} (\vec{V}_s - \vec{V}_s)$. If the momentum equation were reduced to $\vec{I}_s = 0$, the other terms being neglected, the plasma would behave as an isolated body only submitted to its own internal forces.

Interactions of external origin are contained in the two remaining terms of the momentum equation. The term of collisions upon the neutral fluid constitutes the second class of effects. If it were predominant relative to the other terms, then the momentum equation would simply reduce to : $\vec{V}_s = \vec{V}_N$. The plasma could then be regarded as "frozen" in the neutral fluid drifting at the velocity $\vec{V}_N$.

Finally, the third class of effects, which contains the last term of the momentum equation, expresses the interactions of the plasma with an external electromagnetic field ($\vec{E}$, $\vec{B}$). If now all terms could be neglected relative to the Laplace force, then the momentum equation would be written : $\vec{E} + \vec{V}_s \times \vec{B} = 0$. The plasma, "frozen" in magnetic flux tubes, would drift across magnetic field lines at the electromagnetic velocity : $\vec{V}_s = \vec{E} \times \vec{B}/B^2$.

4.2. Case of the ionospheric plasma

The behaviour of the ionospheric plasma, assumed to be composed of two species of particles, electrons and ions, depends on altitude.

In F-region (above 180 km of altitude about), electromagnetic effects dominate. As already mentioned, all particles drift at the same electromagnetic velocity, (a property already used in section 3), and the current flow across magnetic field line cancels.

In E-region (between 80 km and 180 km of altitude about) the behaviour of electrons is still dominated by the electromagnetic field. This is no more the case for ions : their frequency of collision upon neutrals reaches the same order of magnitude as their gyrofrequency. In consequence, the ion momentum equation (i for ions) expresses the balance of the electromagnetic and collisional effects :

$$n_i q_i \left(\vec{E} + \vec{V}_i \times \vec{B}\right) = n_i m_i \; \nu_{iN} \left(\vec{V}_i - \vec{V}_N\right)$$

A non-zero current density results from the different behaviour of electrons and ions. It is generally written in the following form, known as the ionospheric Ohm's law :

$$j = \overline{\overline{\sigma}} \cdot \left(\vec{E} + \vec{V}_N \times \vec{B}\right)$$

The tensor $\overline{\overline{\sigma}}$ of ionospheric conductivities depends on the plasma density, the collision and cyclotron frequencies.

With a sharp peak of conductivities in the direction perpendicular to $\vec{B}$, the E-region appears as the best conducting layer of the ionosphere. It concentrates the whole current circulation across magnetic field lines. Indeed, the narrow E-layer can be regarded as an element of a large-scale electric circuit connected to the magnetosphere via magnetic field lines. Excellent conductors, magnetic field lines are capable to drive currents diverted from possible accumulation in the ionospheric and magnetospheric circulation perpendicular to the magnetic field. EISCAT observations give access to the ionospheric circuit, and in particular to its large-scale morphology.

In general, the studies about the large-scale current system do not take into account the details of the height-profile of currents across the thin E-layer. They rather focus upon the variations of the horizontal distribution of height-integrated currents. The works reported below achieved this vertical integration from EISCAT measurements under some assumptions mainly : the neutral wind velocity generally small relative to the electromagnetic velocity is neglected ; the electric field component parallel to $\vec{B}$ can be ignored relative to the perpendicular component, generally larger by one order of magnitude, and assumed in addition to be independent of altitude.

The vertical integration of the ionospheric Ohm's law over the conducting E-layer provides an "integrated Ohm's law" relating the integrated perpendicular currents $\vec{J}_\perp$ to the electric field $\vec{E}$:

$$\vec{J}_\perp = \overline{\overline{\Sigma}} \, . \, \vec{E}$$

The coefficients of the integrated conductivity tensor $\overline{\overline{\Sigma}}$ result from the height-integration of the corresponding coefficients of the tensor $\overline{\overline{\sigma}}$. They are computed from EISCAT measurements of the height-profile of electron density in E-region combined with an estimation of the collision frequencies by a model of neutral atmosphere (Alcaydé, 1981). The electric field, independent of altitude, is deduced as in section 3 from ion velocity measurements in F-region.

4.3. EISCAT observations

The top diagram of Figure 2 displays the ionospheric map of integrated perpendicular currents deduced on 16 June 1982 during an extended scan experiment run over 24 hours. Due to the geometry of the elevation scan mode, the latitudinal range accessible to E-region measurements at 100 km of altitude covers 1/3 of the corresponding range in F-region at 300 km of altitude. In consequence, the window of observation of conductivities and thus currents is reduced to 3° of latitude. The diagram reproduces the usual pattern of two electrojets flowing eastward in the evening sector and westward in the morning sector. On 16 June 1982, the current flow exhibits a very asymmetric morphology with a westward electrojet very confined to a few hours early in the morning, and an eastward electrojet covering the whole evening sector.

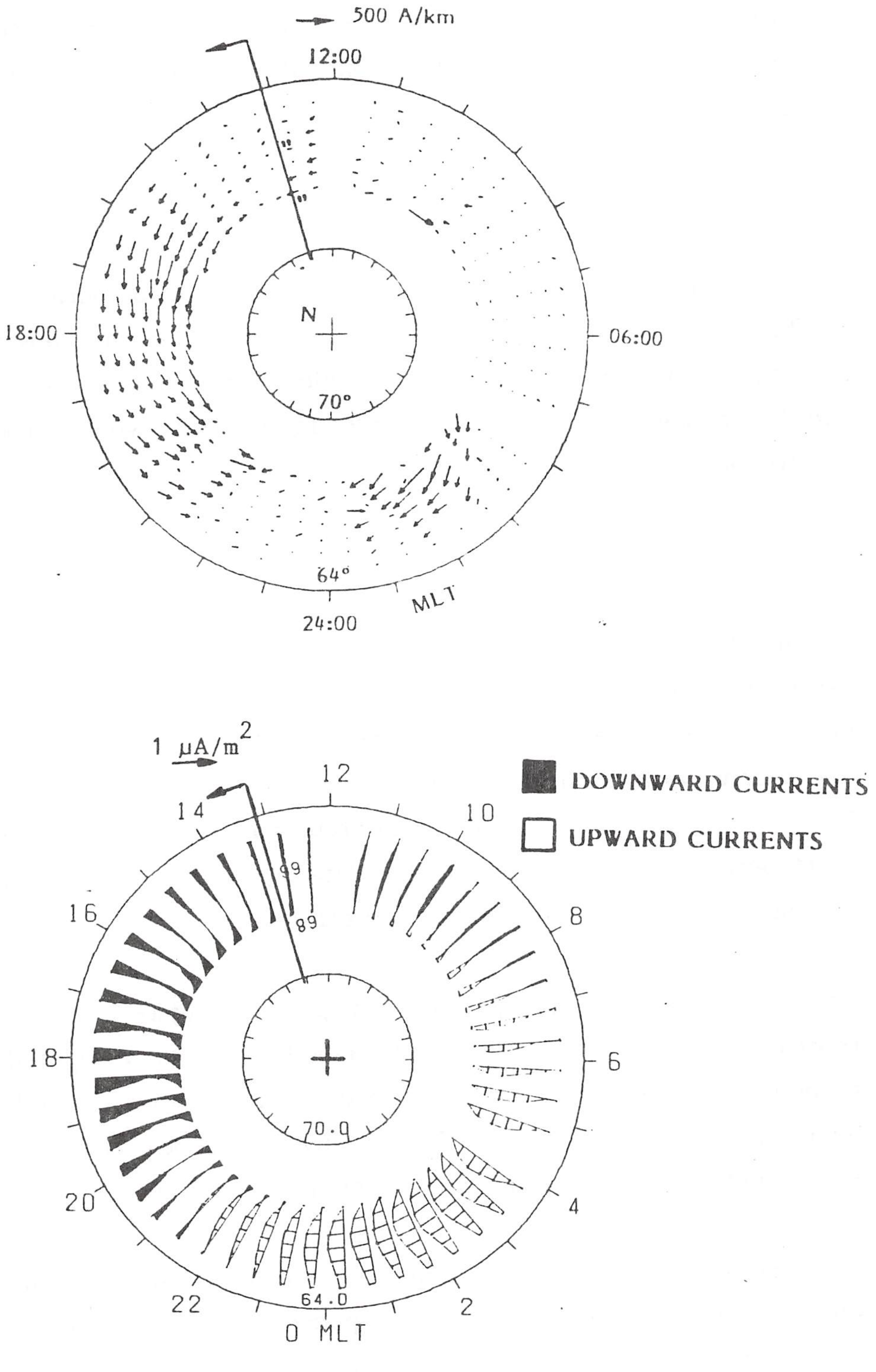

Figure 2. 16 June, 1982. Ionospheric maps of integrated currents perpendicular to the magnetic field (top diagram), and of field-aligned currents (bottom diagram), deduced from EISCAT measurements.

An evaluation of the field-aligned current intensity can be extracted from the equation of charge conservation, which reduces in the absence of temporal variations to :

$$\mathrm{div}\,\vec{j} = 0$$

This equation ensures the local closure of ionospheric currents. Its height-integration over the E-layer under the same assumptions as previously provides the following evaluation of field-aligned currents as a function of the divergence of integrated perpendicular currents (where I represents the inclination of the magnetic field) :

$$j_{//} \sin I = \mathrm{div}\,\vec{J}_{\perp}$$

If magnetic conditions were stationary and thus the data cleared of temporal variations, the spatial derivatives could be computed from successive radar measurements. The chosen experiment on 16 June 1982 approaches the stationarity with a magnetic activity index Kp smoothly fluctuating between 2 and 3. Furthermore, Caudal (1986) proposed to eliminate the variations of short periods of time by fitting the data to the diurnal harmonic variation assumed to originate only from spatial effects.

The results are shown in the bottom diagram of Figure 2 which attempts to represent the intensity of field-aligned currents computed from the perpendicular current distribution of the top panel. In the EISCAT observation window, currents are found to flow downward (black parts) in the afternoon sector and upward (white parts) in the night and morning sectors.

These results were finally compared to the average pattern obtained by Iijima and Potemra (1978) from data of the spacecraft TRIAD in quiet to moderate magnetic conditions ($AE < 100\gamma$). The radar observations satisfactorily agree in morphology as well as in intensity with the equatorward part of the current system defined by Iijima and Potemra. This tends to validate the quality of information deduced from EISCAT data.

5. ELECTRODYNAMIC ENVIRONMENT OF AURORAL STRUCTURES OF SMALLER SCALE : CASE OF STABLE AURORAL ARCS

The collision of magnetospheric particles with the upper atmosphere of the Earth, the so-called precipitation process, is responsbible for auroral light emissions by exciting atomic and molecular constituents of the atmosphere. In addition of such spectacular visible phenomena, the precipitating particles also contribute to the local ionization of the upper layers of the atmosphere. The resulting increase of electron density and ionospheric conductivities can in particular be observed by incoherent scatter facilities, which also provide the description of the corresponding electrodynamic environment.

This section reports a case study performed by Girard and Senior (1986) from EISCAT data and devoted to auroral structures elongated (1000 km or more) and relatively narrow (of the order of 10 km), that the authors denominated by the general term of "stable arcs". They are characterized by intense light emissions associated with a strong increase of E-region electron density, lasting for long time periods (10 minutes and more)

5.1. EISCAT observations

The EISCAT radar was operated in a limited scan mode adapted to the observations of these stable auroral arcs : each scan, completed within 20 minutes, covers a latitudinal range limited to 2° in F-region with a good space resolution of 3 km and 10 km respectively in E- and F-regions.

The experiment performed on 11 March 1984 reveals the presence of two stable arcs observed in the field of view of the radar during 3 successive scans (1 hour) at about the same location. As further investigations have pointed out a similar electrodynamic behaviour during each scan, the results concerning one scan alone (20:45 UT/21:02 UT) are reported here. The two top panels of Figure 3 display the latitudinal variation of basic electrodynamic parameters computed from E-region electron density and F-region ion velocity measurements following the same procedure as in section 4. The two sharp enhancements in the height-integrated Hall and Pedersen conductivities indicate the presence of two arcs centered at about 66° and 66°3 invariant latitude. This two-arc system is associated with fluctuations of large amplitude and strongly correlated of both northward and eastward components of the electric field. At the extreme latitudes of the scan only accessible to F-region measurements, the fluctuations become smoother, which may indicate the background state of the ionosphere outside the arcs.

5.2. Frame of reference of the arc system

In general, theoretical approaches to problems of generation and development of auroral arcs describe the electrodynamic behaviour of the plasma in the frame of reference of the arc. A first attempt to organize EISCAT observations then requires the knowledge of the arc orientation. Hereafter, the arc coordinate system in the plane perpendicular to the magnetic field $\vec{B}$ will be labelled (x, y) with x in the direction normal to the arc and y in the direction parallel.

In the absence of optical measurements, the arc orientation can be determined from Maxwell's equations applied to EISCAT measurements. The quasi-stationarity of the two arc structure, suggested by similar observations over one hour, reduces the Faraday's law to the simple form : curl $\vec{E} = 0$. In the arc coordinate system, it is written as follows : $(\partial E_y/\partial x) - (\partial E_x/\partial y) = 0$. If the assumption of uniformity inside the arc structure holds, gradients along the arc in the y direction vanish $(\partial/\partial y = 0)$. It then comes : $\partial E_y/\partial x = 0$. This equation means the conservation across the arc structure of the electric field component tangent to the arc direction. This essential property permits to determine the arc orientation which was found in the present case to be rotated by 42° away from the L-shell in the northeast-southwest direction (Girard and Senior, 1986).

The latitudinal variation of the electric field components normal and tangent to the arc are shown in the bottom panel of Figure 3. As expected, the tangent component remains constant throughout the two-arc structure, which supports a posteriori the assumption of uniformity. In constrast, the normal component exhibits large fluctuations.

5.3. Quantitative picture of the arc current system

The current circulation associated to the arc structure is investigated in the arc coordinate system from the ionospheric Ohm's law and the charge conservation equation integrated over the conducting E-layer, as in Section 4.

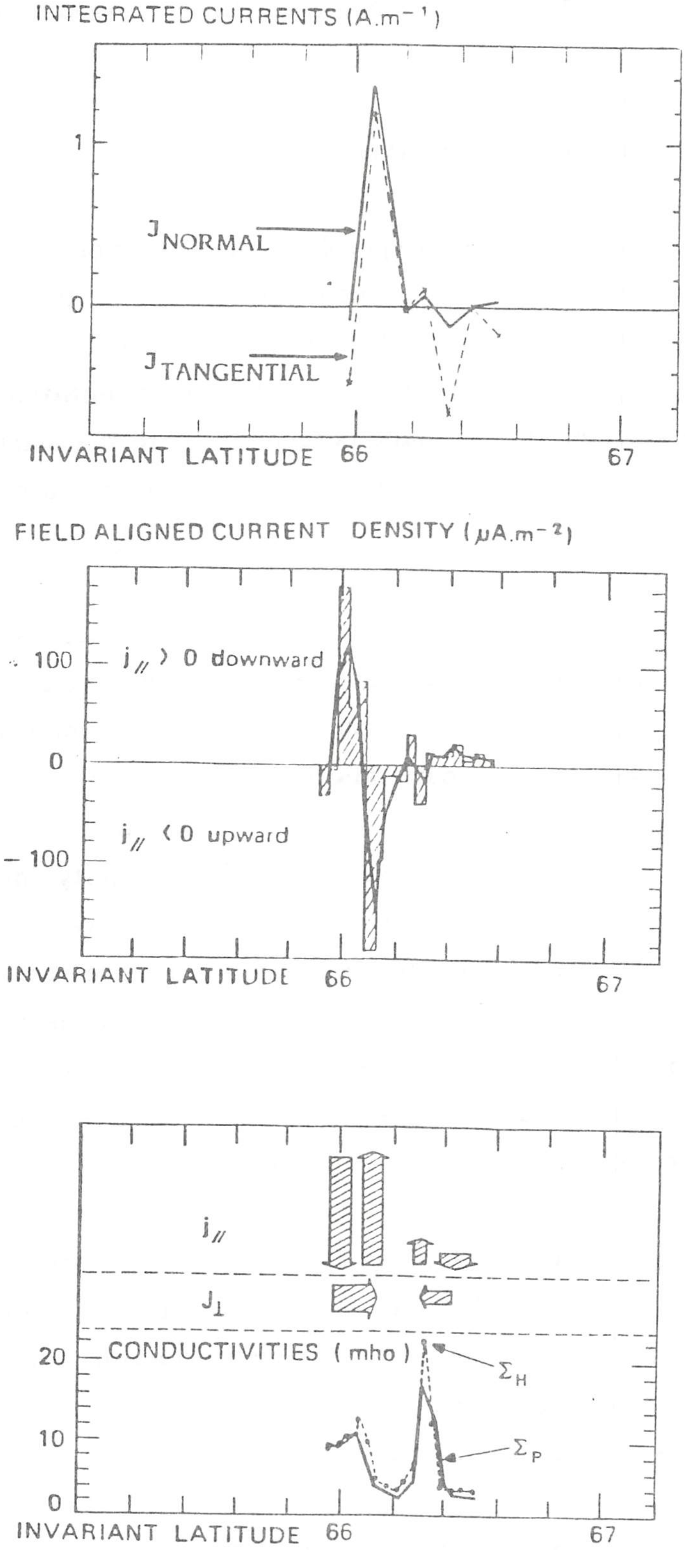

Figure 4. 11 March, 1984. Latitudinal profiles of ionospheric currents and schematic representation of the current circulation associated to the two-arc structure.

The top panels of Figure 4 display the latitudinal profiles of the field-aligned currents $j_{//}$ and of integrated currents $\vec{J}_\perp$ perpendicular to the magnetic field. The whole current system exhibits large intensities: in particular at the southward arc, both normal and tangent components of the perpendicular current exceed 1 A/m and the field aligned current density reaches almost 200 $\mu A/m^2$. One can also notice that the current circulation entirely reverses from one arc to the other one: the electrodynamic behaviour of such auroral structures, even close in time and space, can strongly differ. This feature is clearly illustrated in the bottom panel of Figure 4, which resumes in a schematic representation the main observations of the current system associated to this stable two-arc structure.

This study demonstrates the capability of ESICAT to determine the electrodynamic behaviour of small-scale structures such as these so-called stable auroral arcs. It contributes to build experimental basis to theoretical investigations of arc generation mechanisms.

6. CONCLUSIONS

Designed to explore the latitudinal structure of the auroral plasma, EISCAT scan experiments have supported number of investigations of the thermosphere, ionosphere and magnetosphere systems. Some examples taken from recent electrodynamic studies were chosen to illustrate the capabilities of this operating mode. It was in particular attempted to stress the procedure followed up to derive the relevant electrodynamic parameters from radar measurements, to discuss the results, and if possible, to test their accuracy to other observations or predictions.

In the proposed examples, the laws of fluid dynamics and electromagnetism, applied to EISCAT measurements during scan experiments, permitted to characterize:

- the planetary-scale distribution of plasma flow over the auroral zone. The pattern of the convection electrostatic potential was derived from EISCAT measurements in stationary conditions. It could be validated from simultaneous observations of the evening plasmaspheric bulge in the equatorial magnetosphere.

- the planetary-scale morphology of the auroral current system. In particular, the distribution of field-aligned currents derived from EISCAT data was found to be consistent with statistical spacecraft observations.

- the electrodynamic behaviour of the plasma in auroral structures of smaller scale. In the reported case of a stable arc structure, EISCAT measurements permitted to determine the arc orientation and to evaluate the current circulation associated to the arc.

REFERENCES

Alcaydé, D. 1981. An analytical model of temperature and composition from 20 to 2000 km altitude, Ann. Geophys., 37, 515.

Alcaydé, D., Caudal, G. and Fontanari, J. 1986. Convection electric fields and auroral electrostatic potential over $61° < \Lambda < 72°$ invariant latitude observed with the EISCAT facility, 1. Initial results, J. Geophys. Res., 91, 233.

Blanc, M. 1980. Convection du plasma dans l'ionosphère et la magnétosphère : un circuit électrique et sa résolution, Ann. Geophys., 36., 1.

Caudal, G. 1986. Field-aligned currents deduced from EISCAT radar observations and implications concerning the mechanism that produces Region-2 currents, submitted to J. Geophys. Res.

Evans, J.V., Holt, J.M., Oliver, W.L. and Wand, R.H. 1980. Millstone Hill inoherent scatter observations of auroral convection over $60° < \Lambda < 75°$, 2, Initial Results, J. Geophys. Res., 85, 41.

Folkestadt, K., Hagfors, T. and Westerlund, S. 1983. EISCAT : an updated description of technical characteristics and operational capabilities, Radio Sci., 18, 867.

Fontaine, D., Perraut, S., Alcaydé, D., Caudal, G. and Higel B. 1986. Large-scale structures of the convection inferred from coordinated measurements by EISCAT and GEOS 2, to be published in J. Atmos. Terr. Phys.

Foster, J.C., Doupnik, J.R. and Stiles, G.S. 1981. Large-scale patterns of auroral ionospheric convection observed with the Chatanika radar, J. Geophys. Res., 86, 11357.

Girard, L. and Senior, C. 1986. Electrodynamic structure of auroral arcs from EISCAT measurements : a case study, submitted to J. Geophys. Res.

Holt, J.M., Wand, R.H. and Evans, J.V. 1984. Millstone Hill measurements on 26 February, 1979 during the solar eclipse and formation of midday F-region through, J. Atmos. Terr. Phys., 46, 251.

Iijima, T. and Potemra, T.A. 1978. Large scale characteristics of field-aligned currents associated with substorms, J. Geophys. Res., 83, 599.

Kosik, J.C. 1978. The use of past and present magnetospheric field model for mapping fluxes and calculating conjugate points, Space Sci. Rev., 22, 48.

Olson, W.P. and Pfitzer, K.A. 1974. A quantitative model of the magnetospheric magnetic field, J. Geophys. Res., 79, 3729.

HIGH-LATITUDE PROBLEMS TO BE STUDIED BY INCOHERENT SCATTER RADARS

T.S. Jørgensen
Danish Meteorological Institute
2100 COPENHAGEN
Denmark

Abstract

A great variety of fascinating phenomena occur in the ionosphere of the highest latitude region of the earth. They are signatures of processes taking place in distant regions of the magnetosphere, and so investigation of these phenomena may help understanding the physics of the magnetosphere. In this paper we discuss a number of problems of the high-latitude upper atmosphere and suggest ways of exploring these by means of incoherent scatter radars.

1. INTRODUCTION

The purpose of this paper is to discuss some research topics of current interest concerning the high-latitude ionosphere and magnetosphere suitable for incoherent scatter radar (ISR) investigations. By high latitudes is meant the area covered and surrounded by the auroral oval. The region poleward of the oval is called the polar cap although other definitions of the polar cap boundary also sometimes are used, e.g. the limit of closed magnetic field lines, the boundary between sunward and antisunward plasma convection, and the poleward limit of the Region-1, field-aligned current system (Reiff, 1983).

The high-latitude ionosphere can now be observed directly by the EISCAT, Sondrestrom and Millstone Hill ISR's. Together they can "see" the ionosphere up to about 80°Λ (invariant latitude). The locations of EISCAT at ~66°Λ and Sondrestrom at ~74°Λ relative to the auroral region is shown in Figure 1. Millstone Hill is at ~55°Λ.

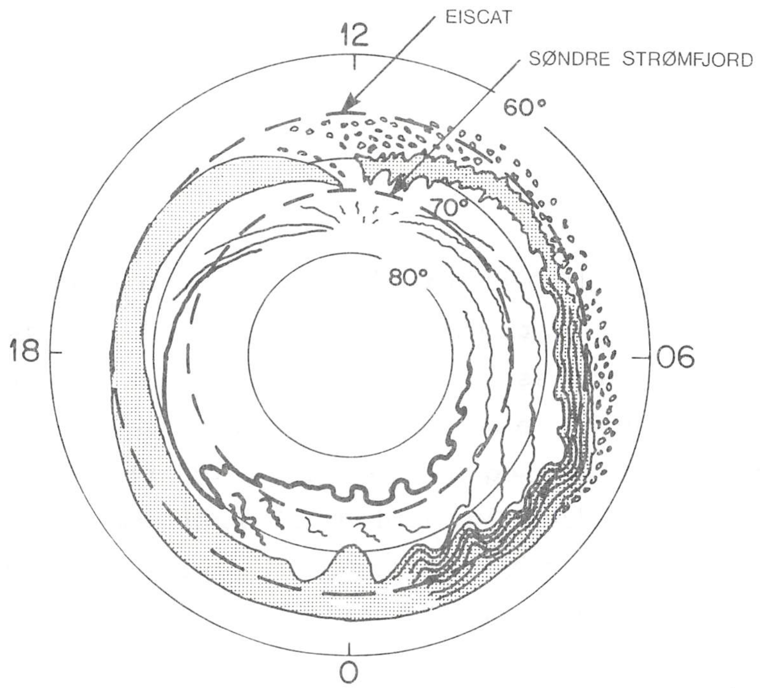

Figure 1. Locations of the EISCAT and Sondrestrom incoherent scatter radars relative to the auroral region. Coordinates are invariant latitude and magnetic local time (Adapted from Akasofu, 1976).

The other existing ISR's at Jicamarca and Arecibo cannot probe the high-latitude ionosphere directly, but they can observe effects of high-latitude events as for example gravity waves propagating equatorward from a region of energy dissipation at auroral latitudes.

The two most recently established ISR's are the EISCAT and Sondrestrom facilities. They began operations in 1981 and 1983 respectively. Their locations indicate a particular interest in the high-latitude region, the reason for which is illustrated in Figure 2. This figure shows the earth and the magnetosphere, and how the auroral oval and the polar cap is thought to be connected to various distant magnetospheric regions via the earth's magnetic field lines. Note that for clarity the earth is shown bigger than it is relative to magnetospheric dimensions.

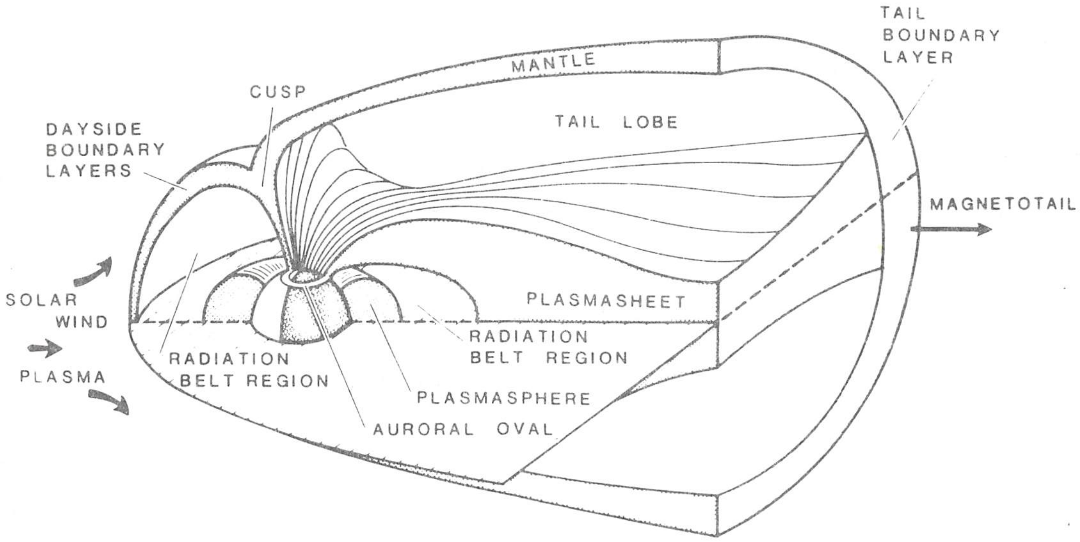

Figure 2. A sketch of fundamental plasma regions in the magnetosphere and their relations to the earth (Roederer, 1981).

Waves and charged particles in the magnetosphere tend to move along the earth's magnetic field. Therefore waves and particles originating in the outer magnetosphere may end up in the high-latitude ionosphere where their effects or "footprints" may be observed. So, an important argument for locating the EISCAT and Sondrestrom radars where they are is that these facilities can be used to investigate the distant magnetosphere. As seen in Figure 1, EISCAT passes under the nightside auroral oval and thus is well suited to investigate the plasma sheet region. Sondrestrom is close to the cusp region around noon, and this radar can observe signatures of solar wind - magnetosphere interactions.

One may ask why we need expensive ISR's to observe the high-latitude ionosphere, when many satellites capable of measuring many ionospheric parameters for years have been and still are crossing the polar regions. One answer is that ISR's can observe the E- and F-regions of the ionosphere simultaneously with a height resolution down to around a kilometer. No satellites can do this. Another reason has to do with the fast time variations of high-latitude ionospheric parameters. Satellites in low polar orbits spend less than a third of their time in the high-latitude regions, and this of course seriously diminish their probabilities of keeping track of temporal developments. An ISR on the other hand is able to record ionospheric variations for example during a substorm event with a time resolution of the order of a minute.

In the following sections we will discuss various high-latitude phenomena and problems with these, which may be studied with ISR's. Limit of space prevents the discussion to be exhaustive. The selected topics are not necessarily the most important ones, if such could be defined. They rather just reflect the author's interests.

2. ELECTRIC FIELDS

Electric fields have important effects on the ionosphere-thermosphere system at high latitudes. For example electric fields perpendicular to the earth's magnetic field will drive plasma convection which through collisions will create neutral winds in the thermosphere. In the E-region these electric fields move the electrons relative to the ions, which are braked by collisions with the neutrals and so create currents. Energy dissipation by Joule heating results from the Pedersen currents. A quantitative understanding of these effects requires a knowledge of the instantaneous high-latitude convection pattern.

Convection electric fields have been measured by a variety of techniques including satellite-, rocket-, and balloon-borne probes, optical tracking of ionized barium clouds, coherent scatter observations of drifting E-region irregularities and ISR observations of drifting F-region plasma. Since all these measurement techniques provide information on only a limited spatial region at any time, the construction of the overall convection pattern requires a synthesis of data obtained at a variety of places and times. Such synthesis leads to average rather than instantaneous convection patterns.

The extent to which average convection models (e.g. Heppner, 1977 and Heelis et al., 1982) can describe the instantaneous convection pattern is not clear. Also, is is not clear to what extent magnetospheric signatures have been distorted during the averaging process.

The only way instantaneous convection patterns in the entire high-latitude region can be obtained is to combine simultaneous electric field observations from several well distributed locations. In such an effort the high-latitude ISR's play an important role.

In 1981-82 a campaign of coordinated observations was carried out using the Chatanika (65°Λ), Millstone Hill and EISCAT radars. 110 hours of simultaneous observations by all three radars were made from September 1981 to January 1982. This was the start of the MITHRAS (Magnetosphere Ionosphere Thermosphere Radar Studies) program (de la Beaujardière et al., 1984). Also other methods of electric field measurements were included. The groups operating the Dynamics Explorer satellites (Hoffman, 1981) and the STARE (Scandinavian Twin Auroral Radar Experiment) coherent radar (Greenwald et al., 1978) made special efforts to acquire data coincident with the incoherent scatter radar observations.

With the purpose of determining instantaneous high-latitude convection patterns Heelis et al. (1983) combined ionospheric drift velocity measurements taken during a MITHRAS campaign from the Dynamics Explorer 2 satellite and the Chatanika and Millstone Hill radars. They found that during a magnetic disturbance, the entire convection pattern expanded equatorward.

All ISR's make simultaneous observations every month on so-called Incoherent Scatter Coordinated Days, which are appointed in the International Geophysical Calender. The observations are stored in the Incoherent Scatter Radar Data Base at NCAR, Boulder, Colorado, where they are available to the scientific community.

3. FIELD-ALIGNED CURRENTS

Electric currents flow along the earth's magnetic field at auroral latitudes. They are generated in the distant magnetosphere and dissipate energy in the upper atmosphere, which can exceed the energy dissipated there by auroral particles.

The field-aligned currents are concentrated in two regions which encircle the geomagnetic pole. These are shown in Figure 3. The current regions have been arbitrarily designated by Iijima and Potemra (1976a) as "Region 1" located at the poleward side, and "Region 2" located at the equatorward side. The Region 1 currents flow into the ionosphere in the morning sector and away from the ionosphere in the evening sector. The Region 2 currents flow in the opposite direction at any given local time. As shown in Figure 3 field-aligned currents also occur in a longitudinally limited region around noon poleward of the Region 1 current. These are called cusp currents.

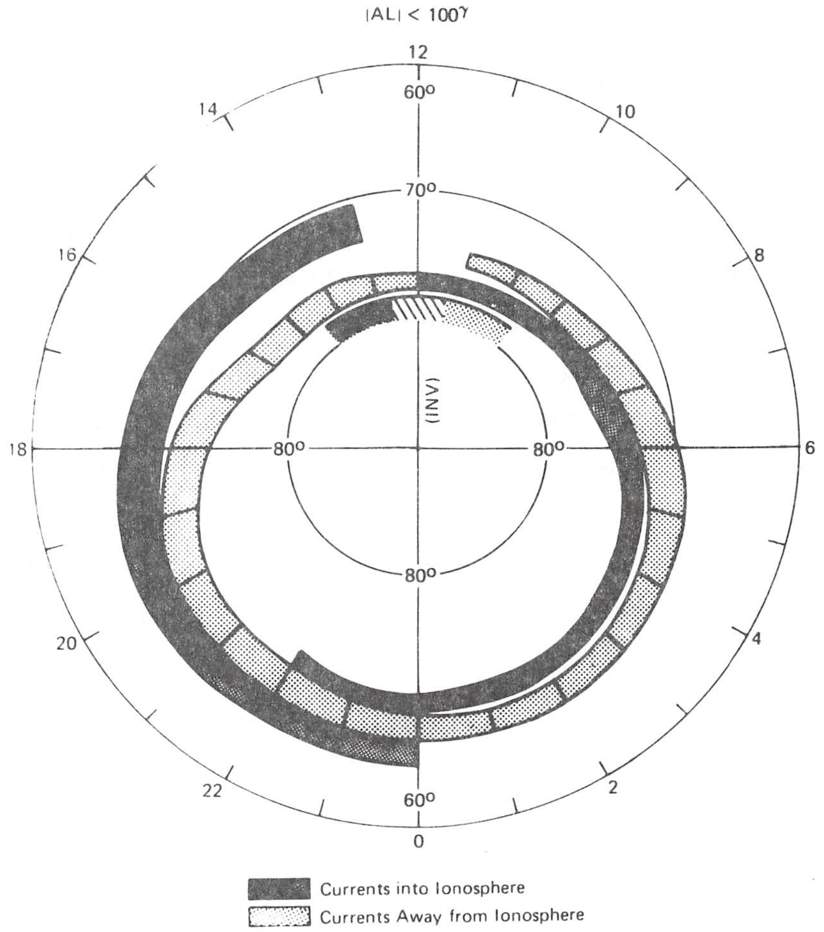

Figure 3. A summary of the distribution and flow directions of large-scale field-aligned currents determined from data obtained on the TRIAD satellite during weakly disturbed conditions (Iijima and Potemra, 1976b).

One important problem concerning field-aligned currents is where and how they are generated in the distant magnetosphere. In the following we will discuss some proposed models of field-aligned current generation, and how ISR measurements may help to distinguish between them. To ease the comparison we choose to discuss currents in the dawn sector of the magnetosphere only.

Sonnerup (1980) developed a steady state fluid model of the low-latitude boundary inside the magnetopause. The plasma flow there is antisunward, and earthward of this a sunward return flow occurs. Both flows are perpendicular to the earth's magnetic field, and so electric fields are generated ($E = VxB$). In the boundary layer the electric field is away from the earth, and in the return flow generator the field is towards the earth. These electric fields drive field-aligned currents towards the earth from the region surrounding the interface between the boundary layer and return flow generators and away from the earth in the earthward region of the return flow generator. Assuming that the generator electric fields are mapped along magnetic field lines to the ionosphere, the spatial relationship of field-aligned currents and electric fields there is as shown in Figure 4a. It is seen that the model predicts Region 1 currents to occur poleward as well as equatorward of the convection reversal boundary.

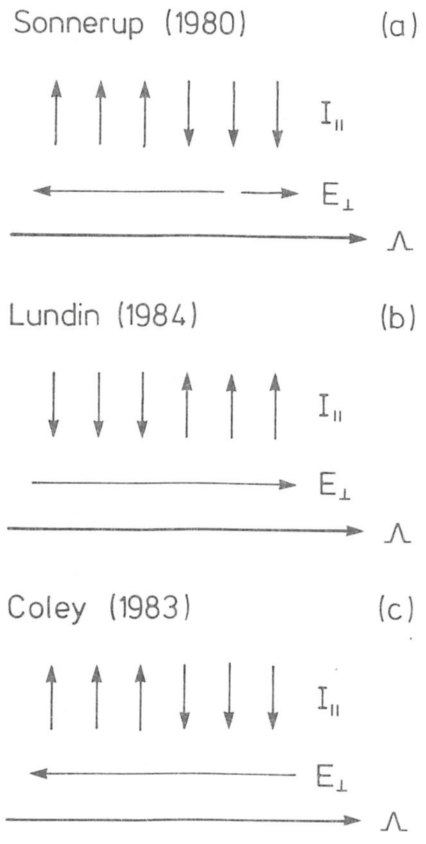

Figure 4. Spatial relations between field-aligned currents and electric fields in the dawn sector of the high-latitude ionosphere according to three different models (see text).

Lundin (1984) discussed generation of field-aligned currents by a similar magnetohydromagnetic process confined to the low-latitude boundary layer only. The resulting field-aligned currents in the high-latitude ionosphere are shown in Figure 4b. The current out of the ionosphere is poleward of the current into the ionosphere, and both occur in a region with a poleward or dawn-dusk directed electric field. These currents cannot correspond to the Region 1 and 2 currents, which are in the opposite directions in the dawn sector, but they could possibly represent the Region 1 current and the cusp current before noon (see Figure 3).

It should be noted that the current system discussed by Lundin (1984) is based on the assumption of a local process, which may not generate the entire Region 1 and 2 field-aligned currents.

The spatial relationship between field-aligned currents and perpendicular electric fields in the ionosphere has also been derived from measurements. One such empirical model results from observations of field-aligned currents, 1-keV electron precipitation and the direction of the horizontal electric field by the AE-C Spacecraft (Coley, 1983). It was found that Region 1 and 2 currents both occur equatorward of the convection electric field reversal as shown in Figure 4c. This indicates that field-aligned currents are generated in the region of the magnetosphere, where the plasma convection is sunward and not in the antisunward flowing low latitude boundary layer.

The different spatial relationships between field-aligned currents and convection electric fields discussed above and illustrated in Figure 4 indicate a need to further study these currents and fields with the aim of finding signatures in the high-latitude ionosphere of the field-aligned current source regions.

The Sondrestrom and EISCAT radars are well suited for this purpose. From measurements of ion velocity and E-region electron density, electric fields, conductivities and horizontal ionospheric currents can be found. Calculation of the divergence of the horizontal currents then leads to field-aligned currents. The applicability of this method was demonstrated by Robinson et al. (1982).

4. AURORA

The diffuse and discrete aurora generally occur in a ring-shaped area roughly between 65° and 75°Λ. This is the so-called auroral oval (Figure 1). In about the same latitude range, plasma convection predominantly is westward in the evening side between noon and midnight and eastward in the morning side from midnight to noon (Heppner, 1977). At latitudes higher than ~75°Λ, where the plasma convection usually has an antisunward component, auroral emissions are less common. These observations suggest that aurora is related to the plasma convection pattern, and then to electric fields.

Electric field measurements around auroral arcs are of interest for at least two reasons. First, the direction of plasma convection near the arcs may indicate the location in the magnetosphere of the plasma source region providing the auroral particles. If convection on both sides of an arc is sunward, the source region is likely to be in the plasma sheet or its boundary layer. If convection on both sides is antisunward, the source region may be the low latitude boundary layer, and of course, if the arcs occur at the convection reversal boundary, a source at the inner edge of the low latitude boundary layer is indicated. Second, the distribution of electric fields around the aurora in the ionosphere may give information on the potential structure in the magnetosphere, where auroral particles are accelerated.

Vondrak (1981) summarized what has been learned from Chatanika radar measurements of electric fields around auroral arcs. All observed arcs were in the region of sunward convection or near the convection reversal boundary. No observations of auroral arcs clearly poleward of the convection reversal boundary were reported, but of course, this may be because the Chatanika radar was located at 65°Λ and so rarely had a chance to investigate the region of antisunward convection.

Heelis et al. (1980) and Heelis et al. (1981) reported on electric field and particle measurements by the AE-C satellite. They found not only auroral precipitation in the region of sunward convection, but also slightly poleward of the convection reversal boundary in the antisunward convection region, and they concluded that the precipitation poleward of the reversal boundary originated on closed field lines threading the antisunward flowing low latitude boundary layer.

Recently Frank et al. (1986) investigated the generally sun-aligned transpolar Theta aurora, which extends from the dayside to the nightside sectors of the auroral oval, using observations from both of the Dynamics Explorer satellites. They found that this aurora occurred in or near a shear between sunward and antisunward convection, and that the overall character of the transpolar arc region appears to be very similar to that observed over the poleward zones of the auroral oval, which is currently thought to be magnetically mapped into the boundary layer of the plasma sheet in the magnetotail.

Finally, we will mention a study of auroral morphology in the noon sector based on images from DMSP satellites by Meng and Lundin (1986) in which they concluded that the discrete auroras in the midday oval may be caused by injection of magnetosheath plasma into the dayside boundary layer.

These studies indicate that the particles producing the aurora may come from various different magnetospheric regions, i.e. the plasma sheet and its boundary layer, the low latitude boundary layer, and the interface between the plasma sheet and the low latitude boundary layer.

However, much work remains to be done before the relationship between the aurora and the distant magnetosphere is well understood. Both the EISCAT and the Sondrestrom radars are very useful for this kind of investigations. In particular the Sondrestrom radar which regularly will be near all the types of auroral phenomena mentioned above. Not only the electric field observations are important, but other ionospheric parameters like plasma density and temperature which can be measured by these radars, may help to characterize the environment of the auroras and provide clues regarding their sources.

There is a fascinating perspective in the study of and eventual profound knowledge of the relation between auroral arcs and convection electric fields, which is that we may be able to obtain information on the instantaneous convection pattern all over the polar region from an image of the auroral emissions over that area. Such images are presently being provided by the DMSP, DE-1, and VIKING satellites.

5. SUBSTORMS

Substorms are manifestations of energy transfer from the solar wind to the magnetosphere and the ionosphere. It has been suggested that substorms result from a sudden conversion of magnetic energy accumulated in the magnetosphere prior to substorm onset, and that the onset is triggered, when the amount of stored magnetic energy reaches a critical level (cf. Russell and McPherron, 1973 and McPherron et al., 1973). On the other hand, Perreault and Akasofu (1978) and Akasofu (1981) have suggested that substorms occur when the power ε of the solar wind - magnetosphere dynamo reaches a critical level. These two models are known as the unloading and directly driven substorm models respectively, and the relative importance of the two processes is still a matter of debate (Akasofu, 1986).

The reason that it is so difficult to distinguish between the two processes is that widely separated plasma regions in the solar wind, the magnetosphere and the ionosphere are involved in the substorm process, and therefore that many parameters in these regions must be observed simultaneously with a time resolution of about a few minutes in order to obtain a complete description of a substorm. This is of course not easy, because the necessary satellites and ground stations not always are in the proper locations.

The simultaneous operations of the high-latitude ISR's, such as in the MITHRAS campaigns mentioned above, provide a very important set of data for substorm studies. The advantage of the radar data is that the radars provide continuous coverage at several locations, and that they can provide the parameters that are needed to define both the electrodynamic and precipitation aspect of the energy transfer. For example, the radars can determine the electric fields and the ionospheric and field-aligned currents, as well as the energy dissipation parameters such as Joule heating and particle precipitation.

The response of the high-latitude electric field to substorms was studied by de la Beaujardière et al. (1983). Simultaneous observations during five substorm periods from the Chatanika and Millstone Hill incoherent scatter radars and the STARE coherent radar were analysed, and it was found that the electric field signature associated with substorms depends on the local time at which it is observed. The electric field appears to reverse near noon and midnight and intensifies near dawn and dusk. In one case, an abrupt intensification of the electric field was simultaneously observed in the dusk and dawn sectors.

Since January 1984 several coordinated campaigns with the purpose of investigating substorms have been carried out in a program called GISMOS (Global Incoherent Scatter Measurements of Substorms). All existing ISR's participate in the program, but many other types of ground-based and satellite-borne observations are included in the data analysis. An important part of the GISMOS program is development of models for auroral latitude ionospheric conductivities due to particle precipitation and solar radiation, the high-latitude convection pattern and thermospheric neutral winds. For further information regarding GISMOS contact O. de la Beaujardière, SRI International, Menlo Park, California.

6. MAGNETOSPHERIC REGIONS

Satellite observations have revealed that the plasma in the magnetosphere is far from uniform. On the contrary, several regions each with its characteristic plasma parameters have been observed within the magnetosphere. Inside the magnetopause at high latitudes is the entry layer, the cusp and the plasma mantle. At low latitudes along the flanks of the magnetosphere is the low latitude boundary layer, and in the magnetotail is the plasma sheet, the plasma sheet boundary layer and the tail lobes (see Figure 2 and for example Frank, 1985). The range of plasma density in these regions is from less than 0.1 cm^{-3} in the tail lobes to ~50 cm^{-3} in the low latitude boundary layer. Electron temperatures vary from ~10^5°K in the low latitude boundary layer to 2 x 10^7°K in the plasma sheet boundary layer. All these regions are connected via the earth's magnetic field lines to the high-latitude ionosphere, where they may be expected to expose recognizable signatures or footprints as mentioned in the introduction. A very important task is to discover the characteristics of these footprints. The high-latitude ISR's should be efficient tools for this, since they can measure so many different ionospheric parameters simultaneously and continuously.

It is generally accepted that some of the earth's magnetic field lines are "closed" and some are "open". The closed field lines each connect two conjugate points in opposite hemispheres. The open field lines extend from the earth's polar regions and connect to the solar or interplanetary magnetic field (IMF). It is of basic importance for magnetospheric physics to know where the boundary between the closed and open field lines is located, but despite of much work this problem has not been satisfactorily solved.

Heelis et al. (1980) made simultaneous measurements of the auroral zone particle precipitation and the ion convection velocity by the Atmosphere Explorer C and D satellites. They found a consistent difference between the location of the poleward boundary of the auroral particle precipitation and the ion convection reversal. The difference of about 1.5°Λ is such that some part of the antisunward convection lies wholly within the auroral particle precipitation region. This indicates that some of the dawn to dusk electric field is generated on closed field lines perhaps connected to the low latitude boundary layer.

The result is inconsistent with earlier work by Frank and Gurnett (1971) and Gurnett and Frank (1973) who found from Injun 5 observations of energetic particles and electric fields that the electric field reversal marked the boundary between open and closed field lines. And Coley (1983) found from particle and electric field measurements on Atmosphere Explorer C that in the evening and morning sectors of the winter high-latitude region the poleward edge of precipitation of electrons with energy above 1keV in general is collocated with the convection reversal boundary, which also suggests that the reversal boundary marks the boundary between open and closed field lines.

It is conceivable that measurements in the magnetic meridian plane across the convection reversal boundary by the Sondrestrom and EISCAT radars may provide information regarding the boundary between open and closed field lines.

One reason for the above mentioned inconsistent results regarding the location of the open/closed field line boundary may be that the relationship between this boundary and the convection reversal boundary is a function of local time. Assuming that the magnetic field lines are frozen into the plasma of the magnetosphere, a magnetic field line in the noon meridian, extending from the ionospheric cusp region to the equatorial low latitude boundary layer, will move such that its equatorial location will be in the low latitude boundary layer at the dawn and dusk meridian before its ionospheric extremity moves more than about a half hour in local time (assuming typical flow speeds of 200 km/s in the equatorial plane inside the magnetopause and 0.5 km/s in the ionosphere). Thus, any ionospheric signature of the low latitude boundary layer must be confined to the region near noon.

Another reason that signatures of the low latitude boundary layer in the high-latitude ionosphere are hard to find may be that it is generally difficult to find a low latitude boundary layer on a single magnetopause crossing of a satellite, indicating that a low latitude boundary layer may not exist at all times everywhere inside the magnetopause. Thus for example Mozer (1986) has reported that only 28 magnetopause crossings having identifiable low latitude boundary layers were found in a search through about 50 magnetopause crossings of the ISEE-1 satellite.

As an example of a type of ISR data which may be useful in a search of ionospheric signatures of magnetospheric regions, we show in Figure 5 the latitudinal relationship between F-region electron temperature, the convection reversal boundary and the ionospheric DPY-current (derived from magnetometers) in the noon sector (Vennerstrøm et al., 1984). In this study it was concluded that the DPY-current is physically associated with the primary (antisunward) convection, contrary to the electrojet currents which are assosiated with (sunward) return flow. Furthermore, the DPY-current is flowing in the region of open field lines, while the auroral electrojets are flowing on closed field lines.

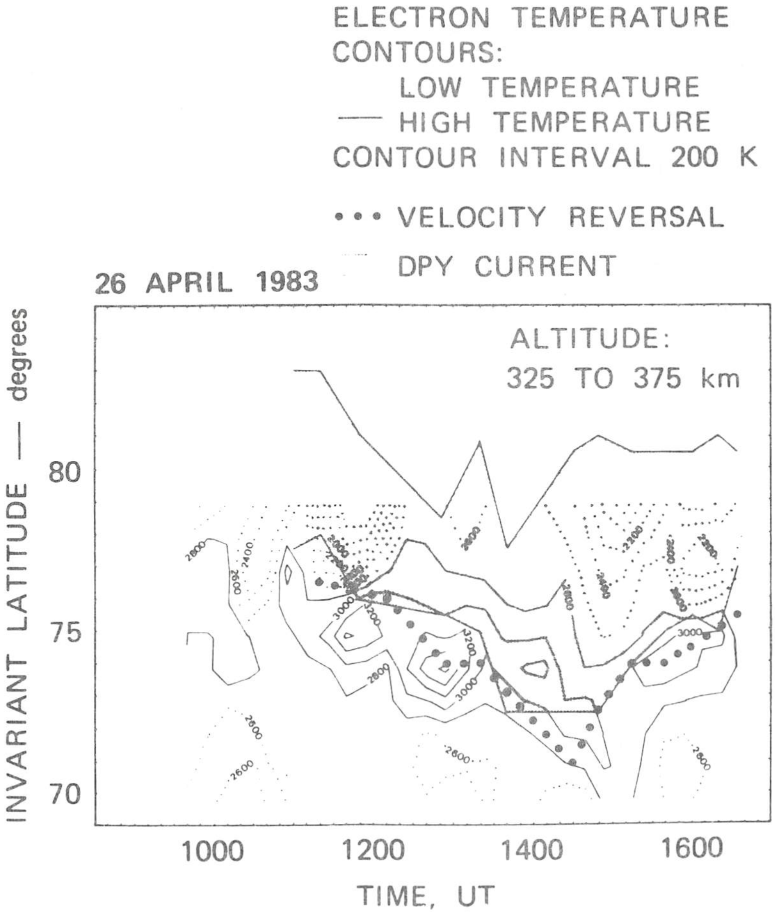

Figure 5. Latitudinal relationship between ionospheric regions characterized by electron temperature and convection velocity measured by the Sondrestrom radar and by the ionospheric DPY-current derived from magnetometers (Vennerstrom et al., 1984).

7. SOLAR WIND - MAGNETOSPHERE INTERACTIONS

The solar wind is responsible for a number of phenomena in the magnetosphere. Both intermittently occurring events like substorms and continuous albeit highly variable processes as the magnetospheric plasma convection derive their energy from the solar wind.

Two different mechanisms for transfer of solar wind energy into the magnetosphere were both proposed a quarter of a century ago, and they are still being actively debated. In one, closed magnetospheric flux tubes are transported from the dayside to the nightside of the magnetosphere in the boundary layer around the flanks of the magnetosphere by a "viscouslike" process occurring at the magnetopause (Axford and Hines, 1961), and in the other, open flux tubes are transported over the poles of the earth, after merging between the earth's and the interplanetary magnetic field has taken place (Dungey, 1961). A third possible mechanism may be that magnetosheath plasma is impulsively injected into the closed magnetosphere (Lemaire, 1977).

Since the mid-1960's much evidence of magnetic merging and open flux transport has been accumulated, but observations in the low latitude boundary layer and in the ionosphere have indicated that the viscous interaction process is of importance too (e.g. Cowley, 1982, and references therein). So the two processes may coexist, and the question then arises, what their relative contributions are.

ISR's have been used to investigate solar wind-magnetosphere interaction. For example the relation between the IMF and the high-latitude convection was studied by Clauer et al. (1984), Jørgensen (1985), de la Beaujardière et al. (1985), and Risbeth et al. (1985). These studies have indicated that the plasma convection all over the high-latitude region after about 10-15 minutes responds to changes in the IMF. An example of this relationship is illustrated in Figure 6, which shows that changes around 11-12 UT (09-10 MLT) in ionospheric plasma convection velocity in a several degrees wide latitude range correspond to variations in the IMF. The exact nature of this coupling between the IMF and the high-latitude ionosphere is not known, and we stress the importance of making simultaneous IMF and ionospheric observations with good spatial and temporal resolution.

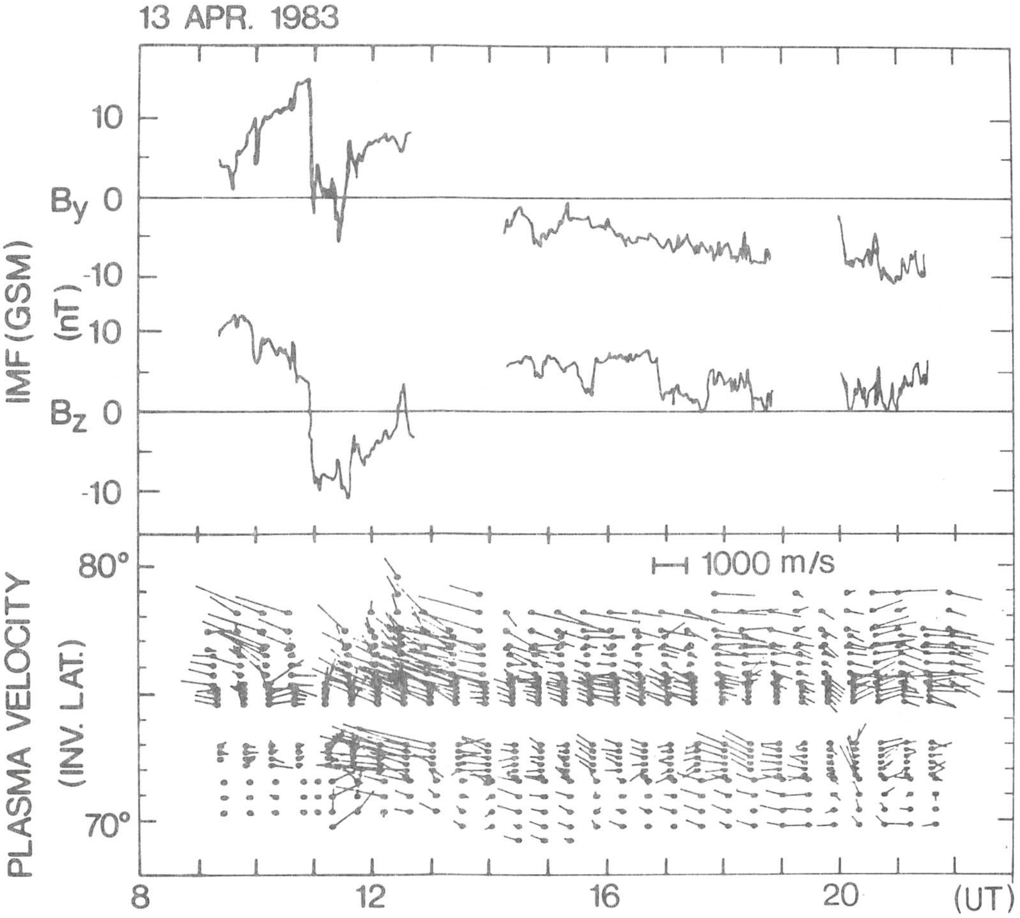

Figure 6. Interplanetary magnetic field B_y and B_z components observed by IMP-8 and high-latitude ionospheric plasma convection observed with the Sondrestrom radar (Jørgensen, 1985).

Goertz et al. (1985) discussed the different signatures in high-latitude plasma convection to be expected to result from the three solar wind - magnetosphere interaction mechanisms mentioned above, and van Eyken et al. (1984) demonstrated the potential of the EISCAT radar system to explore this possibility of distinguishing between the mechanisms. Figure 7 shows that the predominantly westward (sunward) flow in the afternoon sector suddenly rotates to become largely poleward in a ~10 min. period, and van Eyken et al. (1984) conclude that a possible explanation of this sudden change of direction is that an observation has been made of the ionospheric signature of an event in which a region of initially closed, sunward moving, flux tubes are suddenly coupled into the magnetosheath flow, indicating that merging of the IMF and the earth's magnetic field occurs.

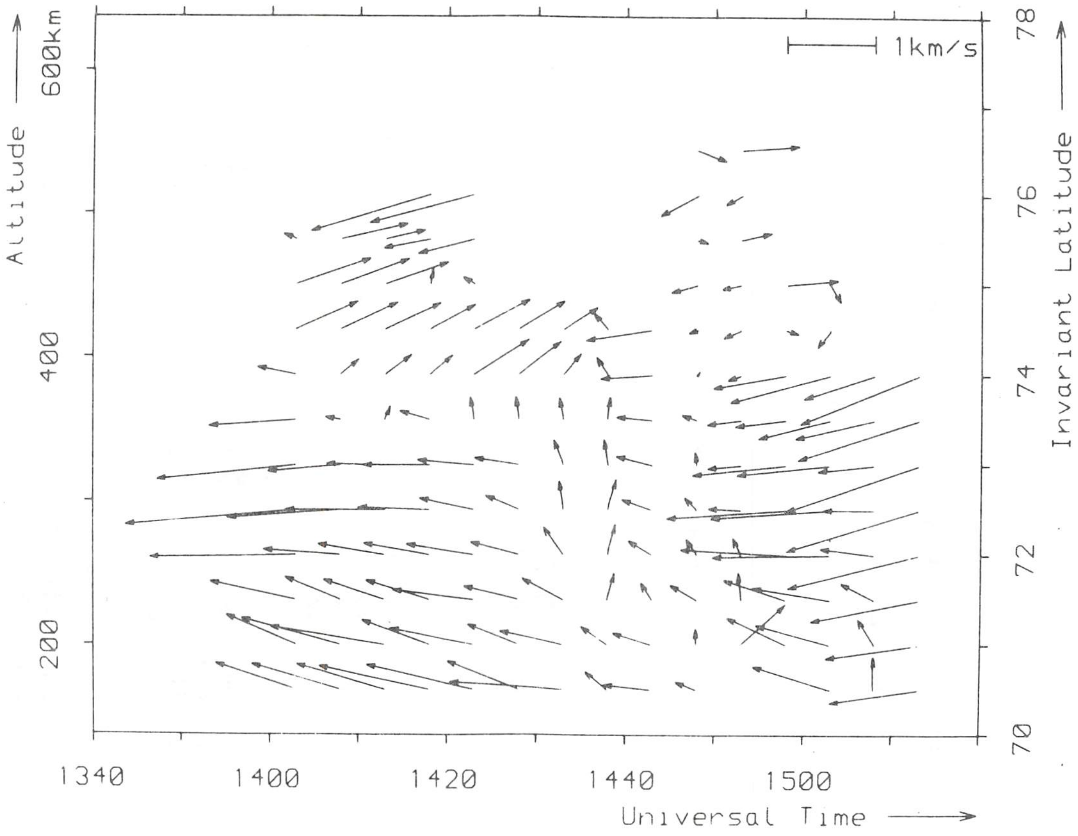

Figure 7. Plasma convection velocities measured by the EISCAT radar (van Eyken et al., 1984).

The size and shape of the magnetopause region(s) where the solar wind - magnetosphere interaction occurs is not known. Information about this may be derived from the size and shape of the corresponding signatures in the ionosphere, which may be obtained from simultaneous measurements by the high-latitude ISR's.

Reiff and Burch (1985) constructed a qualitative model of the high-latitude ionospheric plasma convection pattern incorporating the effects of both merging of the interplanetary magnetic field with the earth's magnetic field and of viscous processes. One interesting prediction of this model, which should be possible to check with high-latitude ISR measurements, is that for IMF-$B_y > 0$ there are two convection reversal boundaries in the dusk sector and one in the morning sector in the northern polar region, while the opposite should be the case for IMF-$B_y < 0$.

8. CONCLUSIVE REMARKS

This paper is not intended to be a comprehensive review of upper atmospheric phenomena which take place in the highest latitude region of the earth, but rather be a provocative document by discussing how ISR's may contribute to further understanding and eventual solution of problems in connection with some of these phenomena. The survey is far from complete. For example important subjects as the neutral atmosphere and ionospheric ion composition, which are well suited for ISR studies are left out.

REFERENCES

Akasofu, S.-I. 1976. Recent progress in studies of DMSP auroral photographs, Space Sci. Rev., 19, 169.

Akasofu, S.-I. 1981. Energy coupling between the solar wind and the magnetosphere, Space Sci. Rev., 28, 121.

Akasofu, S.-I. 1986. Som critical issues on magnetospheric substorms, Planet. Space Sci., 34, 563.

Axford, W.I. and C.O. Hines. 1961. A unifying theory of high-latitude geophysical phenomena and geomagnetic storms, Can. J. Phys., 39, 1433.

Clauer, C.R., P.M. Banks, A.Q. Smith, T.S. Jørgensen, E. Friis-Christensen, S. Vennerstrøm, V.B. Wickwar, J.D, Kelly, and J. Doepnik. 1984. Observation of interplanetary magnetic field and of ionospheric plasma convection in the vicinity of the dayside polar cleft, Geophys. Res. Lett., 11, 891.

Coley, W.R. 1983. Spatial relationship of field-aligned currents, electron precipitation, and plasma convection in the auroral oval, J. Geophys. Res., 88, 7131.

Cowley, S.W.H. 1982. The causes of convection in the earth's magnetosphere: A review of developments during the IMS, Rev. Geophys. Space Phys., 20, 531.

de la Beaujardière, O., J. Holt, and E. Nielsen. 1983. Early MITHRAS results: The electric field response to substorms, Radio Sci., 18, 981.

de la Beaujardière, O., V.B. Wickwar, M.J. Baron, J. Holt, R.M. Wand, W.L. Oliver, P. Bauer, M. Blanc, C. Senior, D. Alcaydé, G. Caudal, J. Foster, E. Nielsen, and R. Heelis. 1984. MITHRAS: A brief description, Radio Sci, 19, 665.

de la Beaujardière, O., V.B. Wickwar, J.D. Kelly, and J.H. King. 1985. Effect of the interplanetary magnetic field Y-component on the high-latitude nightside convection, Geophys. Res. Lett., 12, 461.

Dungey, J.W. 1961. Interplanetary field and the auroral zones, Phys. Rev. Lett, 6, 47.

Frank, L.A. and D.A. Gurnett. 1971. Distributions of plasmas and electric fields over the auroral zones and polar caps, J. Geophys. Res., 76, 6829.

Frank, L.A. 1985. Plasmas in the earth's magnetotail, Space Sci. Rev., 42, 211.

Frank, L.A., J.D. Craven, D.A. Gurnett, S.D. Shawhan, D.R. Weimer, J.L. Burch, J.D. Winningham, C.R. Chappell, J.H. Waite, R.A. Heelis, N.C. Maynard, M. Sugiura, W.K. Peterson, and E.G. Shelley. 1986. The Theta aurora, J. Geophys. Res., 91, 3177.

Goertz, C.K., E. Nielsen, A. Korth, K.H. Glassmeier, C. Haldoupis, P. Høeg, and D. Hayward. 1985. Observations of a possible ground signature of flux transfer events, J. Geophys. Res., 90, 4069.

Greenwald, R.A., W. Weiss, E. Nielsen, and N.R. Thomson. 1978. STARE: A new radar auroral backscatter experiment in northern Scandinavia, Radio Sci., 13, 1021.

Gurnett, D.A. and L. Frank. 1973. Observed relationships between electric fields and auroral particle precipitation, J. Geophys. Res., 78, 145.

Heelis, R.A., J.D. Winningham, W.B. Hanson, and J.L. Burch. 1980. The relationship between high latitude convection reversals and the energetic particle morphology observed by Atmosphere Explorer-C, J. Geophys. Res., 85, 3315.

Heelis, R.A., W.B. Hanson, and J.L. Burch. 1981. AE-C observations of electric fields around auroral arcs, in Physics of Auroral Arc Formation, ed. by S.-I. Akasofu and J.R. Kan, American Geophysical Union, Washington, D.C.

Heelis, R.A., J.K. Lowell, and R.W. Spiro. 1982. A model of the high-latitude ionospheric convection pattern, J. Geophys. Res., 87, 6339.

Heelis, R.A., J.C. Foster, O. de la Beaujardière, and J. Holt. 1983. Multistation measurements of high-latitude ionospheric convection, J. Geophys. Res., 88, 10, 111.

Heppner, J.P. 1977. Empirical models of high-latitude Electric fields, J. Geophys. Res., 82, 1115.

Hoffman, R.A.. 1981. Dynamics Explorer, Space Sci. Instrum., 5.

Iijima, T. and Potemra, T.A. 1976a. The amplitude distribution of field-aligned currents at northern high latitudes observed by Triad, J. Geophys. Res., 81, 2165.

Iijima, T. and Potemra, T.A. 1976b. Field-aligned currents in the dayside cusp observed by Triad, J. Geophys. Res., 81, 5971.

Jørgensen, T.S., 1985. Polar cap/polar cusp studies using incoherent scatter radar facilities, in Results of THE ARCAD 3 PROJECT and of recent programmes in magnetospheric and ionospheric physics, Cepadues-Editions, France.

Lemaire, J. 1977. Impulsive penetration of filamentary plasma elements into the magnetosphere of the Earth and Jupiter, Planet. Space Sci., 25, 887.

Lundin, R. 1984. Solar wind energy transfer regions inside the dayside magnetopause - II. Evidence for an MHD generator process, Planet. Space Sci., 32, 757.

McPherron, R.L., C.T. Russell, and M.P. Aubry. 1973. Satellite studies of magnetospheric substorms on August 16, 1968, 9. Phenomenological model for substorms, J. Geophys. Res., 78, 3131.

Meng, C.-I. and R. Lundin. 1986. Auroral morphology of the midday oval, J. Geophys. Res., 91, 1572.

Mozer, F.S. 1986. Reply, Geophys. Res. Lett., 13, 235.

Perreault, P. and S.-I. Akasofu, 1978. A study of geomagnetic storms, Geophys. J. R. Astr. Soc., 500, 547.

Reiff, P.H. 1983. Polar and auroral phenomena: A review of U.S. progress during 1979-1982, Rev. Geophys. Space Phys., 21, 418.

Reiff, P.H. and J.L. Burch. 1985. IMF B_y-dependent plasma flow and Birkeland currents in the dayside magnetosphere 2. A global model for northward and southward IMF, J. Geophys. Res., 90, 1595.

Risbeth, H., P.R. Smith, S.W. H. Cowley, D.M. Willis, A.P. van Eyken, B.J.I. Bromage, and S.R. Crothers. 1985. Ionospheric response to changes in the interplanetary magnetic field observed by EISCAT and AMPTE-UKS, Nature, 318, 451.

Robinson, R.M., R.R. Vondrak, and T.A. Potemra. 1982. Electrodynamic properties of the evening sector ionosphere within the Region 2 field-aligned currentsheet, J. Geophys. Res., 87, 731.

Roederer, J.G. 1981. The solar wind-magnetosphere- ionosphere system: An overview, in Exploration of the Polar Upper Atmosphere, ed. by C.S. Deehr and J.A. Holtet, D. Reidel Publishing Company.

Russell, C.T. and R.L. McPherron. 1973. The magnetotail and substorms, Space Sci. Rev., 15, 205.

Sonnerup, B.U.Ö. 1980. Theory of the low-latitude boundary layer, J. Geophys. Res., 85, 2017.

van Eyken, A.P., H. Risbeth, D.M. Willis, and S.W.H. Cowley. 1984. Initial EISCAT observations of plasma convection at invariant latitudes 70°-77°, J. atmos. terr. Phys., 46, 635.

Vennerstrøm, S., E. Friis-Christensen, T.S. Jørgensen, O. Rasmussen, C.R. Clauer, and V.B. Wickwar. 1984. Ionospheric currents and F-region plasma boundaries near the dayside cusp, Geophys. Res. Lett, 11, 903.

Vondrak, R.R. 1981. Chatanika radar measurements of the electrical properties of auroral arcs, in Physics of Auroral Arc Formation, ed. by S.-I. Akasofu and J.R. Kan, American Geophysical Union, Washington, D.C.

THE SONDRESTROM INCOHERENT-SCATTER RADAR FACILITY

J. Kelly
SRI International
Geoscience and Engineering Center
Menlo Park, California 94025 USA

1. SCIENTIFIC OBJECTIVES

Incoherent-scatter radar measurements of the electrodynamic properties of the very high-latitude ionosphere will provide necessary contributions to the understanding of magnetospheric boundary variations and magnetospheric/ionospheric coupling. As shown in Figure 1, three distinct regions can be surveyed with the Sondrestrom facility: (1) the dayside auroral oval, (2) the polar cap, and (3) the poleward side of the nighttime auroral oval. In addition, this radar is situated so that it is the northernmost element of a chain of incoherent-scatter facilities extending from high latitudes to the equator.

1.1 Dayside auroral oval

The questions that can be studied with incoherent-scatter radar observations of the dayside auroral oval are:

- What is the plasma convection pattern?
- How does the convection pattern vary with the orientation of the IMF?
- How does the sunward to antisunward reversal in plasma flow vary temporally and spatially?
- What are the characteristics of the dayside aurora?

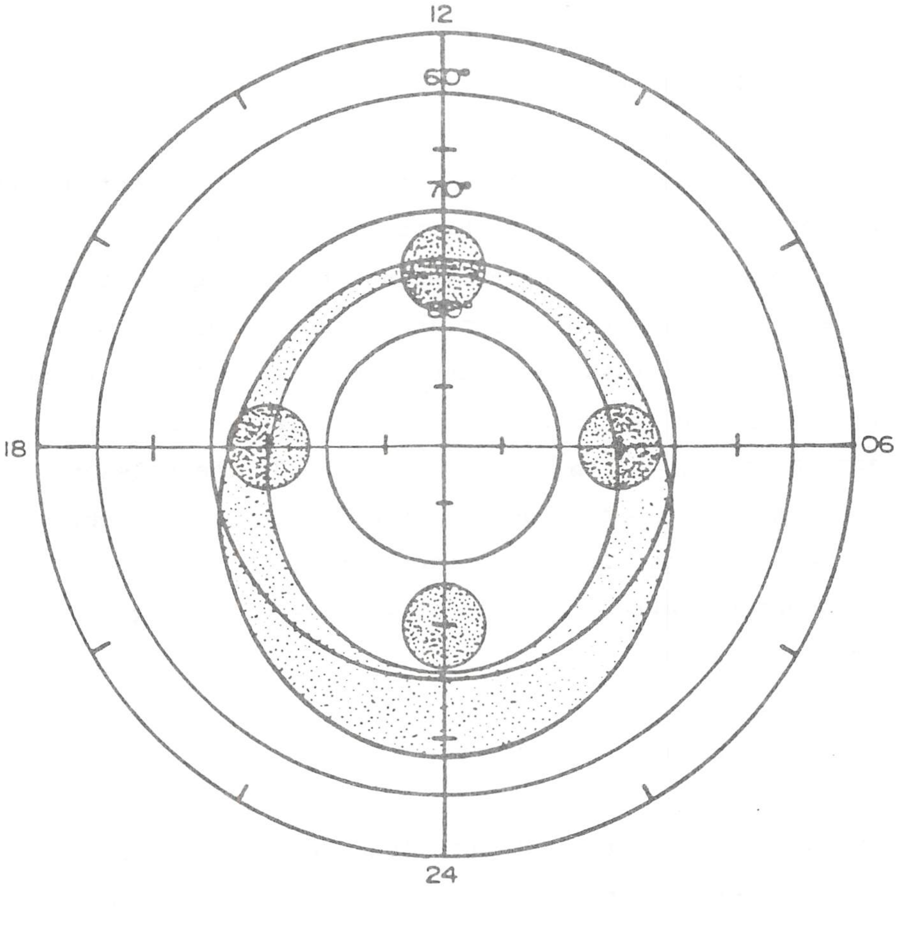

Figure 1. A magnetic local time (MLT) vs invariant latitude plot of the auroral oval with the E-region field of view of a radar located at 75° Λ placed at 06, 12, 18, and 24 hours MLT.

There are many more questions concerning the dayside oval; most can be attacked by analysis of incoherent-scatter radar measurements.

1.2 Polar cap

The polar cap is important for a number of reasons, but primarily because it is the region in which open magnetic field lines merge with the interplanetary field and in which the magnetospheric tail is projected on the ionosphere. The main topics that need investigation are plasma convection and the polar-cap aurora. We need to understand the general morphology (as well as the complex patterns) of plasma convection, polar current systems, and polar-cap aurora. Of keen interest are the relationships between plasma convection, polar aurora, and the orientation of the interplanetary magnetic field.

1.3 The poleward side of the nighttime auroral oval

This region is of interest because it marks the boundary between open and closed geomagnetic field lines. It is a very complex region in which the electric field is characterized by a convection reversal at or near this boundary and in which the pattern of field-aligned currents is often complex.

The key contribution that incoherent-scatter radar can make in the investigation of this region is measurement of ionospheric currents and electric fields at the polar-cap boundary to determine the temporal and spatial variations in relation to substorm activity. Also, during conditions of prolonged substorm inactivity, the auroral oval narrows and moves northward. Incoherent-scatter radar measurements during such conditions can be a very important monitor of the magnetospheric ground state.

1.4 Establishment of a chain of incoherent-scatter radars

Relocating the Chatanika radar to Sondrestrom, Greenland, resulted in establishing a chain of incoherent-scatter radars extending from the magnetic equator to a geomagnetic latitude of 75°. Figure 2 shows the location of the other existing incoherent-scatter radars operated by the United States (Millstone Hill, Massachusetts; Arecibo, Puerto Rico; and Jicamarca, Peru) and the EISCAT and St. Santin radars.

Coordinated measurements by the radars in this chain will enable the scientific study of the thermospheric dynamics on a global scale. Observations along a meridian can be used to distinguish between universal and local-time variations. In addition, the chain can monitor the global thermospheric response to high-latitude phenomena (such as substorms and impulsive heating events) and the equatorward propagation of high-latitude electric fields during magnetic storms (Gonzalez et al., 1979).

1.6 Incoherent-scatter radar capabilities

Incoherent scatter is a powerful technique for investigating ionospheric and atmospheric phenomena for the following reasons:

(1) A large number of geophysical (or ionospheric plasma) parameters can be measured simultaneously by the radar.

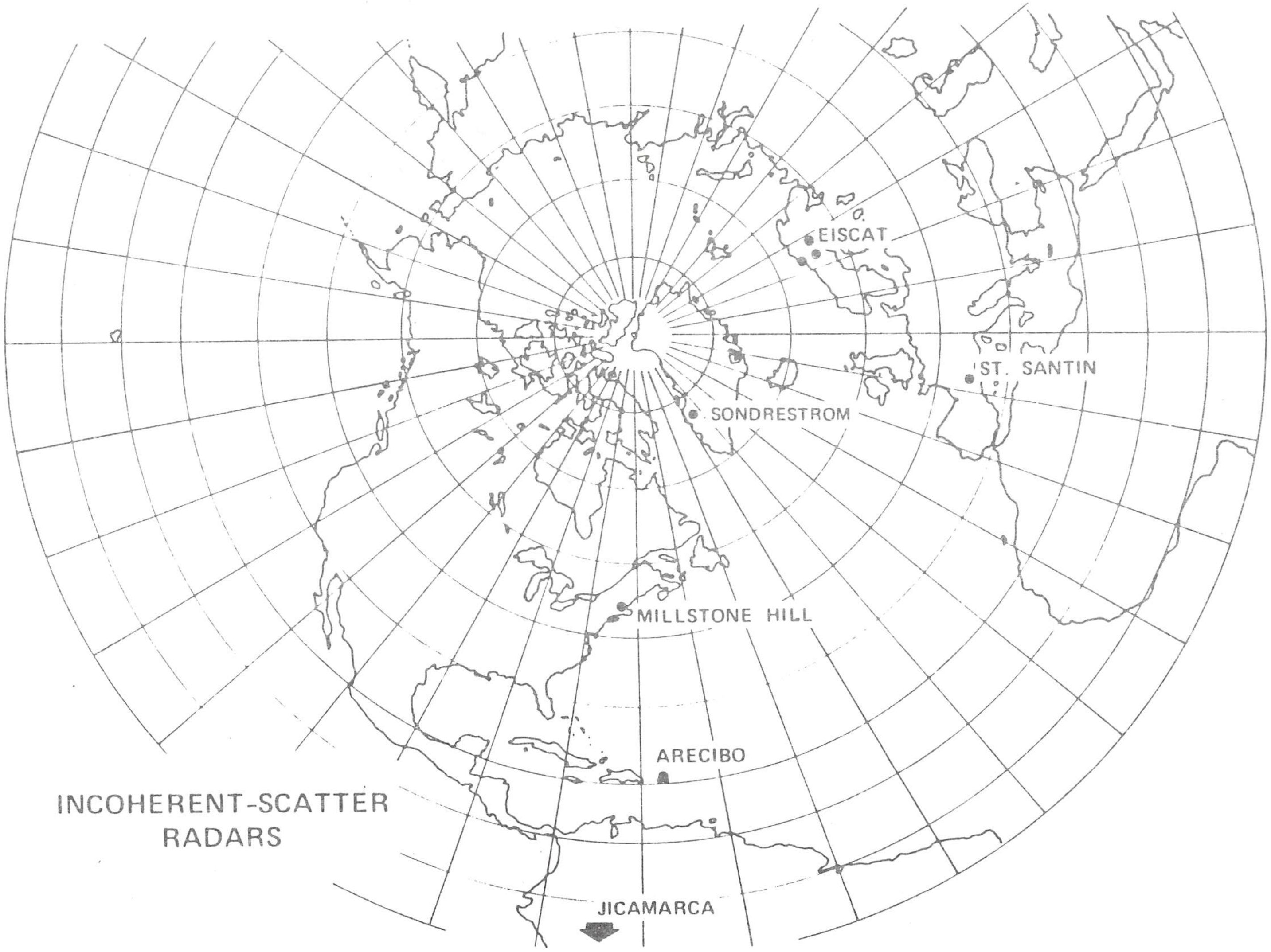

Figure 2. Polar projection of incoherent-scatter radar facilities.

(2) Measurements can be made continuously for periods of many hours.

(3) The radar has the ability to scan spatially.

The measured parameters include electron density, ion velocity, electron-to-ion temperature ratio, and ion-mass-to-ion-temperature ratio. From these basic measurable parameters many other quantities can be derived or inferred (i.e., horizontal and parallel electric fields, ionospheric conductivities, neutral-wind velocities, currents, Joule and particle energy-deposition rates). Table I gives these measured and derived parameters. The usual altitude range of the incoherent-scatter measurements is from 70 to 700 km.

2. THE SONDRESTROM FACILITY

The Sondrestrom radar is located in a small valley approximately 7 miles by road from the Sondrestrom Air Base. The coordinates of the radar site are shown in Table II. Special care was taken to locate the radar so the nearby hills would shield the antenna from the distant mountains and ice cap that would cause ground clutter at ionospheric ranges.

Table I. Measurable and derivable quantities of the Sondrestrom radar.

Quantity	Symbol
Ionospheric--ion line	
Electron density	N_e
Ion temperature	T_i
Electron temperature	T_e
Line-of-sight ion velocity	V_i
Ion velocity	V_R
Ion composition	$[O^+]/N_e$
Ion-neutral collision frequency	ν_{in}
Electric field	$E_\perp$
Exospheric temperature	T_∞
Hall conductivity	σ_H
Pedersen conductivity	σ_P
Current density	$J_\perp$, $J_\parallel$
Neutral wind	U
Meridional neutral wind	U_{MERID}
Recombination coefficient	α
Production rate versus altitude	q(h)
Energy spectrum of auroral primary electrons	f(E)
Energy deposition:	
Particles	Q_e
Joule	Q_J
Ionospheric--Plasma line:	
Plasma frequency	ν_R
Plasma wave phase velocity	ν_φ
Plasma wave phase energy	E_φ
Plasma wave temperature	kT_p
Atmospheric	
Refractive index fluctuations	C_N^2
Winds, horizontal and vertical	U_n

Transportation to and from Sondrestrom Air Base is available commercially or by the U.S Military Air Command (MAC). There are regular commercial flights directly from Copenhagen, Denmark, and from Canada (via Frobisher Bay, Canada and Godthaab, Greenland). The MAC flights originate at McGuire Air Force Base, New Jersey, and are available (with proper clearances) to visitors.

Table II. Coordinates of the Sondrestrom incoherent-scatter radar.

Elevation (m)	177
Geographic	
Latitude (N)	67.0°
Longitude (E)	309.2°
Geomagnetic	
Latitude (N)	74.5°
Inclination	80.5°
Declination (W)	41.6°
L-Shell Value	~ 13.8

The radar system and data-processing systems are described in detail elsewhere (Baron, 1977, Leadabrand et al., 1972). Diesel generators located at the site produce the required primary power. A 600-kW generator provides power solely for the radar transmitting system, a 150-kW generator provides the balance of the electricity for the site, and a second 150-kW generator is a backup.

The antenna for the radar is a completely steerable 32-m-diameter parabolic reflector that uses a Cassegranian feed configuration. Table III lists the significant parameters of the radar in its present configuration.

Table III. Parameters of the Sondrestrom incoherent-scatter radar.

Parameter	Adjustment Range	Normal Operation
Transmit frequency	1280 to 1300 MHz	1290 MHz
Transmit power (peak)	0 to 5 MW	3-4 MW
Duty cycle (maximum)	3%	2.7%
Transmit polarization		RHC
Receive polarization		LHC
Antenna diameter		32 m
Antenna beamwidth (full width, half power)		0.5°
Antenna gain		50 dB
System noise temperature		110°K
Pulse length	10 to 500 μs	60 and 320 μs (alternate IPPs)
Receiver IF bandwidth	$\leqslant$ 10 MHz	50 or 62.5 kHz
Correlator sample interval		8 or 10 μs

Unlike most other incoherent-scatter radars, the SRI system operates at 1290 MHz. This relatively high frequency was a compromise. The frequency is high enough that coherent scatter is minimized and not so high that Debye-length considerations would preclude F-layer studies.

The radar uses an online Harris computer to control the experiment and format the data. With the aid of external digital correlators, the computer provides some real-time data processing. The computer also drives the antenna and generates online data displays for experiment management by the radar operator.

The same computer is used off line to reduce the recorded data--i.e., to convert the measurements of signal power and frequency spectrum into the physically more meaningful parameters of electron density, electron and ion temperature, and plasma drift.

2.1 Other Facilities/Instrumentation at Sondrestrom

Table IV gives a summary of the instrumentation at the extended facility at Sondrestrom. An impressive amount of instrumentation has been set up to take advantage of the radar observations, particularly the optical and the hydromagnetic-wave equipment. In addition to these, Danish scientists have had much instrumentation in the vicinity for a long time.

This year existing equipment have been improved, and new instruments have been added. The Keogram camera was improved and reinstalled for the second half of the winter observing season.

The Lockheed spectrally selective image-intensified all-sky television was upgraded and installed in the optical facility in February 1986. It has a color monitor in the control room. The Lockheed meridian-scanning photometer was also put back into operation in February 1986.

As part of a major campaign in February 1986, the Aerospace Corporation installed a low-resolution Fabry-Perot interferometer for measuring the spectral-width of the emissions of atomic oxygen. It was installed in the optical facility and has been left for future campaigns.

Table IV. Instruments and Facilities at Sondrestrom

Instrument or Facility	Institution
Sondrestrom radar facility	SRI International
Optical facility	University of Michigan
Fabry-Perot interferometer	University of Michigan
Half-meter spectrometer	National Research Council (CN)
6-channel meridian-scanning photometer	Lockheed Research Laboratory
Low-light-level TV and and camera	Lockheed Research Laboratory
Keogram camera	Boston College
Fabry-Perot interferometer	Aerospace Corporation
Magnetometer	Danish Meteorological Institute
30-MHz riometer	Danish Meteorological Institute
All-sky camera	Danish Meteorological Institute
Ionosonde	Danish Meteorological Institute
HF doppler radar	Danish Meteorological Institute
Micropulsation system	University of New Hampshire
Micropulsation system	Bell Laboratory
VLF receivers	Stanford University
HILAT satellite ground station	SRI International
Rocket range	Danish Meteorological Institute and NASA

Stanford University has set up a VLF receiving system at the radar site. This system, covering 10 Hz to 30 Hz, records natural VLF emissions synoptically.

The University of New Hampshire has operated a micropulsation system at Sondrestrom for the last two years. It has search coils that are so oriented that they can detect hydromagnetic waves propagating in the magnetic north-south and east-west directions. In September, a vertical axis search coil will be added.

Bell Laboratory has installed another system for detecting hydromagnetic waves at Sondrestrom. To date it is being used on a campaign basis.

3. SYSTEM UPGRADE PLANS

The Sondrestrom digital system and receiver system is being upgraded to allow:

- Improved spatial coverage.
- Simultaneous E- and F-region measurements without loss of statistical significance, or F-region measurements with greater statistical significance.
- Measurement of Doppler-shifted signals that can be out of the present passband.
- Improved range resolution.
- Pulse-to-pulse correlation for low-altitude measurements.

3.1 Upgrades

The first step in this upgrade entails bringing the now out-of-date Harris S-100 computer up to a supportable and expandable revision level and implementing the GPIB (general purpose interface bus). The following upgrades will be implemented:

- Purchase of an extended addressing kit.
- Purchase of a VOS operation system.
- Purchase of FORTRAN 77.
- Purchase of Harris-to-GPIB interface.

The second step entails upgrading the radar antenna-control system and moving control responsibilities from the Harris to a dedicated microprocessor. This will result in a significant improvement in the reliability and flexibility of the antenna control systems. In addition, the antenna-motor generators will also be replaced by modern silicon-controlled rectifiers (SCR) controllers to eliminate troublesome power fluctuations that occur under the current operating configuration.

The third step substantially upgrades the data-collection hardware, eliminating the restrictions imposed by our present digital equipment. The key item in this modification is the implementation of the NSF funded RSC being developed by Cornell University. As described in Swartz and Johnston (1985), it is designed to provide flexible high-speed preprocessing of radar data. Using a parallel, pipeline architecture, it will be especially well suited for tasks such as calculations of autocorrelation functions, decoding of phase-coded pulses, and coherent and incoherent accumulations. The configuration under development will provide sampling rates up to 10 MHz for each channel of input. In addition to processing modules to do the calculations the RSC will include analog-to-digital converters, a radar timing module (for radar transmitter/ receiver control), and an output data formatter for interfacing the RSC to a Harris computer. Cornell will also develop software for operating the RSC on the Harris computers at the Arecibo and Jicamarca incoherent-scatter radars. It is also appropriate, during this step, to replace our current 75-kHz IF receiver with a baseband receiving system. Finally, the purchase of four computer-controlled frequency synthesizers will provide for the much needed dual-frequency operation described earlier.

These hardware upgrades will require significant modifications to the on-line data-collection program. Using the baseband receiving system and RSC will also affect the data-reduction programs.

Next, we plan to implement Barker coding capability to the system and increase the maximum pulse repetition rate. The addition of Barker coding is a minimal task because the coding-decoding control is provided by the RSC. Only minor modifications to the transmitter would be required. The improvement to increase the transmitted PRF is a larger task. This improvement entails considerable engineering work, but the hardware costs will be minimal.

The final upgrade is the addition of a second CPU (Harris H-800) for data processing. This CPU will provide science-ready data for experimenters in near real time. In addition, this second CPU will help compensate for the increased computation requirements resulting from the added capacity of the digital hardware.

REFERENCES

Baron, M.J. 1977. p. 103 in Radar Probing of the Auroral Plasma, (Ed. A. Brekke), Scandinavian University Books, Oslo, Norway.

Gonzalez, C.A., M.C. Kelley, B.G. Fejer, J.F. Vickrey and R.F. Woodman 1979. J. Geophys. Res. 84, 5803.

Leadabrand, R.L., M.J. Baron, J. Petriceks, and H.F. Bates 1972. Chatanika, Alaska, auroral zone incoherent-scatter facility, Radio Sci. 7, 727.

Swartz, W.E. and P. Johnston 1983, p.513 in Middle Atmosphere Program, Hand Book for Map, (Ed. S.A. Bowhill and B. Edwards), SCOSTEP Secretariat, Univeristy of Illinois, Urbana, IL.

DATA ANALYSIS

WLODEK KOFMAN

1) The sensitivity of the incoherent-scatter spectrum to different ionospheric parameters for different region.

The incoherent-scatter spectrum depends on the following plasma parameters : NE electron density, TE and TI electron and ion temperatures, ψ ion-neutral collisions, p ion composition,ion-electron and electron-neutral collision.

The dependence of the spectrum on ion-electron and electron-neutral collisions is very weak and it is practically impossible to measure these parameters in the F and E regions of the ionosphere. The spectrum depends much more on ψ. In the lower thermosphere (80-110km), it is possible to determine ψ from the measurements. However, to do this, it is necessary to assume that TE = TI. In fact, theoretically, it is possible to determine five parameters ; but in practice, the errors in the determination are so large that the results are meaningless. While this assumption of the temperature equality is correct in the midlatitude ionosphere, it is more questionable in the auroral zone. Under a quiet magnetic conditions this assumption is fulfilled but under disturbed conditions, is often not.
Above 110 km, the incoherent-scatter spectrum is not sensitive to ψ (for a UHF radar) and one assumes ψ = 0 and TE≠TI. In the data analysis, one determines NE, TE, TI, and VI. Another problem arises at altitudes higher than about 130 km due to the changes in ion composition. In the low E region, the major ions are NO^+ and O_2^+, but when the altitude increases,the composition changes and O^+ starts to be the major ion. The ion composition is very difficult to determine from the incoherent-scatter spectrum. In figure 1 we show the errors in the determination of the parametres if one supposes that the correlation function was measured with 1% precision except the first lag which was measured with 2% precision (32 lags). The curves indicates the precision if one assumes the composition known or not . In table 1 we show also the precision on the parameter determination. The error equal zero means that the parameter was fixed in analysis. These calculations were published by Lejeune 1980 and in this paper one can find other curves indicating the precision in the parameters determination.Usually, one assumes the ion composition but unfortunely the wrong assumption leads to a wrong determination of TE, TI, and NE. This is one of the major problems of measurements in the F1 region of the ionosphere. In the midlatitude ionosphere, the assumed model is usually sufficiently good to provide a good determination of the other parameters (or one can assume a knowledge of the other parameters). In the auroral zone, in the presence of particule precipitation and Joule heating, the ion composition can change greatly, with the transition region (50 % heavy ions) increasing from 180 km to 210 km. For these reasons,a data analysis technique with some additional assumptions was developed to determine the ion composition from the measurements (see next section). In the region where the ion composition is known, above about 250km, one easily determines the plasma parameters NE, TE, TI and VI.

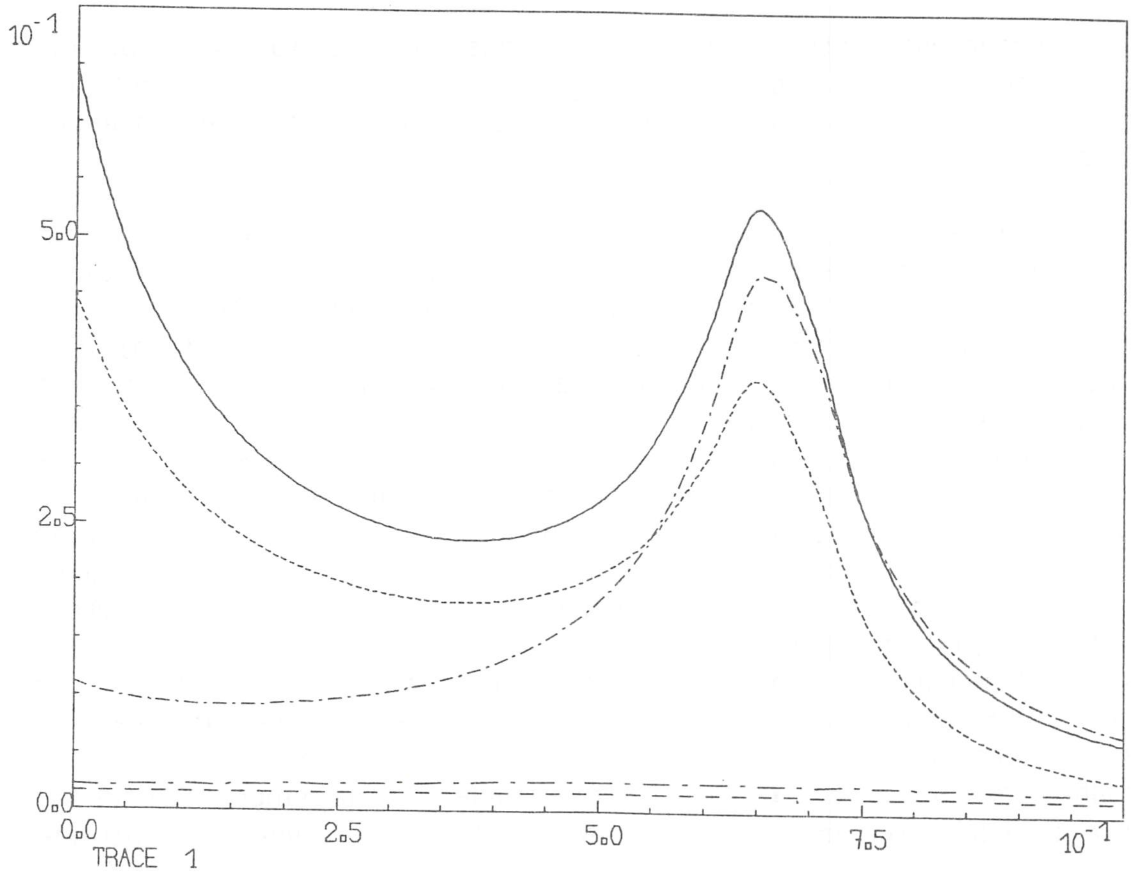

Figure 1

– – – – – – relative error on T_e analysis with fixed composition

— - - - – relative error on T_i analysis with fixed composition

.... relative error on T_e analysis with fitted composition

– – – – relative error on T_i analysis with fitted composition

———— relative error on fitted composition

INCERTITUDES

	Fech (KHz)	Ne (cm^{-5})	T_e (K)	T_i (K)	V_{O^+} (Hz)	$1 - \frac{(O^+)}{Ne}$	n_{in}	$V_e - V_{O^+}$ (Hz)	$V_{O^+} - V_{H^+}$ (Hz)	T_{O^+}/T_{H^+}
Création	50	5	2000	1000	0	0,2 (NO^+)	0			
Incertitude		0,38	362	79	52	0,25	0			
Création		5	2000	1000	0	0,4 (NO^+)	0			
Incertitude		0,20	302	107	0	0,20	0			
Création	25	1	300	300	0	1 (NO^+)	2000			
Incertitude		0,45	174	95	0	0	1066			
Création	100	1	2000	1000	0	0,05 (H^+)	0	0	0	1
Incertitude		0,016	27	21	50	0	0	0	0	0
		0,023	29	24	0	0,006	0	6630	0	0
		0,025	38	28	0	0,006	0	0	1960	0,31
		0	0	0	54	0	0	7910	2280	0

The ion composition problem arises again at very high altitudes where the transition from O^+ ions to He^+ and H^+ ions exists ; it occurs above 500 km.

2) **Measured correlation function : corrections**.

One can show that the observed correlation function is given by the formula :

$$R(\tau) = (R_M(\tau) * R_Z(\tau)) \otimes R_R(\tau)$$

$\circledast$stands for a convolution
R_M is the medium correlation function of the medium
$R_Z = \int z(t-\tau/2-h)\, z^*(t+\tau/2-h)\, dh$
z is the envelop of the transmitted signal
$R_R(\tau) = \int h(t)\, h^*(t+\tau)\, dt$
h represents the receiver impulse response.

This equation can be written in the spectral domain as :

$$S(f) = (S_M(f) \otimes S_Z(f)) * S_R(f)$$

These equations imply that before the data analysis, it is necessary to correct for the effects of the filter and the pulse. length. The correlation function is usually estimated by :

$$R(\tau) = \sum^{N-\tau-1} s(i)s(i+\tau)$$

which gives another correction to the correlation function (s is the received signal) because $E(R(\tau)) = (N-\tau) * r(\tau)$.(E means expected value in the probabilistic sense and $r(\tau)$ the correlation function) Practically, it means the following operations :

a) to multiply the measured function $R(\tau)$ by $1/(N-\tau)$

$$R1(\tau) = R(\tau)/(N-\tau)$$

b) to divide $S1(f)$ by $S_R(f)$ to correct the filter effect

$$S2(f) = S1(f)/S_R(f)$$

c) to divide $R2(\tau)$ by transmitted pulse correlation function

$R3(\tau) = R2(\tau)/R_Z(\tau)$ $R2(\tau)$ = Fourier transform of $S2(f)$

(for single pulse, it is a triangular function)
Finally $R3(\tau)$ represents the estimate of the correlation function of the medium.

The corrections described above are possible only in the case of a sufficiently long correlation function (for which R (max lag) $\simeq 0$) that the Fourier transform is not very different from the true spectrum. If that is not the case, it is necessary to correct the theoretical functions in the regression procedure, which consumes a lot of computer time.

In the case of multipulse measurements, one does not correct for the filter effect. But if it is necessary, as in the case of anomalous heating, one does it on the theoretical functions.

3) Quick parameter determination from measurements.

Let R3(i) be the estimate of the medium correlation function. One can obtain estimates of the ionospheric parameters TE , TI , NE , and VI by simple calculations from the shape of the correlation function. One determines, by interpolation, the value of the first minimum Amin and the first zero crossing Azero. In the spectral representation it corresponds to the spectrum width and the ratio of the peak to the valley. From these two parameters and R3(0) value, one calculates the TE, TI, and NE values for O^+ composition. (Wickwar 1975, Lejeune 1978)

$$\mathrm{Amin} = \mathrm{Amin}/\mathrm{R3}(0)$$

$$\mathrm{C1} = 1 + 2.17 * \mathrm{Amin}\ ,\quad TR = \mathrm{TE}/\mathrm{TI} = (1 - \sqrt{\mathrm{C1}})\ /\ 0.23$$

$$\mathrm{C2} = (1.2548 + 6.7734\ /\ (\mathrm{TR} + 0.9632)) * \lambda_{\mathrm{radar}} \qquad (\lambda_{\mathrm{radar}}\ \text{in meter})$$

$$\mathrm{TI} = (\mathrm{C2}/\mathrm{Azero}) ** 2 * 1\mathrm{E}06 \qquad \text{Azero in } \mu\text{sec}$$

$$\mathrm{TE} = \mathrm{TR} * \mathrm{TI}$$

$$\mathrm{NE} = R_M(0) * (1 + \mathrm{TR}) * \mathrm{Cradar} * (\mathrm{distance}) ** 2/(\tau * P_W)$$

$$\alpha^2 = (4\,\pi\,\lambda_D / \lambda_{\mathrm{radar}})^2 \qquad \alpha^2 = \alpha 0 * \mathrm{TE}/\mathrm{NE} \qquad \alpha 0 \text{ is a constant}$$

$$\mathrm{NE} = R_M(0) * (\alpha^2 + \mathrm{TR} + 1) * (\alpha^2 + 1) * \mathrm{Cradar} * (\mathrm{distance}) ** 2/(\tau * P_W)$$

If one adds the composition model in the F1 region one can calculate revised temperatures. Let $p = 1 - O^+/\mathrm{NE}$

$$\mathrm{TE} = \mathrm{TE} * (0.94 + p - 0.36 * (p - 0.55) ** 3)$$

$$\mathrm{TI} = \mathrm{TI} * (-4.05 - 1.546 * p + 15.65\ /\ (3.1 - p))$$

For instance, for p = 1, TE increases by a factor of 1.90 and TI by 1.86 . This clearly indicates the importance of the composition in the temperature determination. A new value of NE is calculated using TE(p) and TI(p).

The ion velocity ΔF is determined by :

$$2\pi\Delta F = \sum_1^N W(i) * (i-1) * \text{Real}\,(R3(i)) * \text{Im}\,(R3(i)) \,/\, \sum_1^N W(i) * ((i-1) * \text{Re}(R3(i)) **2$$

W(i) weigts .

This procedure is very close to the matched filter estimate developed for the Chatanika radar, except that we use the real part of the correlation function as the matched replica . As we shall see later, this corresponds to the first iteration in the regression procedure.

4) Least mean square fitting of the incoherent scatter spectrum

Let $R3(\tau,x)$ be the estimate of the correlation function of the medium for different lags τ, and $x = (x_1, x_2, \dots x_N)$ be the vector of ionospheric parameters that one would like to determine from the measurements

The theoretical model predicts that the true correlation function is $R_M(\tau,x)$. One supposes that on average $R_M(\tau,x) = E(R(\tau,x))$ which means that the measured correlation function is non biased. The covariance matrix can be defined by :

$$\Gamma = E((R3(\tau,x) - R_M(\tau,x))\,(R3(\tau,x) - R_M(\tau,x)^T)$$

If the observation can be obtained with an infinite precision, it is easy to see that $R3(\tau,x) - R_M(\tau,x) = 0$, for the correct value of x, and for every τ . In practice, it is not possible to measure R3 without errors and one has to find a way to estimate x . The most popular method is least square fitting ; it was proposed for the first time by the mathematician Gauss.

In the estimation theory, we can show that this method corresponds to the statistical one which maximizes likelihood for the normal process. In practice, it means that we have to find the vector x which makes the quadratic minimum form :

$$\delta Y_i = R(i,x) - R3(i,x) \qquad Q = \underline{\delta Y}^T(\underline{x}^{k+1})\,\underline{\Gamma}^{-1}\,\underline{\delta Y}^*(\underline{x}^{k+1}) = \min$$

To find x, we use an iteration procedure based on linearization near the last solution. Let the solution be $\underline{x}^1, \underline{x}^2, \dots, \underline{x}^k$ and $\underline{x}^{k+1} = \underline{x}^k + \underline{\delta x}^k$

$$\underline{\delta Y}(\underline{x}^{k+1}) = \underline{\delta Y}(\underline{x}^k) + D(\underline{x}^k)\,\delta\underline{x}^k$$

D is matrix of derivatives $d_{ij} = \partial R(i,\underline{x}) \,/\, \partial x_j$

To minimize the quadratic form, one has to calculate the solution of $\text{GRAD}_x(Q) = 0$

$$\mathrm{GRAD} = (\partial / \partial x_1, \ldots, \partial / \partial x_n)$$

One obtains the solution :

$$\mathrm{REAL}\ ({}^{T}D(\underline{x}^{k})G^{-1}(\underline{\delta Y}(\underline{x}^{k})+D(\underline{x}^{k})\underline{\delta x}_{k})) = 0.$$

Let : $\Phi = \mathrm{Real}\ ({}^{T}D(\underline{x})\Gamma^{-1}D^{*}(\underline{x}))$, one has :

$$\underline{x}^{k+1} = \underline{x}^{k} + \Phi^{-1}\underline{\Psi} \quad , \text{ where } : \quad \underline{\Psi} = -\ \mathrm{Real}\ (({}^{T}D\Gamma^{-1}\underline{\delta Y}^{*}))$$

and like that one can continue by performing the next iteration. In the particular case of a linear function, one does not need the iteration because the matrix Φ does not change and the solution is found immediately .

The last problem to be solved theoretically is to determine the errors for the parameters determined. After the iteration, when the linearization procedure is entirely valid, we can find the matrix of errors by :

$$\Xi_X = E\ (\ (\underline{x}^{k+1} - \underline{x}^{k})\ (\underline{x}^{k+1} - \underline{x}^{k})^{T})$$

and due to the fact that $\underline{x}^{k+1} - \underline{x}^{k} = \Phi^{-1}\underline{\Psi}$, one obtains with some manipulations that $\Xi_X = \Phi^{-1}$.

The iteration process stops when δx_k is less than some percent of ∂x_i (usually 20 %).

Example :

In the case of the incoherent-scatter measurements, we can write

$$R(i) = R_0(i)\ \exp(j2\pi i\Delta t\Delta F)$$

where R_0 is the ACF without any ensemble drift and R(i) is the measured ACF with a Doppler shift ΔF . If we neglect the differential ion and electron drift, the R_0 is a real function.

Let us suppose that $x_1 = \Delta F'$ and $x_2, \ldots\ldots, x_k$ are the other scalar paramaters. We will calculate the matrix D and Φ in this case.

$$d_{i,1} = \partial R/\partial(\Delta F) = j2\pi i\Delta t * R_0 * \exp(j2\pi i\Delta t\Delta F)$$

$$d_{i,j} = \delta R/\delta x_j = \delta R_0/\delta x_j * \exp(j2\pi i\Delta t\Delta F) \quad j > 1$$

Supposing Γ diagonal, we obtain :

$$\varphi_{11} = \sum_i |d_{i,1}|^2/\sigma_i^2 = \sum_i (2\pi i\Delta tR_0)^2/\sigma_i^2$$

$$\varphi_{1,j} = \mathrm{Real}\ \{ \textstyle\sum_i (j2\pi i\Delta tR_0 * \delta R_0/\delta x_j)/\sigma_i^2 \} = 0 \text{ for } j > 1$$

This relation shows that the velocity parameter is uncoupled from the scalar parameters.

$$\underline{\Psi} = - \mathrm{Re}\{ {}^TD\ \Gamma^{-1}\underline{\delta Y}* \}$$

$$\psi_1 = - \mathrm{Re}\ \{ \textstyle\sum_i (d_{i,1} * \delta Y_i*)/\sigma_i^2 \}$$

$$= - \textstyle\sum_i (2\pi i\Delta tR_0(i) * \mathrm{Im}\ (\exp\ (j2\pi i\Delta t\Delta F * \delta Y_i*) \}\ /\sigma_i^2$$

$$\psi_j = - \mathrm{Re}\ \{ \textstyle\sum_i\ \partial R_0/\partial x_j * \delta Y_i^* * \exp(j2\pi i\Delta t\Delta F)/\sigma_i^2 \}\ j > 1$$

The application of these formulas shows that the determination of the velocity is almost independent of the determination of the other parameters. However, the terms $\varphi_{1,1}$ and ψ_1 contain R_0, which depends on the other parameters : there is still some coupling.

Now we calculate the results of the first iteration. If we assume $\Delta F = 0$ as the initial condition, we obtain :

$$\Delta F_1 = \varphi_{11}^{-1}\psi_1$$
$$= \{ \textstyle\sum 2\ \pi\ i\ \Delta T\ R_0\ \mathrm{Im}\ (\delta Y_i\ )/\sigma_i^2 \} / \textstyle\sum (2\pi i\Delta T\ R_0\ /\ \sigma_i)^2 \}$$

$$\mathrm{Im}\ \delta Y_i = \mathrm{Im}\ Y_i \quad \text{for } \Delta F = 0$$

This formula is very close to the velocity estimate by the matched filter method. The matched filter method uses in fact in the place of R_0, which means the theoretical function, the measured function.

The variance of ΔF estimate is :

$$\sigma_{\Delta F}^2 = \{ \textstyle\sum (2\pi i\ \Delta T\ R_0/\sigma_i)^2 \}^{-1}$$

5) Quality of the fit.

The regression process can diverge if the number of parameters searched for is too large compared with the quality of the data. The quality of each iteration is estimated by the variable :

$$\chi = \{ (\textstyle\sum (\delta Y_i/\sigma_i)^2\ /\ (n - n_p - 1) \}^{1/2}$$

The expected value of χ is 1. If an iteration is successful, χ must decrease. If not, one diminishes the quantity by which the parameters are changed and begins again.

When the process has converged, the value of χ has to be close to 1. If it is the case, the fit is good and the uncertainties on parameters determined in the analysis should be correct. If χ is different from 1 by more than 30 - 50 %, something is wrong . The data can be corrupted by some systematic effect, or the σ_i are not correct, which means that the uncertainties on parameters are wrong by about the same factor.
In some cases, the convergence criterion is so strict that the last increment of the parameters is larger than the uncertainties on those parameters multiplied by the stop criterion . In this case, the maximum iteration is reached before convergence, but χ can be close to 1 , if this is the case, one can keep the results with an appropriate flag.

5-1) Variance of ACF estimator for single pulse measurements

To obtain the ACF of the observed signal, one estimates the ACF of signal plus background noise R_{S+N} and the ACF of noise R_N. Two estimates are calculated on statistically independent S+N and N signals by the procedure described by the equations .

$$R(i) = 1/N_{1p} * \sum_{p} R^p(i) \quad \text{and} \quad R^p(i) = 1/N * \sum_{j=1}^{N-i-1} s(i+j)s(j)$$

To calculate the variance of the estimate, one assumes that the noise and signal are statistically independent gaussian processes and that the estimates of the S+N ACF and the N ACF are independent. The statistical independency of R^p and R^q for $p \neq q$ is also assumed .

$$\begin{aligned} Var(R(i)) &= 1/N_{1p} * 1/N * (1-i/N) * (r^2(i) + \\ &\quad + r^2(0) + 2\sum^{N-i-1}(1-l/(N-i)(r^2(i) + r(l+i)r(l-i)) \end{aligned}$$

$$R_S = R_{S+N} - R_N \qquad E(R(i)) = (1 - i/N)\, r(i)$$

This is the general formula and one can easily calculate, from this formula, the variance of the estimates . In order to see the influence of different parameters on the variance, we will derive the variance for the zero lag in the case of white background noise $r_N(i) = P_N \delta(i)$. In this case the formula has a simple form, which is a good approximation for EISCAT measurements .

$$Var(R_S(0))/P_S{}^2 = 2/N_{ips} * 1/N * \{(1+SNR^{-1})^2 + 2\sum_1{}^{N-1}(1-l/N)\rho^2(l)\} +$$
$$+ 2/N_{ipn} * 1/N * SNR^{-2}$$

$\rho(l) = r_S(l)/r_S(0) \quad SNR = P_S/P_n$

This formula indicates that the variance is a strong function of the SNR, but that it also depends on the bandwidth of the measured spectrum (the $\sum \rho^2(i)$ term is proportional to the bandwidth). For SNR << 1, the variance depends principally on SNR, and for SNR >> 1, the errors depends only on the statistical nature of the signal .

In the data analysis we suppose that the variance of the complex ACF is 0.5{VAR(Re(R)}+VAR(Im(R)} which gives for $i=0$ almost the same formula and for $i \neq 0$ two times less .(ρ^2 is replace by $\rho * \rho^*$) The previous formula corresponds to measured ACF . If one corrects the ACF one has to multiply VAR by the square of the correction factor .

5-2) Variance for multipulse.

The same type of calculation gives us the variance for the multipulse technique :

$$\mathrm{Var}(R_s(i))/P^2{}_s = 1/N_{ip} * ((n+1/SNR)^2 + \rho^2(i))$$

where n is the number of sub pulses in the multipulse

This formula was obtained using the assumption that the clutter power is equal to the signal power In practice, we can estimate the clutter power .

6) Covariance matrix of ACF estimator

In the data analysis, i.e. in the least square fit, the weight matrix that we use is diagonal : it means that we neglect the correlations between the statistical errors of the lags. There are two reasons for that : the correlation between the errors is very low for measurements with the sampling at the Shanon rate and diminishes to zero for SNR << 1, and the procedure that uses the non-diagonal covariance matrix is very complicated and time consuming

For instance,

$$\mathrm{Cov}(\hat{\rho}_l,\hat{\rho}_j) \simeq 1/N_{ip} * ((n+1/SNR)\, \rho_{l-j} + \rho_l \rho_j)) \quad \hat{\rho} \text{ means estimate}$$

for multipulse measurements. One can see that the non-diagonal terms of the matrix are at least one order of magnitude smaller than the diagonal terms for $n = 5$ and $\rho < 0.5$.

For single pulse measurements, the analysis is much more complicated

$$\mathrm{Cov}(\hat{\rho}_k \hat{\rho}_p) \simeq 1/N_{ip} * (1+SNR^{-1})^2 / SQRT((N-k)(N-p)) * \sum_l \rho'(l)\ \rho'(l+p-k)$$

$$\rho' = (\rho_n + \rho_s * SNR) \ / \ (SNR+1)$$

This formula was obtained for non biased estimate of ρ and supposing that the background noise estimate is much precise than signal estimate

G. Lejeune 1980 has shown that, for small SNR, the non diagonal terms are always small, and that sometimes one can have an improvement by oversampling because of the increase in precision of the parameter determination. But, for SNR >> 1, strong oversampling leads to an increase of the non-diagonal terms and the assumption of a diagonal matrix is wrong.

D.T.Farlay , Radio Science, 7, 1972
V.B.Wickwar, SRI Technical Report, 1974
G.Lejeune, Rapport CEPHAG, 36/78
T.Hagfors, EISCAT Technical Note, 1978
G.Lejeune, Seminaire GRECO, 1980
W.Kofman, Seminaire GRECO, 1980
G.Lejeune EISCAT Ann.Rew.Meeting, 1982

ON THE THEORY OF SPORADIC E

T. Nygrén
Department of Physics, University of Oulu
SF-90570 Oulu
Finland

Abstract

The fundamentals of sporadic E theory are reviewed. It is shown how both wind shears and strong auroral electric fields are capable of creating vertical plasma compression leading to the generation of sporadic E-layers. The density profile and thickness for a layer in diffusive equilibrium are discussed.

1. INTRODUCTION

The topic of the present paper is the generation mechanisms of thin horizontal sheets of enhanced plasma density observed in the ionospheric E-region. Such strata are commonly called sporadic E-layers and they are responsible for certain types of sporadic E-traces seen in ionograms (for nomenclature and classification of sporadic E see Piggott and Rawer, 1972). The thickness of a sporadic E-layer is usually of the order of 1 – 2 km and its plasma density may be several times higher than that in the background E-region. Hence it is in these layers where the steepest electron density gradients are encountered in the ionosphere. An example of a sporadic E-layer measured using the EISCAT radar is portrayed in Fig. 1.

The generation of sporadic E-layers can be explained in terms of the *wind shear mechanism*, according to which a vertical shear in the horizontal neutral wind creates convergent vertical ion flow compressing plasma into a thin sheet. This theory was gradually developed during the 1960's (Whitehead, 1960, 1961, 1962; Axford, 1961, 1963; Axford and Cunnold, 1966; Layzer, 1964; Chimonas and Axford, 1968). Attempts have also been made to explain the sporadic E in terms of plasma instabilities or neutral air turbulence, but all these efforts have been unsuccessful. Therefore the simple wind shear theory is generally believed to provide the basic mechanism generating the sporadic E, although instabilities may affect the details of the layer structure. During the last few years, however, it has been realized that vertical plasma compression similar to that caused by wind shears can also be produced by strong

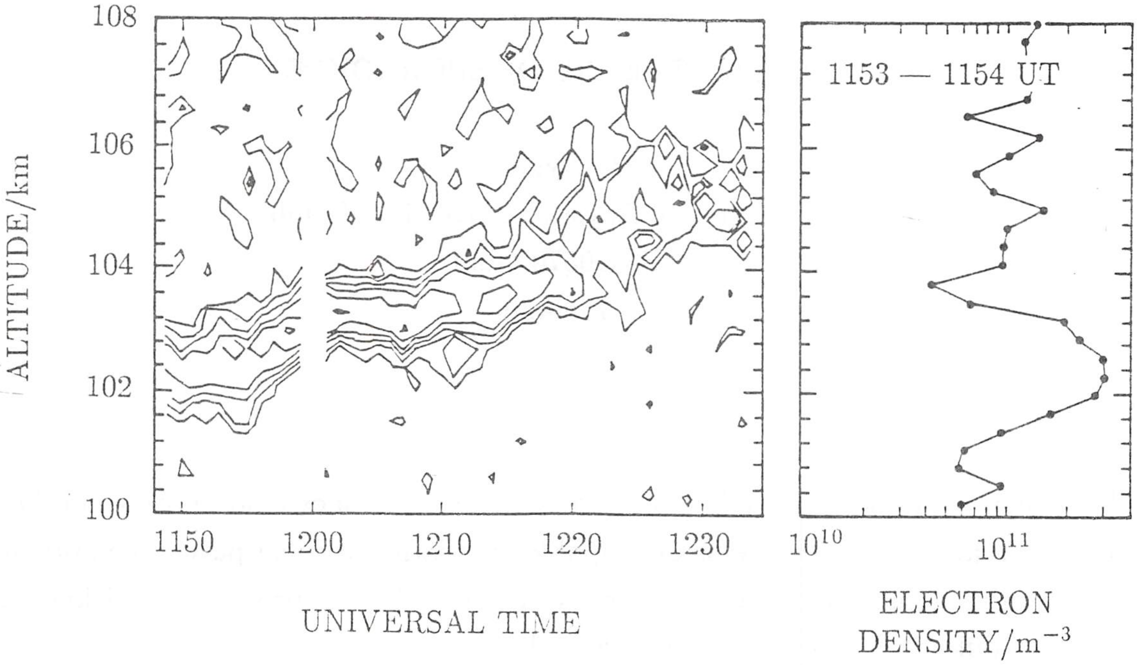

Figure 1. A sporadic E-layer measured with the UHF–radar on 14 August 1986 during the EISCAT summerschool. The height resolution is 300 m. In the first panel contours of constant electron density are drawn. The common logarithm of electron density (in m^{-3}) on the first contour is 11.1 and the interval between the contours is 0.1. The second panel shows a single profile after 1 min postintegration (by courtesy of Dr. T. Turunen).

auroral electric fields (Nygrén et al., 1984). Hence it seems that some layers at high latitudes are actually caused not by wind shears but rather by an *electric field mechanism*. One should point out that the electric field theory (in terms of an effective electric field due to a constant neutral wind) was suggested already in the 1960's by Piddington (1963) but, because the mechanism is not effective at temperate latitudes, not much attention was paid on his work at that time.

2. WIND SHEAR MECHANISM

At E–region altitudes the neutral wind velocity vector may rotate with height creating a vertical shear in the horizontal wind. This structure is often associated with the semidiurnal component of the atmospheric tidal wave. Typically the helix drawn by the velocity vector is a left-handed screw in the northern hemisphere, although right-handed screws are also occasionally encountered. In this chapter the vertical component of the ion velocity caused by such a wind structure is investigated. Throughout the paper stationary state and horizontally stratified ionosphere are assumed.

Northern hemisphere is considered and two Cartesian coordinate systems are used. In NWz-coordinates the N-axis points horizontally to the geomagnetic north, the W-axis to the west and the z-axis vertically upwards, whereas the directions of the axes in $WN_{\perp}z$'-coordinates are horizontally westwards, northwards perpendicular to the geomagnetic field and parallel to the field. Fig. 2 displays the magnetic meridian plane with the two coordinate systems and the geomagnetic induction **B**. Since the representation (A.3) is valid for the mobility tensor in the $WN_{\perp}z$'-coordinates (see the Appendix), it is convenient to carry out the calculations in this system. Then the northward, westward and vertical unit vectors have the representations

$$\mathbf{e}_N = \begin{pmatrix} 0 \\ sinI \\ cosI \end{pmatrix}, \quad \mathbf{e}_W = \begin{pmatrix} 1 \\ 0 \\ 0 \end{pmatrix}, \quad \mathbf{e}_z = \begin{pmatrix} 0 \\ cosI \\ -sinI \end{pmatrix}, \tag{1}$$

where I is the dip angle.

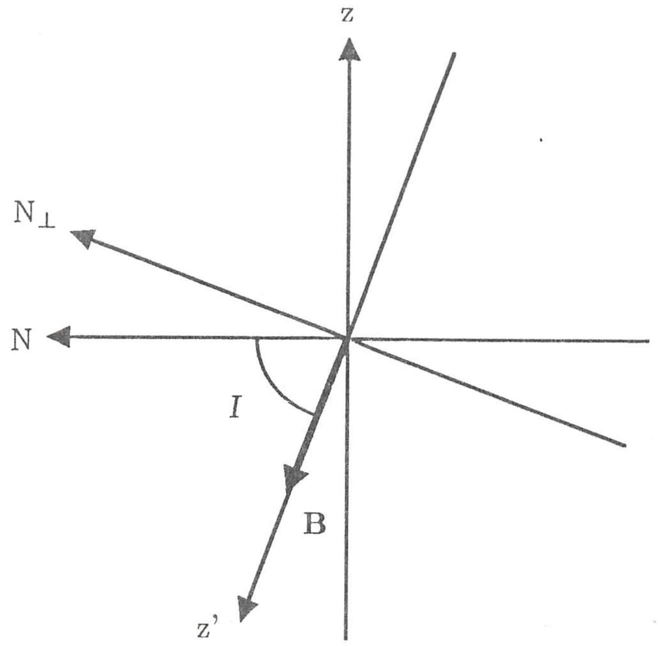

Figure 2. Magnetic meridional plane with the two coordinate systems used. **B** is the geomagnetic induction and I is the dip angle.

The ion convection velocity in the absence of the ambient electric field is given by eq. (A.9) in the form $\mathbf{v}_{ic} = m_i \nu_{in} \mathbf{k}_i \cdot \mathbf{u}$, and its vertical component is

$$v_{icz} = m_i \nu_{in} \mathbf{e}_z \cdot \mathbf{k}_i \cdot \mathbf{u}. \tag{2}$$

If horizontal neutral wind $\mathbf{u} = u_N \mathbf{e}_N + u_W \mathbf{e}_W$ is assumed, the vertical convection velocity is obtained as

$$v_{icz} = m_i \nu_{in} [(\mathbf{e}_z \cdot \mathbf{k}_i \cdot \mathbf{e}_N) u_N + (\mathbf{e}_z \cdot \mathbf{k}_i \cdot \mathbf{e}_W) u_W] \; . \tag{3}$$

This equation contains the zN- and zW-components of the ion mobility tensor and they can be easily calculated using equations (A.3), (A.4) and (1). The results are

$$\begin{cases} k_{izN} = \mathbf{e}_z \cdot \mathbf{k}_i \cdot \mathbf{e}_N = -\dfrac{sinI \cdot cosI}{eB\rho_i (1+\rho_i^2)} \\ k_{izW} = \mathbf{e}_z \cdot \mathbf{k}_i \cdot \mathbf{e}_W = -\dfrac{cosI}{eB(1+\rho_i^2)} \; . \end{cases} \tag{4}$$

Using these formulas eq. (3) can be put in the form

$$v_{icz} = -\frac{cosI}{1+\rho_i^2} (\rho_i \cdot u_W + u_N \cdot sinI) \; . \tag{5}$$

It is convenient to express $\mathbf{u}$ in polar coordinates. When Ψ is defined as the angle between $\mathbf{u}$ and the N-axis, reckoned as positive from north to west, the velocity conponents are $u_N = u \cdot cos\Psi$ and $u_W = u \cdot sin\Psi$, and

$$v_{icz} = -\frac{u \cdot cosI}{1+\rho_i^2} (\rho_i \cdot sin\Psi + cos\Psi \cdot sinI) \; . \tag{6}$$

When the neutral wind has a helical profile, Ψ is a monotonous function of height. If Ψ increases with altitude, the wind screw is right-handed, otherwise left-handed. During a full rotation of the neutral wind velocity vector, the angle Ψ gets all values between 0 and 2π.

The vertical convection velocity is zero, if

$$\rho_i = -\cot\Psi \cdot \sin I \; , \tag{7}$$

which is fulfilled at least two times for each rotation of the wind velocity vector. One of the nulls is obtained within the NE-sector and the other within the SW-sector. Because ρ_i depends on altitude, it is also possible that more than one null is encountered within a single sector. No nulls can be found within the quadrants between north and west or between south and east.

It is essential for the generation of sporadic E–layers that the plasma flows in vertical direction towards a fixed height both from above and from below. This means that, in the case of stationary neutral wind, a sporadic E–layer may be generated at a null given by eq. (7), provided the plasma flow around the null is convergent. The plasma convergence can be investigated by examining the sign of dv_{icz}/dz. By differentiating eq. (6) and using the condition $\rho_i \cdot sin\Psi + cos\Psi \cdot sinI = 0$, the divergence of the vertical convection velocity at the null can be written as

$$\left(\frac{dv_{icz}}{dz}\right)_{zo} = -\frac{u(z_0) \cdot cosI}{1+\rho_i^2(z_0)} \cdot A \cdot sin\Psi(z_0) \ , \qquad (8)$$

where

$$A = -\left[\left|\frac{d\rho_i}{dz}\right|_{zo} + \frac{\rho_i^2(z_0) + sin^2 I}{sinI} \cdot \left(\frac{d\Psi}{dz}\right)_{zo} \right] \qquad (9)$$

and z_0 is the altitude of the null.

The vertical flow is obviously convergent, if $A \cdot sin\Psi(z_0) > 0$ and divergent, if $A \cdot sin\Psi(z_0) < 0$. The quantity A is dependent on the screw pitch and it is positive, if

$$\left(\frac{d\Psi}{dz}\right)_{zo} < -\frac{sinI}{\rho_i^2(z_0) + sin^2 I}\left|\frac{d\rho_i}{dz}\right|_{zo} = -f(z_0) \ , \qquad (10)$$

otherwise negative. Hence A is negative for all right-handed wind screws and also for left-handed screws with $|d\Psi/dz|_{zo} < f(z_0)$. Because $sin\Psi(z_0)$ is positive in the SW-sector and negative in the NE-sector, the rules for convergent and divergent nulls are as shown in Fig. 3. Thus one may conclude that, in the case of a right-handed wind screw, the convergent null is always encountered in the NE-sector, whereas left-handed screws may give convergent nulls in either of the two quadrants.

It is instructive to consider the wind shear mechanism in the cases of high and low altitudes corresponding to small and great values of ρ_i, respectively. When $\rho_i \ll 1$, eq. (5) gives

$$v_{icz} \simeq -u_N \cdot sinI \cdot cosI \ . \qquad (11)$$

This shows that at high altitudes the convection velocity is determined only by the meridional neutral wind and the null lies at an altitude where $u_N = 0$. If the neutral wind has a northward component above and a southward one below this height, the null is convergent and a sporadic E–layer may be created. On the other hand, when $\rho_i \gg 1$,

$$v_{icz} \simeq -\frac{cosI}{\rho_i^2}(\rho_i \cdot u_W + u_N \cdot sinI) \simeq -\frac{cosI}{\rho_i}u_W \ . \qquad (12)$$

Hence the vertical ion motion at low altitudes is caused by the zonal wind. A sporadic E–layer may be created at an altitude where $u_W = 0$, if $u_W > 0$ above and $u_W < 0$ below this height.

The speed of plasma accumulation at the altitude z_0 is described by the divergence presented in eq. (8). At a convergent null the divergence is negative, and the plasma convergence can be defined as $C = -(dv_{icz}/dz)_{zo}$. An order of magnitude estimate of C is obtained by inserting in equations (8) and (9) the numerical values $u(z_0) \simeq 100$ m/s, $(d\Psi/dz)_{zo} \simeq 10°/\text{km}$, $\rho_i(z_0) \simeq 1$ (corresponding to an altitude of about 120 km) and 5 km for the scale height of ρ_i. The result is $C \simeq 10$ m·s^{-1}/km, which is of the same order of magnitude as observed in rocket measurements (MacLeod, 1966). The measured values at the altitudes of sporadic E–layers are often somewhat smaller. This is probably an indication of the wind shear being weaker than that assumed above.

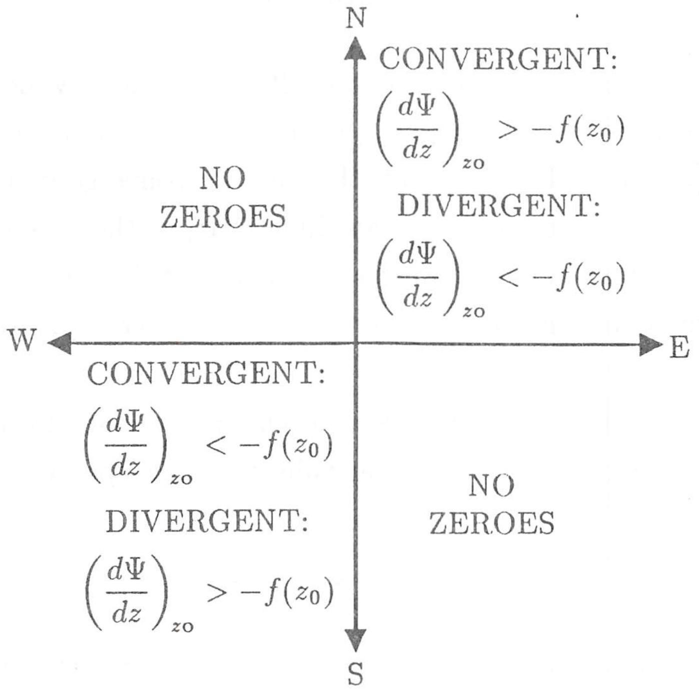

Figure 3. Rules for convergent and divergent nulls in vertical ion velocity according to wind shear theory.

3. ELECTRIC FIELD MECHANISM

In the ionospheric E–region the parallel mobility of electrons is so high that the electric field is practically perpendicular to the geomagnetic field and independent of altitude. At auroral latitudes the electric field may be so strong that it drives ions with a substantially higher speed than the neutral wind does. Although the field has no altitude dependence corresponding to the wind shear, it turns out to be capable of creating a convergent vertical plasma flow very similar to that caused by the wind shear mechanism. This is due to the height dependence of the ion collision frequency and the fact that the strong field is able to drive the plasma fast enough. Hence there seems to be a possibility that some sporadic E–layers at high latitudes are caused by strong electric fields rather than by neutral winds.

A horizontally stratified ionosphere with no neutral wind is assumed. Then, according to eq. (A.9), $\mathbf{v}_{ic} = e\,\mathbf{k}_i \cdot \mathbf{E}_0$, where $\mathbf{E}_0$ is the ambient electric field. Thus the vertical component of the convection velocity is

$$v_{iz} = e\,\mathbf{e}_z \cdot \mathbf{k}_i \cdot \mathbf{E}_0 \ . \tag{13}$$

Since the electric field is perpendicular to $\mathbf{B}$, it can be written in the form $\mathbf{E}_0 = E_{0W}\mathbf{e}_W + E_{0N_\perp}\mathbf{e}_{N_\perp}$ which leads to

$$v_{icz} = e\left[(\mathbf{e}_z \cdot \mathbf{k}_i \cdot \mathbf{e}_W)\,E_{0W} + (\mathbf{e}_z \cdot \mathbf{k}_i \cdot \mathbf{e}_{N_\perp})\,E_{0N_\perp}\right] . \tag{14}$$

The zW-component of the ion mobility tensor needed in this formula is given in eq. (4). The $zN_\perp$-component is calculated in the similar way, and the result is

$$k_{izN_\perp} = \mathbf{e}_z \cdot \mathbf{k}_i \cdot \mathbf{e}_{N_\perp} = \frac{\rho_i \cdot cos I}{eB\,(1+\rho_i^2)} \ . \tag{15}$$

The vertical convection velocity can now be written as

$$v_{icz} = \frac{cos I}{B\,(1+\rho_i^2)}\,(\rho_i \cdot E_{0N_\perp} - E_{0W}) \ . \tag{16}$$

Polar coordinates are again used. When Φ is the angle between $\mathbf{E}_0$ and the $N_\perp$-axis (positive direction westwards from north), the field components can be written in the form $E_{0N_\perp} = E_0 \cdot cos\Phi$ and $E_{0W} = E_0 \cdot sin\Phi$. Using these expressions,

$$v_{icz} = \frac{E_0 \cdot cos I}{B\,(1+\rho_i^2)}\,(\rho_i \cdot cos\Phi - sin\Phi) \ . \tag{17}$$

When comparing this formula with eq. (6), one must remember that, unlike Ψ, Φ is independent of height.

When the electric field direction lies within the SW-sector, $cos\Phi < 0$ and $sin\Phi > 0$. Then eq. (17) shows the vertical convection velocity to be negative at all altitudes, which indicates downward plasma flow. Similarly, it is seen that field directions within the NE-sector always lead to upward motion. The other two quadrants, however, are quite different. Evidently, $v_{icz} = 0$ when

$$\rho_i = tan\Phi \; . \tag{18}$$

Since $\rho_i > 0$ and decreases with height, this condition is always fulfilled at some altitude for any field direction within the NW- or SE-sector. Hence a null in the vertical ion velocity may be present, although the plasma is driven by an electric field only, and the field direction is the same throughout the E–region.

The type of the null can now be investigated using the divergence of the convection velocity. If z_0 is the altitude of the null given by eq. (18), the divergence at the null is

$$\left(\frac{dv_{icz}}{dz}\right)_{zo} = -\frac{E_0 \cdot cosI}{B}\left|\frac{d\rho_i}{dz}\right|_{zo} \cdot cos^3\Phi \; . \tag{19}$$

Hence convergent flow is obtained, when $cos\Phi > 0$, i.e. within the NW-sector. The opposite quadrant gives divergent plasma motion.

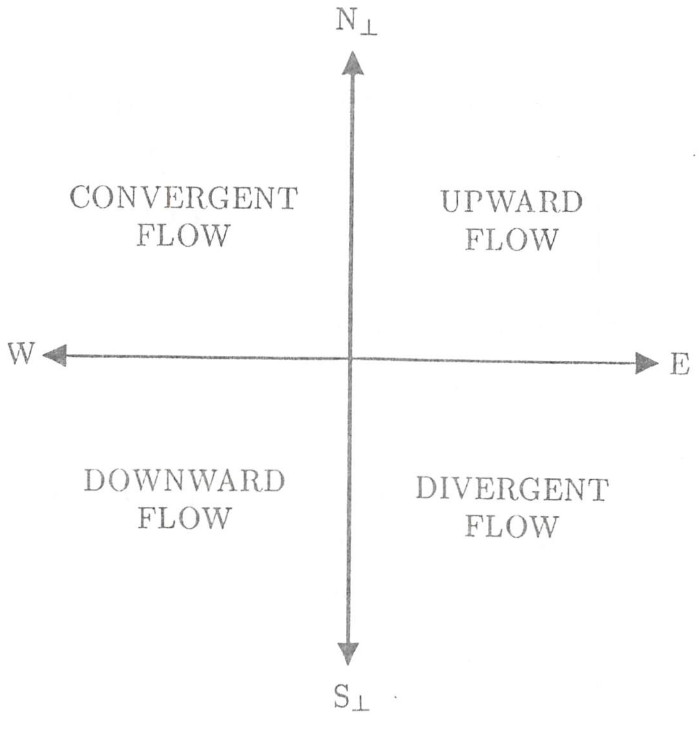

Figure 4. The four types of vertical plasma motion caused by electric field.

In conclusion, an electric field may create vertical plasma motion of four different types: upward, downward, convergent and divergent. The type is determined by the electric field direction as shown in Fig. 4. A possibility for sporadic E generation exists, when the flow is convergent, i.e. when the field points in some direction between north and west.

In order to study whether the electric field is able to compress the E–region plasma as effectively as the neutral wind does, the numerical value of the vertical convergence $C = -(dv_{iCz}/dz)_{zo}$ is finally investigated. According to eq. (18), $\rho_i(z_0) = 1$, if $\Phi = 45°$. This value corresponds to an altitude of about 120 km. Using $E_0 = 10$ mV/m, $B = 50$ μT and 5 km for the scale height of ρ_i, eq. (19) gives $C \simeq 14$ m·s^{-1}/km$\times cos I \simeq 4$ m·s^{-1}/km, if $I = 75°$. Hence the strong auroral electric fields of tens of millivolts per meter are able to create quite similar convergent motion as the wind shear mechanism does. However, the altitude dependence of convergence caused by electric field is different from that due to neutral wind (for details, see Nygrén et al., 1984).

4. LAYER SHAPE

It was shown above that both wind shears and electric fields may create vertical plasma compression, and it was assumed that such plasma motion would lead to the generation of a sporadic E–layer. In this chapter the electron density profile in the presence of convergent plasma motion is investigated in more detail. In order to obtain the density profile, the continuity equation must be solved. It contains the ion velocity, which is the sum of convection and diffusion velocities. The convection velocity is caused by neutral winds or electric fields, and the diffusion velocity depends on the density gradient as shown by eq. (A.10).

It is assumed that the vertical convection velocity profile is convergent around a null located at an altitude z_0. The diffusion velocity is obtained using equations (A.10) and (A.11) and the fact that the density gradient is vertical in a horizontally stratified ionosphere (i.e. $\nabla n = dn/dz \cdot \mathbf{e}_z$). The vertical component of the diffusion velocity is

$$v_{idz} = -(\mathbf{e}_z \cdot \mathbf{D}_a \cdot \mathbf{e}_z) \cdot \frac{1}{n} \cdot \frac{dn}{dz} = -D_{azz} \cdot \frac{1}{n} \cdot \frac{dn}{dz} \; . \qquad (20)$$

This equation contains the zz-component of the ambipolar diffusion tensor, which is calculated in the same way as the components of the mobility tensor were obtained above. It can be written in the form

$$D_{azz} = k_B\,(T_i + T_e) \cdot \frac{\rho_i^2 + sin^2 I}{eB\rho_i\,(1 + \rho_i^2)} \; . \tag{21}$$

Diffusion velocity is important in sporadic E theory, because the density gradients at the layers are extremely steep.

Two-atomic ions with a production rate q and a dissociative recombination coefficient α are first assumed. Then the stationary continuity equation and the vertical ion velocity are

$$\begin{cases} \dfrac{d}{dz}\,(nv_{iz}) = q - \alpha n^2 \\ v_{iz} = v_{icz} - D_{azz} \cdot \dfrac{1}{n} \cdot \dfrac{dn}{dz} \; . \end{cases} \tag{22}$$

The maximum electron density due to plasma convergence can be estimated using these equations as follows. The total velocity v_{iz} is inserted in the continuity equation and all terms containing dn/dz are put equal to zero. Then the maximum density can be solved in the form

$$n_{max} = \frac{1}{2\alpha} \cdot \left[\sqrt{C^2 + 4\alpha\left(q + D_{azz}\frac{d^2n}{dz^2}\right)} + C \right] < \frac{\sqrt{C^2 + 4\alpha q} + C}{2\alpha} \; , \tag{23}$$

where C is the plasma convergence at the peak of the layer. Here the inequality is valid, because $d^2n/dz^2 < 0$ at the layer maximum. If the electron density in the absence of vertical convection is n_0, the production rate is $q = \alpha n_0^2$. The dissociative recombination coefficient for E–region ions is $\alpha \simeq 10^{-13}$ m^3/s. As estimated above, the plasma convergence caused by the wind shear or electric field mechanism is of the order of 10 m·s^{-1}/km or smaller. When $n_0 = 5 \times 10^{10}$ m^{-3} (corresponding to a plasma frequency of 2 MHz) and the above values are used, formula (23) gives $n_{max} < 1.2 \times 10^{11}$ m^{-3} ($\simeq$ 3 MHz). This shows that great enhancements of plasma density such as those present in sporadic E–layers cannot be produced by vertical compression. The physical explanation for this result is that two-atomic ions can be transferred to the layer only from distances shorter than the path they can travel during their life time.

When the density profile is solved numerically from equations (22), the results are in agreement with the above estimate. Furthermore, the profile is found to be deformed within a relatively wide altitude region, which means that, even if some enhancement in electron density is possible, no thin layer can be formed.

A solution to the problem is offered by the presence of metal ions (e.g. Fe^+ and Mg^+) in the ionospheric E–region. These ions are thought to be of meteoric origin, and some evidence of them in sporadic E–layers exists. The fact that they are monoatomic prevents them from decaying via dissociative recombination. Furthermore, their ionization potentials are smaller than those of the common atmospheric molecules, and therefore they cannot be neutralized by charge exchange. The remaining prosess is the extremely slow radiative recombination with a rate coefficient of about 10^{-18} m^3/s. This means that the ions can survive for weeks, and therefore they most probably disappear from the E–region altitudes via convection or diffusion.

In the time scale of sporadic E–layer generation or decay it is a good approximation to put the production rate and recombination coefficient to zero for metal ions. Hence a fixed amount of metal ions is assumed in the E-region. Then the continuity equation has a simple solution nv_{iz} = constant. The boundary conditions show that the integration constant must be zero, and therefore $v_{iz} \equiv 0$. Now the second equation in (22) gives

$$D_{azz} \cdot \frac{1}{n} \cdot \frac{dn}{dz} = v_{icz} \ . \tag{24}$$

Hence the convection velocity is balanced by the diffusion velocity and the ions are not in vertical motion.

Eq. (24) can be easily integrated, and the resulting density profile is

$$n = n(z_0) \cdot exp\left[\int_{zo}^{z} \frac{v_{icz}}{D_{azz}}\, dz \right] . \tag{25}$$

In a convergent velocity profile v_{icz} is positive below the null at z_0 and negative above. Then eq. (24) obviously represents a layer with a peak density $n(z_0)$. The maximum density is a free parameter and it is determined by the amount of long-lived metal ions available. This means that the neutral wind or the electric field sweep all metal ions into a single sheet from an altitude region where the plasma flows towards z_0. During this process the diffusion velocity increases together with the steepening of the density gradient, until it can compensate the convection velocity. The final result is a stationary layer with a density profile shown in eq. (25).

In order to estimate the thickness of the layer predicted by the above theory, it is assumed that D_{azz} = constant and the vertical convection velocity is a linear function of height, i.e. $v_{icz} = -C\,(z - z_0)$. These assumptions are a good approximation at least within some narrow altitude region around the null. The integral in eq. (25) can now be calculated and the resulting profile has a Gaussian form

$$n = n(z_0) \cdot exp\Big[-\frac{C\,(z-z_0)^2}{2D_{azz}}\Big]. \tag{26}$$

The thickness at half-maximum of this layer is

$$\Delta z = 2 \cdot \sqrt{\frac{2D_{azz} \cdot ln2}{C}} \quad . \tag{27}$$

This shows that the layer thickness is determined by the ambipolar diffusion coefficient and the plasma convergence. A thin layer is possible, if C is great or D_{azz} is small. The value of C is controlled by the strength of the wind shear and the wind speed or the electric field intensity. The diffusion coefficient is small at low altitudes where the ion-neutral collision frequency is great.

When $\rho_i \simeq 1$, $T_i = T_e \simeq 500$ K and $B \simeq 50\ \mu$T, the ambipolar diffusion coefficient is $D_{azz} \simeq 2 \times 10^3\ \mathrm{m}^2/\mathrm{s}$. This corresponds to an altitude of about 120 km. If $C = 10\ \mathrm{m{\cdot}s^{-1}/km}$, this diffusion coefficient gives a layer thickness of $\Delta z \simeq 1$ km, and even $C = 2\ \mathrm{m{\cdot}s^{-1}/km}$ leads to $\Delta z \simeq 2.5$ km. It was estimated above that both the wind shear mechanism and the electric field mechanism are capable of creating a convergence of this order of magnitude. Hence it can be concluded that both mechanisms are able to compress metal ions into a thin sporadic E–layer. A necessary condition for the generation of a pronounced layer is the presence of a sufficient amount of long-lived ions.

5. DISCUSSION

In the present paper the main ideas of the wind shear and electric field mechanism are introduced. The ionospheric E–region is, of course, more complicated than the above simplified model. Some of the aspects to be included in a more advanced theory are considered in this chapter. An interested reader will find more information on sporadic E in a review article by Whitehead (1970).

In addition to the long-lived metal ions forming the sporadic E–layer, the normal background ionization is present in the E-region. Therefore continuity equations for two different ion species should be solved. The matter is complicated by the fact that the equations are coupled, but the main consequence of the analysis can be understood in a simple way as follows. Consider that the density of metal ions is n_m and the density of two-atomic ions is n_i and n_o inside and outside of the layer, respectively.

If plasma transport is neglected in the continuity equation, the production rate of two-atomic ions is $q = \alpha n_o^2$. Since q does not change strongly with height, the same value can be used within the layer as well as in its surroundings. At the layer maximum the electron density is $n_e = n_i + n_m$, and the production rate is equal to $q = \alpha n_i n_e = \alpha n_i (n_i + n_m)$. When the two expressions for q are put equal and n_i is solved, the result is

$$n_i = \frac{1}{2} \cdot \left(\sqrt{n_m^2 + 4n_o^2} - n_m \right) . \tag{28}$$

This equation shows that, necessarily, $n_i \leq n_o$. Hence the density of two-atomic ions is not increased but, on the contrary, it is diminished at the layer altitude. This result is caused by increased recombination rate due to the enhanced electron density within the layer. If $n_o = 5 \times 10^{10}$ m^{-3} (corresponds to a plasma frequency of about 2 MHz) and $n_m = 2 \times 10^{11}$ m^{-3}, eq. (28) gives $n_i = 1.2 \times 10^{10}$ m^{-3}. This shows that a majority of background ions may disappear at the layer altitude.

In a more complete theory the time-dependent equations should be investigated and the generation and decay of sporadic E–layers should be studied. The time dependence of the neutral wind should also be taken into account. The screw-like structure associated with semidiurnal tides rotates in the course of time in such a way that the convergent nulls move downwards. The sporadic layers tend to follow the motion of the nulls. Hence layers formed at high altitudes gradually descend through the E–region during a period of several hours. These sequential layers are observed diurnally in two waves. In the lower E–region the collision frequency is high and only slow ion motion is possible, and therefore the layers can no more follow the motion of the null. The result is that they remain floating at so called dumping altitude.

The effects of neutral wind and electric field are studied separately in this paper, although both of them are simultaneously present in the ionosphere. However, their relative importance varies, and therefore the pure wind shear and electric field theory can be considered as two extreme cases of the general situation, where both mechanisms are effective. Also the assumption of strictly horizontal neutral wind is not always true. It can be shown that even small vertical winds can significantly change the altitudes of the convergent nulls.

The true ionosphere is not horizontally stratified, but the layer has a limited horizontal extent and often also a small or large scale internal structure. The layer profile may considerably depart from the Gaussian form: it may have a flat top or two maxima. These phenomena are probably associated with turbulence, plasma instabilities or the presence of more than one long-lived ion species.

The EISCAT facility gives an interesting possibility for sporadic E research at high latitudes. Previously sporadic E has been investigated successfully at lower latitudes using the Arecibo radar (e.g. Miller and Smith, 1978) and some work using EISCAT has also been done (Turunen et al., 1985). It is hoped that the high spatial resolution and level of performance offered by the EISCAT system will be utilized more extensively for this purpose in the future.

ACKNOWLEDGEMENTS

The experiment allowing the high resolution measurement of the sporadic E shown in Fig. 1 was planned by Dr. T. Turunen. The author is grateful to him for the data and also wants to thank Mr. A. Huuskonen for carrying out the data analysis and Dr. L. Jalonen for fruitful discussions.

APPENDIX

The purpose of this appendix is to review briefly the mobility and ambipolar diffusion in magnetized plasma. Consider the stationary momentum equation for a charged particle species x:

$$q_x n_x(\mathbf{E} + \mathbf{v}_x \times \mathbf{B}) - \nabla p_x - n_x m_x \nu_{xn}(\mathbf{v}_x - \mathbf{u}) = 0 \; . \tag{A.1}$$

Here q_x, n_x, $\mathbf{v}_x$, p_x and m_x are the electric charge, number density, bulk velocity, partial pressure and mass of the x-particles, ν_{xn} is their collision frequency with neutral molecules, $\mathbf{E}$ is the electric field, $\mathbf{B}$ is the magnetic induction and $\mathbf{u}$ is the bulk velocity of the neutrals.

The solution of the momentum equation can be put in the form

$$\mathbf{v}_x = \mathbf{k}_x \cdot \left(q_x \mathbf{E} + m_x \nu_{xn} \mathbf{u} - \frac{1}{n_x} \nabla p_x\right) \; , \tag{A.2}$$

where

$$\mathbf{k}_x = \begin{pmatrix} k_{xP} & k_{xH} & 0 \\ -k_{xH} & k_{xP} & 0 \\ 0 & 0 & k_{x\parallel} \end{pmatrix} \tag{A.3}$$

is the mobility tensor in a coordinate system with the third axis parallel to $\mathbf{B}$. The components of $\mathbf{k}_x$ are

$$\begin{cases} k_{xP} = \dfrac{1}{q_x B} \cdot \dfrac{\rho_x}{1+\rho_x^2} \\ k_{xH} = \dfrac{1}{q_x B} \cdot \dfrac{1}{1+\rho_x^2} \\ k_{x\|} = \dfrac{1}{m_x \nu_{xn}} = \dfrac{1}{q_x B \rho_x} \end{cases} \tag{A.4}$$

and they are called the Pedersen, Hall and parallel mobility, respectively. In these formulas $\rho_x = \nu_{xn}/\omega_x$ is the collision frequency normalized by the angular gyrofrequency $\omega_x = q_x B/m_x$.

Eq. (A.1) is separately valid for ions (x = i) and electrons (x = e). Because electrons are very light, they can easily move along the magnetic field and thus effectively prevent any significant departures from charge neutrality. Therefore, in the presence of only one singly charged ion species one can write $n_i = n_e = n$, $q_i = e$ and $q_e = -e$, where e is the positive elementary charge.

When $\rho_e \ll 1$, the momentum equation for electrons is simplified in the form

$$-en\left(\mathbf{E} + \mathbf{v}_e \times \mathbf{B}\right) - \nabla p_e = 0 \ . \tag{A.5}$$

Such conditions are encountered in the ionospheric E–region where $\nu_{en} \leq 10^4$/s and $\omega_e \approx 10^7$/s. The same approximation, however, cannot be made for E–region ions, since $\rho_i = 1$ usually at about 120 km altitude. It is useful to divide the electric field into two vector components

$$\begin{cases} \mathbf{E}_0 = -\mathbf{v}_e \times \mathbf{B} \\ \mathbf{E}_d = -\dfrac{1}{en} \nabla p_e \ . \end{cases} \tag{A.6}$$

Then $\mathbf{E}_0 + \mathbf{E}_d$ obviously satisfies eq. (A.5). Since $\mathbf{E}_d$ depends on the pressure gradient only, it is called the diffusion field. The diffusion field is generated by the plasma itself, and therefore $\mathbf{E}_0$ is the ambient electric field.

The momentum equation of ions is next investigated. By taking advantage of the expression for $\mathbf{E}_d$ one gets

$$en\left(\mathbf{E}_0 + \mathbf{v}_i \times \mathbf{B}\right) - \nabla\left(p_i + p_e\right) - nm_i\nu_{in}\left(\mathbf{v}_i - \mathbf{u}\right) = 0 \ . \tag{A.7}$$

The ion velocity is now divided into two vector components by writing $\mathbf{v}_i = \mathbf{v}_{ic} + \mathbf{v}_{id}$ and choosing $\mathbf{v}_{ic}$ to be the solution of the momentum equation in the absence of pressure gradients. Then the equations for $\mathbf{v}_{ic}$ and $\mathbf{v}_{id}$ are

$$\begin{cases} en\left(\mathbf{E}_0 + \mathbf{v}_{ic} \times \mathbf{B}\right) - nm_i\nu_{in}\left(\mathbf{v}_{ic} - \mathbf{u}\right) = 0 \\ en\mathbf{v}_{id} \times \mathbf{B} - \nabla\left(p_i + p_e\right) - nm_i\nu_{in}\mathbf{v}_{id} = 0 \ , \end{cases} \tag{A.8}$$

and their solutions are given by

$$\begin{cases} \mathbf{v}_{ic} = \mathbf{k}_i \cdot (e\mathbf{E}_0 + m_i \nu_{in} \mathbf{u}) \\ \mathbf{v}_{id} = -\frac{1}{n} \mathbf{k}_i \cdot \nabla (p_i + p_e) \ . \end{cases} \tag{A.9}$$

This result shows that $\mathbf{v}_{ic}$ depends on the ambient electric field and neutral wind only, whereas $\mathbf{v}_{id}$ is determined exclusively by the pressure gradients. Therefore, in this paper the names convection and diffusion velocity are adopted for $\mathbf{v}_{ic}$ and $\mathbf{v}_{id}$, respectively.

When the ion and electron gases are assumed to obey the ideal gas law and the temperature gradients are neglected, the expression for diffusion velocity can be written as

$$\mathbf{v}_{id} = \frac{k_B (T_i + T_e)}{n} \mathbf{k}_i \cdot \nabla n \ , \tag{A.10}$$

where k_B is the Boltzmann's constant and T_i and T_e are the ion and electron temperatures. Using this equation the ambipolar diffusion tensor

$$\mathbf{D}_a = k_B (T_i + T_e) \mathbf{k}_i \tag{A.11}$$

can be defined. It determines the diffusion rate of ions in magnetoplasma. Although charge neutrality was formally assumed in the above theory, the diffusion field $\mathbf{E}_d$ is actually created by a very small charge density in the regions where $\nabla \cdot \mathbf{E}_d \neq 0$. Via this field the electrons affect the ion diffusion. This fact is indicated by the presence of T_e in the formula for the ambipolar diffusion tensor.

REFERENCES

Axford, W.I. 1961. Note on a mechanism for the vertical transport of ionization in the ionosphere, Can. J. Phys. 39, 1393.

Axford, W.I. 1963. The formation and vertical movement of dense ionized layers in the ionosphere due to vertical wind shears, J. Geophys. Res. 68, 769.

Axford, W.I. and Cunnold, D.M. 1966. The wind-shear theory of temperate zone sporadic E, Radio Sci. 1, 191.

Chimonas, G. and Axford, W.I. 1968. Vertical movement of temperate-zone sporadic E layers, J. Geophys. Res. 73, 111.

Layzer, D. 1964. Generalization and critique of the wind-shear theory of sporadic E, J. Geophys. Res. 69, 1853.

MacLeod, M.A. 1966. Sporadic E theory. I. Collision-geomagnetic equilibrium, J. Atmos. Sci. 23, 96.

Miller, K.L. and Smith, L.G. 1978. Incoherent scatter radar observations of irregular structure in mid-latitude sporadic E layers, J. Geophys. Res. 83, 3761.

Nygrén, T., Jalonen, L., Oksman, J. and Turunen, T. 1984. The role of electric field and neutral wind in the formation of sporadic E–layers. J. Atmos. Terr. Phys. 46, 373.

Piddington, J.H. 1963. Ionospheric drifts and E–region irregularities, Planet. Space Sci. 11, 639.

Piggott, W.R. and Rawer, K. 1972. U.R.S.I. Handbook of Ionogram Interpretation and Reduction, World Data Center A for Solar-Terrestrial Physics, Report UAG-23.

Turunen, T., Silén, J., Nygrén, T. and Jalonen, L. 1985. Observation of a thin E_s–layer by the EISCAT radar, Planet. Space Sci. 33, 1407.

Whitehead, J.D. 1960. Formation of the sporadic E layer in the temperate zones, Nature 188, 567.

Whitehead, J.D. 1961. The formation of the sporadic E layer in the temperate zones, J. Atmos. Terr. Phys. 20, 49.

Whitehead, J.D. 1962. The formation of a sporadic E layer from a vertical gradient in horizontal wind, p. 276 in Ionospheric Sporadic E (ed. E.K. Smith and S. Matsushita), Pergamon Press, New York.

Whitehead, J.D. 1970. Production and prediction of sporadic E, Rev. Geophys. Space Phys. 8, 65.

Radar Software for Tristatic Incoherent Scatter Experiments

Walter Schmidt
EISCAT Scientific Association
S-981 28 Kiruna
Sweden

A. Introduction

The tristatic EISCAT radar system is designed with very flexible hardware devices. This makes a whole range of experiments possible. The process computers and their software have to be optimized to control all parts of the radar from any EISCAT site in an user friendly and fast way without imposing any constraint on their flexibility. Experiments which can be tested or shall be repeated unaltered demand the execution of a predefined set of instructions in a given time sequence. Other experiments like the ground based support of rocket measurements need the interaction between operator and hardware to adapt the radar to the changing experiment conditions. Both objectives are met in the implementation of the EISCAT Realtime Operating System (EROS), a set of about 60 concurrently active real-time programs mainly written in FORTRAN with a total of about 57,000 statements.

B. General EROS Program and Command Structure

The current design of EROS is based on a set of independent programs, each controlling or monitoring one specific sub part of the radar system. A program can be activated by an external event (e.g. the correlator data transfer signal), after a predefined time (e.g. the transmitter monitoring) or by an EROS command.

All these programs have the same basic structure: Commands are placed in an input mailbox. The commands are sequentially executed by initiating the intended hardware change, until the mailbox is empty. Possible messages are rooted through an output part to the control terminal or other logging devices.

Informations like commands or messages are exchanged between the programs in the form of buffers with a the same structure: An identifyer defining source and destination site of the information is followed by a command code and additional parameters where needed. There are 3 main sources for commands:

- The command processor interpretes the interactive commands entered via the keyboard of the command terminal and translates them into the internal message format. The operator is prompted for missing parameters
- The experiment runtime supervisor fetches the pre-compiled instructions at the correct times and displays the original command text on the command terminal
- The communication line monitor accepts command buffers from other sites.

In each case the command buffer is routed to the intended executer program at the specified site(s).

A general error logging program collects all messages from the system, decodes them where necessary and distributes them to the

Simplified EROS Block Diagram UHF Tromso

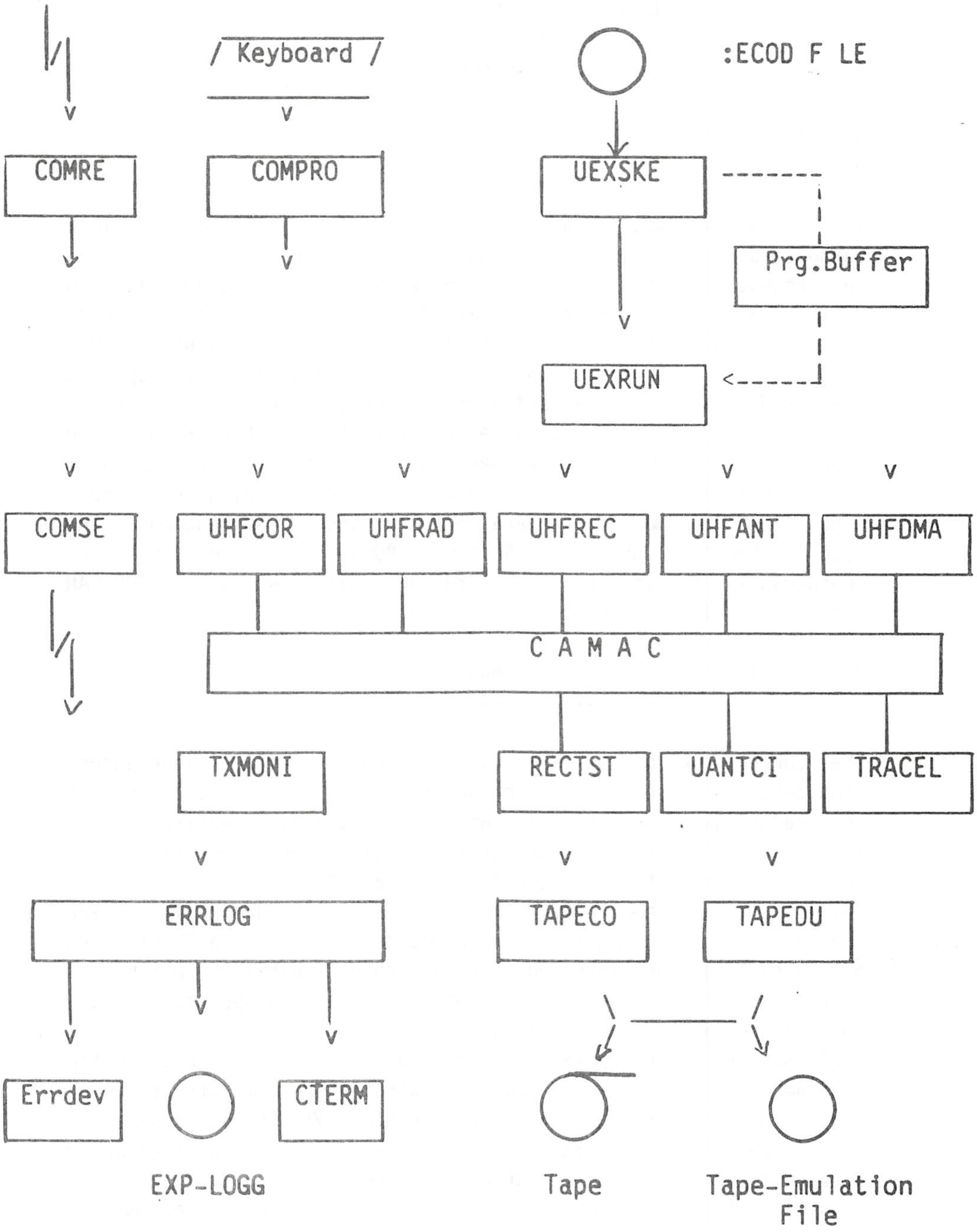

Figure 1.

sites and devices according to the nature of the message.

EROS incorporates 3 logging devices: the command terminal screen, the error printer and an experiment log file on disc. This file is automatically written to the data tape before this is disconnected from the system.

Command structure:

The format of the commands is identical for both the interactive mode and the pre-compiled version. A command consists of 4 parts: the destination site specifier, the system specifier (UHF or VHF), the command itself and parameters where applicable. Each command part can be abbrevated or omitted as long as the remaining command is unambiguous and still meaningful. Nearly all parameters have default values and can be replaced by comas. Command parts may be separated by spaces, parameters by spaces and/or comas. Inside the experiment control files additional comments or site conditional compiler commands can be used. Instead of numerical command parameters predefined variable names can be used, where the content of the variables may be redefined at any time inside the file or during an experiment.

Command example: REMOTE(A) UHF-POINT-REFERENCE-HEIGHT 178,68.6,275 will point the UHF-antennas at all 3 sites so that their lines of site intersect at 175 km altitude, while the Tromso beam is pointing at 178 degrees azimuth, 68.6 degrees elevation

This command could be abbrevated down to

R(A P--H 178 60.6 275 leaving all unneccessary characters out.

C. Hardware Access Groups:

1) Antenna

The UHF antenna is controlled by two motors for azimuth motions in the range of 90 to 630 degrees (east to west 1.5 complete rotations) and two motors for elevation motions in the range of 1 to 93 degrees. The antenna can be moved either by separate manual controls for azimuth and elevation at the Antenna Control Unit (ACU) or by transferring the wanted azimuth and elevation values from the computer into the ACU. Once reached the final position is maintained actively by the 2 motors working against one another thereby compensating for possible wind effects. The actual position is encoded to a precision of 0.005 degrees in each direction.

As the orientation and the mechanical precision of the antenna are not good enough for tristatic measurements, the intended position values have to be corrected first with an offset function before they can be transferred to the ACU. The offset is derived about once a year at each site by measuring the actual positions of a set of radio stars.

The antenna control unit can be accessed from the computer via a CAMAC interface. The intended azimuth and elevation values can be written into the ACU which starts the antenna motion. The current antenna position can be read back at any time from the computer even if the ACU is in MANUAL or STANDBY mode. Additionally some status

Antenna Control System

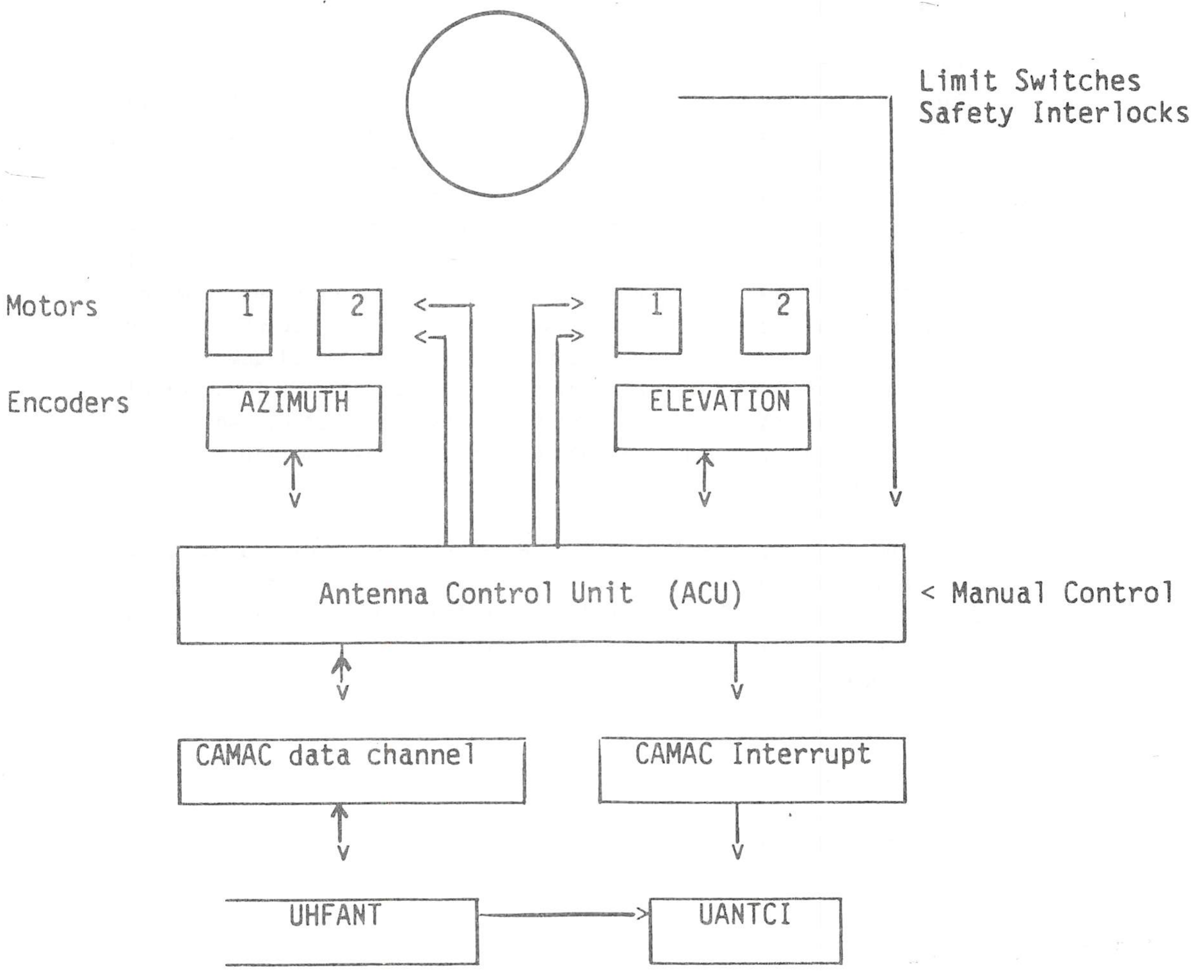

Figure 2

information is transferred with each read process. When the antenna reaches its position an interrupt is issued to the computer.

With EROS the intended antenna direction can be specified in many different ways. The most straight forward way is to use the command POINT-UNCORRECTED which takes the specified AZ and EL values directly without any corrections. All other commands apply the said offset correction before the values are transferred to the ACU. The AZ and EL position values displayed at the controlunit front panel will therefore always deviate slightly from the specified parameters.

The available fraimes of reference are (AZ,EL), (AZ,EL,HEIGHT) or (AZ,EL,RANGE) specified from any location. Preprogrammed reference sites are Tromso (default), Kiruna and Sodankyla antenna locations. If the reference site is identical with the local site the 3rd parameter is meaningless but should be included for convenience. Additionally a geographic frame of reference can be used (LAT,LONG,ALTITUDE).

In bistatic experiments the signal path length depends on the antenna position. To simplify the receiver synchronization the RT-clock in Kiruna and Sodankyla is delayed automatically with each antenna command. The timing can therefore be treated as in the monostatic case.

For radioastromony measurements a subsystem is included in the EROS antenna access part which allows the pointing at radiosources at a given time or the tracking of them. The objects may be specified by names, if they are included in the catalogue of known stars, otherwise their coordinates according to the Astronomical Almanac can be used. A special case is the pointing at the Polestar as it is time independent and is internally translated into an (AZ,EL) command with AZ=0 and EL=site latitude.

2. Receiver Chain

The receiver part begins at the antenna horn, after which for calibration purposes a single frequency can be injected to check the system against 180 degrees phase shifts (Doppler calibration). This source can be activated via EROS for test measurements. For safety reasons it is switched off when EROS is started or an experient is stopped by a command.

An additional white-noise source for power calibration can be connected either via a command from EROS or under the control of the radar controller program (default).

In Tromso these components and the rest of the receiver system can be disconnected from the antenna via the receiver protection switch while a signal is transmitted. This switch is controlled from the radar controller.

The antenna provides both a horizontal and a vertical component of the received signal which are separately amplified. At the remote sites they are then combined in the polarizer to match the received signal to the transmitted circular polarized wave. The two output signals X and Y are phase shifted by 90 degrees. In Tromso this is not needed, the polarizer therefore is removed, and only the X-channel is connected to the UHF antenna.

After the polarizer (or pre-amplifier) the received signals are mixed with a frequency provided by the Local Oscillator 1

Receiver Control System

```
                                    --------------------
                                    !_    ANTENNA      _!
                                      !_     HORN    _!
DOPPLER-CALIBRATION   -------------X    _!
(933.5795 MHZ)                        !________!
                                    (H)!  (V)!
RF-SWITCH --X     !------!              !     !
             X->! ATTN !------X-----X
CALIBRAT. --X     !______!              !     !
                                        !     !
                                    !--------------!
                                    !    PRE-      !
                                    !  AMPLIFIER   !
                                    !______________!
                                        !     !
                                    !--------------!
                                    ! POLARISERS   !
                                    !______________!
                                        !     !
OSCILLATOR                          !-----! !-----!
1053.5 OR 813.5   --------->! MIX !-! MIX !
(CALLED LO1)                        !_____! !_____!
                                       !       !
                                       !       !
                                      (X)     (Y)

     !                                              !
     !                                              !
!-----------!                              !-----------!
!    (X)    !                              !    (Y)    !
!___________!                              !___________!
      !                                         !
!-----------!                              !-----------!
!ATTENUATION!   SIGNAL ATTENUATION   !ATTENUATION!
!___________!                              !___________!
      !                                         !
!-----------!                              !-----------!
!  DIVIDER  !                              !  DIVIDER  !
!___________!                              !___________!
  ! ! ! !                                     ! ! ! !
  1 2 3 4                                     1 2 3 4
  ! ! ! !                                     ! ! ! !
!------------------------------------------------------!
!. . . . . . . CHANNEL SWITCHING . . . . . . . . . !
!______________________________________________________!
  !     !     !     !     !     !     !     !
  1     2     3     4     5     6     7     8
  !     !     !     !     !     !     !     !
```

Figure 3

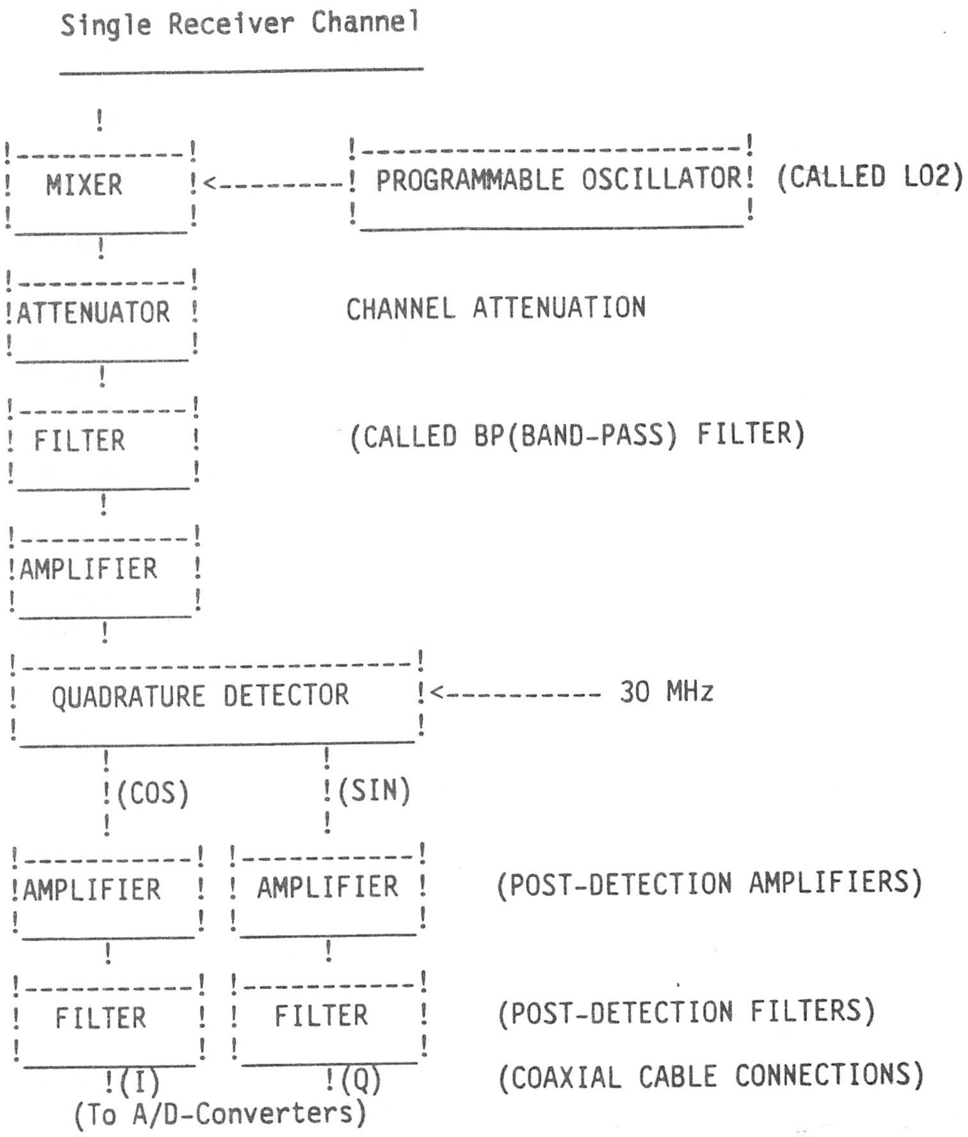

Single Receiver Channel

Figure 4

(L01). The difference signals are then sent to the control room receiver rack. The L01 frequency can be changed by command for special applications, default frequency for UHF experiments is 1053.5MHz. In Tromso the free Y-channel is connected to the L01 of the VHF system thereby making the complete UHF receiver system also available for VHF experiments.

The amplification of each signal path can be changed independently via logarithmic attenuators. With the signal-path selection the final connection between the X/Y channels and the 8 independent receiver channels is made: ALL X, ALL Y, interleaved odd channel numbers to X and even channel numbers to Y (STRAIGHT THROUGH) or vice versa (CROSS). In Tromso the ALL Y selection is interpreted as VHF experiment; accordingly the VHF relevant antenna and transmitter parameters are recorded on the tape along with the data. All other selections will give the UHF parameters.

For each channel the signal is again mixed with a local oscillator (L02) selecting the actual transmitter frequency to observe. Further attenuation of the channel signals allows balancing of channels against one another. A last mixing stage with a fixed 30MHz frequency and a quadrature detector provides a complex signal in a frequency range which can be sampled by the following A/D converters. A post-detection filter determines mainly the available signal bandwidth and shape and has to be selected according to the experiment: filter characteristic and bandwidth can be modified, the first by exchanging the filter modules, the other by EROS commands. EROS knows the possible filter type/bandwidth combinations and checks, if the selected filter is really available in that channel.

3) Radar Controller

The radar controller is the timing center for the measurements. It has its own time basis which at the beginning of each integration periode is synchronised with the second pulses of the RT-clock. Its basic time unit is 1 microsecond. The main parts are:

- a 4k deep instruction memory for 16bit wide instructions and a time control memory of the same size, both accessable for write and read (verification) from the computer
- a time control unit which synchronizes the start of each integration periode and initiates a command fetch at the specified time
- an address logic which fetches the next available instruction and includes a loop counter which determines the end of an integration period when the program cycle has been completed as often as the computer defined scancount value defines
- the transmitter and receiver output drivers, multiplexed under control of bit 14 in the instruction word

The purpose of the different control lines is given in the diagram. Whenever the radar controller is idle between the end of the last cycle of an integration time interval and the synchronised start of the next one. The computer can reprogram the address logic with a new first and last program step address for the next cycle. This can be used to store more than one program in different parts of the controller memory, and then to change between them inside a few miliseconds instead of having to reload the complete program. The corresponding address management is handled by

Radar Controller

	Transmitter Control Lines	Receiver Control Lines
0	- - - - - - - - - - - - - - -	Start Sampling ADC CH 1
1	Transmitter Frequency Ctrl	- " - ADC CH 2
2	4-bit code for F0..F15	- " - ADC CH 3
3	- - - - - - - - - - - - - - -	- " - ADC CH 4
4	UHF-Phase-Ctrl '0'/'180'	- " - ADC CH 5
5	Checkpulse for Oscill.trigger	- " - ADC CH 6
6	Local-Oscillator-Protect ON	- " - ADC CH 7
7	VHF-Phase Ctrl 2-bit:	- " - ADC CH 8
8	- 0/90/180/270 -	Kir/Sodank: Horiz.NoiseInj
9	-not assigned-	NoiseInj (Kir/Sodank: Vertical)
10	-not assigned-	StartCompute to Correlator
11	RF ON	Matched Filter System Active
12	Beam ON	Buffer Address Flip
13	Receiver Protection ON	Spectrum Analyser Programming or free for other purposes

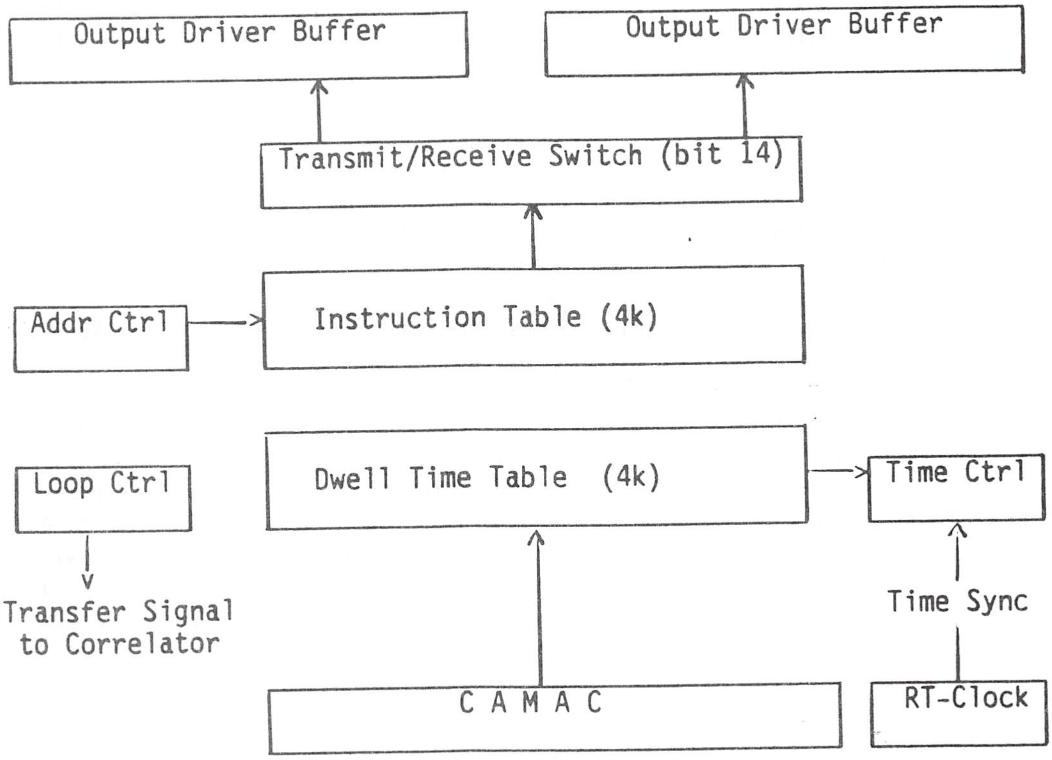

Figure 5

EROS after the related TARLAN compiler has provided the necessary informations along with the compiled version of the program. The user only has to specify the unmber of the new program and the program will change at the end of the current integration time.

EROS translates the integration time into a loop counter value which corresponds to the maximal number of program cycles fitting into the specified integration time. The needed data transfer time is taken into account. This loopcounter value is transferred into the controller together with the program address specifications and could be changed at the same time.

Before the radar controller is started for the first time the start command should be given at least 5 seconds in advance, this time delay has to be specified in the command. If the available time is too short EROS calculates itself the next possible start time using the integration time information. The operator could also specify an absolute start time or use the automatic calculation procedure mentioned above thereby skipping the delay parameter. This is especially useful after problems, as then the tri-static relative time is kept. The default value for the program name is always the last one used, so that a reloading and restarting can be performed without knowledge of any of the actual parameters.

In Tromso it is not possible to stop the radar controller via EROS as long as the transmitter is on. After an experiment the controller has therefore to be stopped with a separate command after the transmitter has been switched off.

TARLAN compiler

The radar controller is a micro coded device where in order not to endanger the equipment some restrictions have to be observed. For this purpose a compiler was developed along with a simpel control language Transmitter-And-Receiver-LANguage (TARLAN). The compiler basically provides a mnemotic code for each output line or line group of the controller, checks that only valid line combinations are used at any given time and allows a sequential absolute time scale for all instructions, whereas the controller itself works with time differences between successive instructions (dwell times). The compiler accepts symbolic files written with an editor program and provides a listing along with errors or warning information. If no serious errors are found an object code file is produced with the file type :TCOD, a listing of the decoded object file can be optionally produced.

The allowed commands have one of the following formats:

```
AT <time> <instruction> (<instruction> ...)  (%<comment>)
SETTCR  <new time bases>
%<comment>
```

All time specifications are in microseconds and must be given in increasing order, after the currently valid time basis is added. The smallest allowed value is 1. No two identical times are allowed. The SETTCR is for programming conveniences only, the compiler itself works only with the complete absolute time.

<instruction> can be any of the available mnemotic codes, no parameters exist. One time specification can be followed by as many

TARLAN Compiler Language

Format:

1) AT <TIME> <INSTR1> (,<INSTR2>)
2) SETTCR <TIME>   % SET TIME CLOCK RELATIVE
3) % <COMMENT>

Transmitter Instructions:

TRANS	Routes the following instructions to transmit-system.
RXPROT	Turn receiver protect on.
RXPOFF	Turn receiver protect off.
BEAMON	Turn klystron beam on.
BEAMOFF	Turn klystron beam off.
RFON	Turn on the RF.
RFOFF	Turn off the RF.
LOPROT	Switch on the local oscillator-protect.
LOPOFF	Switch off the local oscillator-protect.
PHA0	Select phase 0
PHA180	Select phase 180 degrees.
F0 .. F15	Select frequency to transmit. (Fn = 929.5 MHz + n*0.5 MHz)
CHQPULS	Make a 2 microsecond trigger-pulse for scope.
VHF-PHAx	Select VHF phase 0,90,180 or 270

Receiver Instructions:

RECEV	Routes the following instructions to the receiver system.
CH1..CH8	Start sampling on the selected channel.
ALLON	Start sampling on all channels.
CHxOFF	Stop sampling on channel x (x=1..8)
ALLOFF	Stop sampling on all channels.
CALOFF or CAL0	No calibration.
CALON (or CAL100)	Calibration noise injection on (T=210K)

(In Kiruna and Sodankyla: CALON or CAL30: noise inj. to horiz.
CAL100: noise inj to vertical channel, T=30K)

STC	Generate a START-COMPUTE signal to the A/D-converter.
BUFLIP	Flips the correlator buffer-memory. Must be issued between 30 and 50 microseconds after the last channel has stopped samling.

-- Correct time sequence: STC +5 ALLOFF +35 BUFLIP >+4 REP ---

MATCHFIL	Puts the matched filter into RUN-state.
BYPASMAT	Puts the matched filter into BYPASS-state.
REP	Signifies the end of a program (that is the end of the loop).

```
@TARLAN

TARLAN COMPILER    VERSION 3.8 APR 1986

PRINT SOURCE (Y/N) :Y
PRINT OBJECT CODE (Y/N) :Y
OUTPUT TO T(ER),F(ILE) OR L(-P) :L
FOR T(ROMSO) OR R(EMOTE) :T
SOURCE FILE (WITHOUT EXTENSION - :TLAN ASSUMED) :(EXP)CP-3-E-T
FULL FILENAME : (EXP)CP-3-E-T:TLAN
 END-OF-FILE
DUMP (Y/N) : Y
DUMP FILE : (EXP)CP-3-E-T:TCOD
NNNNNN STOP 0
```

Figure 6

```
%%%%%%%%%%%%%%%%%%%%%%%%%%%%%%%%%%%%%%%%%%%%%%%%%%%%%%%%%%%%%%%%%%%%%%%%%%%%%%%%%%
%%
%%  ***  T A R L A N   P R O G R A M M E   F O R   T R O M S O  ***
%%
%%       COMMON PROGRAM CP-3-E
%%
%%       FILE (EXP)CP-3-E-T:TLAN
%%
%%       C. LA HOZ, EISCAT TROMSO, OCT 1985
%%
%%       BASED ON GEN-5 BY TAUNO TURUNEN
%%
%%       LAST ALTERED 6 JANUARY 1986
%%
%%%%%%%%%%%%%%%%%%%%%%%%%%%%%%%%%%%%%%%%%%%%%%%%%%%%%%%%%%%%%%%%%%%%%%%%%%%%%%%%%%
AT 1 TRANS,CHQPULS
AT 10 RXPROT,LOPROT
AT 50 BEAMON
AT 80 F0
AT 100 RFON                          %%  518 US PULSE AT F0 FOR ACF AND REMOTE
AT 618 RFOFF,F1                      %%
AT 620 RFON                          %%  518             F1
AT 1138 RFOFF,F4                     %%
AT 1140 RFON                         %%   98 US PULSE AT F4 FPR POWER PROFILE
AT 1238 RFOFF,F5                     %%
AT 1240 RFON                         %%   98             F5
AT 1338 RFOFF,F6                     %%
AT 1340 RFON                         %%   98             F6
AT 1438 RFOFF,F7                     %%
AT 1440 RFON                         %%   98             F7
AT 1538 RFOFF,BEAMOFF                %%
AT 1900 RXPOFF                       %%
AT 1950 LOPOFF                       %%
AT 2000 RECEV                        %%
                                     %%
AT 2682 CH1                          %% START SAMPL SIG  PP AT RANGE 225 KM
AT 2782 CH2                          %% START                        225
AT 2882 CH3                          %% START                        225
AT 2982 CH4                          %% START                        225
                                     %%
AT 3271 CH5                          %% START SAMPL SIG ACF AT RANGE 481 KM
AT 3791 CH6                          %% START                        481
                                     %%
AT 5195 CH1OFF                       %% STOP  SAMPL SIG  PP AFTER 180 SAMPLES
AT 5295 CH2OFF                       %% STOP                      180
AT 5395 CH3OFF                       %% STOP                      180
AT 5495 CH4OFF                       %% STOP                      180
                                     %%
AT 7910 CH7,CH8                      %% START SAMPL BAK ACF FOR PREVIOUS PHASE
                                     %%
AT 8934 CH5OFF                       %% STOP  SAMPL SIG ACF AFTER 405 SAMPLES
AT 9454 CH6OFF                       %% STOP                      405
                                     %%
AT 9460 CH1,CH2,CH3,CH4              %% START SAMPL BAK  PP FOR THIS     PHASE
AT 9790 ALLOFF,CAL100                %% STOP             PP AFTER  24 SAMPLES
                                     %% STOP            ACF FOR PREVIOUS PHASE
                                     %% TURN  ON  CAL NOISE INJECTION
AT 9850 CH7,CH8                      %% START SAMPL CAL ACF FOR PREVIOUS PHASE
AT 9900 CH1,CH2,CH3,CH4              %% START            PP FOR THIS     PHASE
AT 9980 CH1OFF,CH2OFF,CH3OFF,CH4OFF  %% STOP             PP AFTER   6 SAMPLES
AT 10680 CH7OFF,CH8OFF,CALO          %% STOP            ACF FOR PREVIOUS PHASE
                                     %% TURN  OFF CAL NOISE INJECTION
AT 12000 REP
```

Figure 7

instructions separated by comma or space as a 80 character line can hold.

Transmitter and receiver instructions cannot be mixed. Between some instructions certain minimum or maximum time limits have to be observed. As the hardware would not work if these restrictions are violated they are treated as serious errors no executable object file will be produced.

A program has to be terminated with the instruction REP. All following lines are considered as part of a new program. In this way up to 20 programs can in this way be included into the same file.

4) Correlator

The correlator system consists out of 4 parts which may or may not reside in the same crate.

The analog signals of each channel are converted to signed 8 bit digital values (-128..+127), one for the real part, one for the imaginary part. The first sample is taken when the radar controller commands the start sampling for that channel, the sampling then continues in the intervals defined via EROS until it is again stopped by the radar controller. For each channel a start address in the buffer memory has to be defined. This address is attatched to the data pair and incremented with each sample. It is the responsibility of the experiment designer that the address spaces of different channels don't overlap. The data for channels 3-8 are transferred directly into the buffermemory via one common data bus. Channels 1 and 2 with higher possible conversion rates have their own buffers, whose content along with the buffer memory addresses are transferred after the sampling on all channels has stopped.

Between ADC sets and buffermemory a matched filter decoding device can be included on command of the radar controller. If the decoder is active all data from the ADC's have to be phase coded with the same code. As the data transfer from channels 1-2 and 3-8 are separated in time it is possible to use one group for phase coded signals and the other for uncoded ones.

The buffermemory contains 2 identical halves with the same address space. While one half can be written to from the ADC's, the other half can be read by the correlator processing part. The meaning of these halves is changed by the radar controller instruction BUFLIP. The channel dependent buffermemory start adresses are not used inside the memory unit itself but rather provides the ADC unit with the correct start address values after each BUFLIP command.

The correlator is a pipeline processor with 128 bit wide instruction words and is able to combine any 2 values in the buffermemory and add the product in different ways. 2 identical processors are able to process the real and the imaginary part of the data simultaneously. Up to 63 instructions can be loaded from the computer each of which is capable of handling complex control tasks. The actual behaviour of the program can be modified by a set of 2x16 registers which can be independently set via EROS. The programs themselves can be written using the CORLAN compiler which provides mnemotics of the different instruction sub groups and takes care of some correlator logic interactions. Normally ready programs are used.

Correlator and ADC's

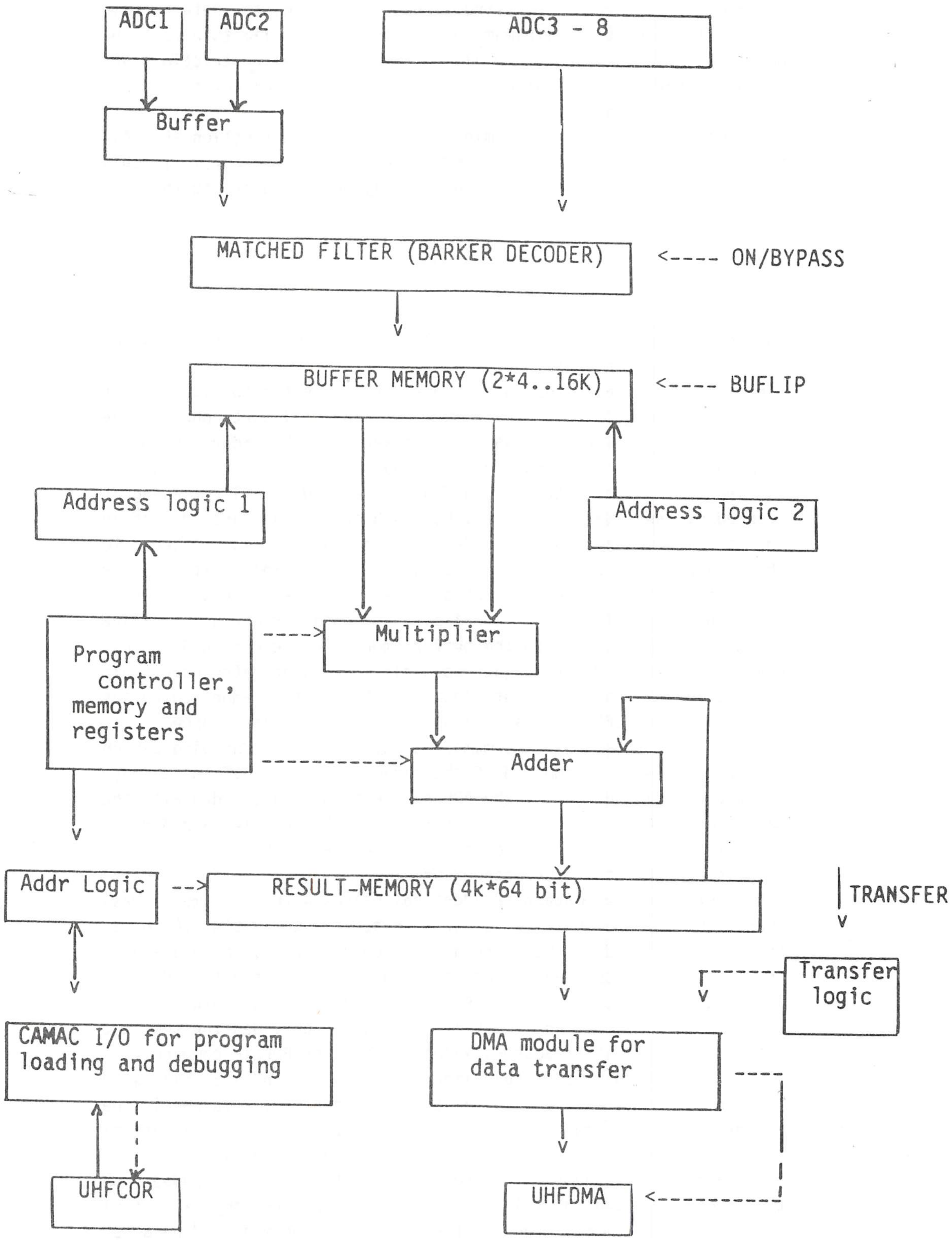

Figure 8

The products are accumulated in the result memory and on the radar-controller transfer command sent via a DMA channel into the computer.

EROS checks the program file for consistency before it loads it into the correlator program memory. No verification is possible as the memory cannot be read back into the computer. The complete transfer takes about 1 sec, the file access including test about 3 seconds. If necessary these two processes may be separated, using explicitly the FETCH-CORRELATOR-PROGRAM command before the LOAD command is issued. Later reloading skips the file access as the program is kept in memory. The contents of all registers used by the program have to be explicitly specified. These values are not transferred into the correlator itself until the START-CORRELATOR command is given. Then the complete register content is overwritten (those registers not specified will have the value 0). Each register keeps its defined value inside EROS until the next time EROS is started! The values written into the correlator and possible modifications made since then can be checked whith the PRINT-CORRELATOR-STATUS command.
The content of the registers could already be specified from inside the correlator program itself thereby initializing them to some working combination. This can also be checked with the PRINT command if this is given after the loading but before the first SET command. To start the correlator with these default values RESET-CORRELATOR must be used instead of the START command.
To modify only certain registers, an UPDATE command is available and it has to be followed by the RESET command again.

5) Data Recording Control

The experiment data are finally all written to a magnetic tape. Before they get there a DMA control program prepares the DMA channel(s) from the correlator(s) telling the interface how many data to expect. Following the radar controller transfer signal the correlator transfers this amount from the result memory into a predefined area of the computer memory. The number of 64 bit words (sent in 16 bit parts) is defined by the EROS command SET-CORR-DATAIO and is loaded into the correlator together with the START command. Once the number of data has arrived the DMA interface issues an interrupt to the DMA control program which then starts with testing the data for formal correctness. An inbuilt watch-dog feature will also activate the program if the signal is delayed by more then 1 second.
Tests are performed on the correct number of words transferred, on correct status information from the correlator, and on the correct loopcounter values, one for each of the 2 parallel processors in the correlator (real/imag). Any detected deviations are reported. If the correlator status indicates problems, the DMA program sends a RESET instruction to the correlator. If that even after 10 repetitions does not help the program initiates automatically a complete reload/start cycle. Should even this fail the program will stop, and no further data will reach the computer.
If the data are found to be formally correct the tape formatting

and transfer program is activated, which in order to release the main data transfer area will copy the complete data set along with its descriptor (parameter block with the most important experiment parameters at that moment) into a separate memory area. Then the data are blocked into 2k 16bit words including some organisational information at the beginning of each block. If one block is full it is written out to the tape. The program also keeps track of the available amount of tape, issueing a request for a new tape when only 75 ft are left.

The tape management and execution of tape related commands is done by a separate control program with lower priority. It takes care of accepting and initially testing a new tape (MOUNT) thereby preventing the accidental overwriting of previous data. While no data transfer is going on, the program can transfer text files to the tape, using the same blocked format than for data. Any data recording has to be activated via the control program and can also be stopped from there. Additionally file marks can be forced into the data stream to make the later access of data easier. If the transfer routine or the control program finds out that there is no tape left the control program stops the recording, transfers the logfile to the tape and then tries to find a new output device. If one is available it will automatically continue there. For emergencies a part of the disks is set aside to serve as an intermediate storage medium treated like a normal tape.

C. Experiment Control

In order to do an experiment with the EISCAT radar, the used hardware parts have to be initialized with the intended parameters, then activated at the proper time or de-activated when needed. This could be done by an experienced operator issueing manually the needed EROS commands. The safer way is to write all the commands in the ELAN language (Experiment control LANguage) with an editor program into a computer file. A compiler (ELAN-Compiler) then checks for correct syntax and valid parameters, produces an object file and gives an overview over the timing conditions. A listing can optionally be printed. The line numbers of the listing are displayed during program execution and are also written with the parameter block onto the tape to keep track of the program part which collected the data.

1) Absolute and Relative Timing

An important part in multi-station experiments is the time synchronisation. The basic time unit for experiment supervision under EROS is 1 second, derived from the computer clock. This is synchronized with the cesium standard of the radar. The data taking starts with the start of the radar-controller. This is the only part which requests a higher time precision. EROS handles this problem by issuing at an absolute time of the day - precision 1 sec - a start command with an inbuilt time delay of a few seconds. The radar controller then starts synchronised with the corresponding second pulse of the RT-clock which by itself runs with 1 microsecond precision. Apart from radioastronomy experiments this is the only hardware access command which can be given with an absolute time from the command terminal. In all other standard cases the absolute time of command execution is: for manual commands the moment the command is given, abd for commands inside an experiment file the time relative to the start of the experiment. The experiment can be started at any absolute time inside the current and the following 4 days.

Inside the ELAN file all time specifications are relative to the absolute time as specified with the start of the experiment. There are 2 timing commands: SYNC and HOLD, both with a time delay parameter in seconds. On start of an experiment the experiment time is initialised to the specified start time, then the compiled version of the ELAN file (type :ECOD) read and the instructions executed sequentially as fast as the involved RT programs manage. As each RT program has its own command buffer this can mean that instructions are not necessarily executed in the order they were originally specified. For the initialization phase of an experiment this is unimportant and it only speeds the overall task up as all resources are optimally used. Later during the experiment one has to keep this fact in mind to avoid problems, though in most cases EROS is designed in a way that it recognises such conflicts itself and provides some additional hidden synchronization means.

The experiment time is completely ignored until one of the two timing commands is encountered. Thus it is possible to check the availability of software and hardware parts ahead of time in the configuration needed for the experiment. Recognised problems may still be corrected before the actual start time is reached.

With each timing command the parameter is added to the experiment time, and the result compared to the current computer time. If the time is not yet reached, the program execution will be suspended, the resulting waiting time displayed on the command terminal. If the computer time is already later then the two commands behave differently: the SYNC command will be ignored, the HOLD command leads to a pause of the specified amount of seconds regardles wether the experiment time slips even further behind the current time or not. This allows to prevent the system from executing too many commands at once e.g. during heavy CAMAC accesses while loading radar controller or correlator. Normally this does not matter as the actual time should always be earlier or equal to the experiment time. In case of a delayed start the runtime system can rush through major parts of the program without a single stop until it eventually catches up with the correct time.

All instructions between two successive SYNC or HOLD commands are executed simultaneously,i.e the actual order of execution depends on the status of the system and can normally not be predicted by the user. One exception exists: commands concerning the same hardware are always executed in the order in which they are given.

As most programs are somehow cyclic repeating the same sequence of instructions over and over again (outermost DO LOOP) the runtime system optimizes late starts by internally adjusting the experiment time so that it somewhere inside the first loop will reach the computer time. Even on starts delayed for hours the original start time can therefore be specified. If an experiment had to be interrupted the operator can select the time adjustment strategy: either to start directly and catch up in the current cycle or wait until the beginning of the following cycle. No further parameters are then needed as they are already known to EROS.

If you want to start the experiment data gathering at a even time and still have time enough to prepare the hardware and the tape then a convenient way is to use a negative time parameter for the first file time instruction: SYNC -120 gives 2 minutes time. The experiment control will continue with the following instructions 2 minutes before the specified experiment start time. If the sum of all following time parameters including the radar controller start delay equals to the absolute value of this negative SYNC the data taking will start exactly at the specified start time. As a guide the ELAN compiler prints already the value of a negative SYNC, if any, and the sum of all the following delays up to the first radar controller start command.

2) Experiment Flow Control

Normally all instructions are executed in the order in which they are found in the program. For convenience or flexibilities sake this can be changed by special instructions inside the program or by the operator with a manual command.

DO / ENDDO: This is the most common flow control command: after the ENDDO instruction the execution continues with the next instruction following the corresponding DO statement. The DO control variable determines how often the loop should be executed. Nesting of loops is possible. Special features: DO -1 is an infinit loop which can only be left by other flow control commands, DO 0 means skip all instructions up to and including the corresponding ENDDO. As the DO parameter can be an internal variable this enables the including or omitting of program parts during experiment time under the control of the operator or in highly complex experiments even under program control.

LIMIT: an infinit loop can be changed into a finite loop with this command allowing e.g. an exact stop of the experiment at the end of one cycle.

GOTO: the experiment continues with the instruction marked with the corresponding BLOCK label. Used from the command terminal this can be used to change the experiment directly if more than one experiment is written into the same file. If this command is given as a remote command an absolute time for execution can be specified to allow the commands to arrive at all involved sites and change the command flow synchroneously.

CALL-BLOCK: this is only allowed insides an ELAN file and treats an instruction set enclosed in BLOCK <n> / RETURN commands as a subroutine. The execution after the RETURN will continue following the CALL command. Nesting is possible.

STOP-EXPERIMENT: the program execution stops, all devices are reset, the data recording stops also. In effect after stopping the execution of the experiment file a short system experiment with the name FINISH:ELAN is started which resets the system. Its content may change from site to site and with time. The stop can be scheduled, i.e an absolute stop time can be specified in advance when the current expériment shall be stopped. As additional to the active experiment another experiment can be scheduled, the STOP command can be used to change an experiment at a pre-defined time. If no experiment is active the command can be used to reset the system as it is then equivalent to a start of the experiment "FINISH"

3) Remote Control

Nearly all commands can also be sent to any combination of EISCAT sites including the own local site. This allows the control of the complete system from one site, even if there is no one at the other sites. Remote commands are always confirmed from the addressed site if they are successfully executed. Otherwise an error message is sent back.

For communication EROS provides its own message system allowing operators at different sites to exchange informations. The sending time is automatically attached to each line, the messages appear also on hardcopy in case the operator overlooks it at the screen.

Important messages to all sites can be sent via broadcast, a single stroke command followed by the message which will automatically be rooted to all sites and there written to all output devices of EROS. Automatic broadcasts are issued from Tromso whenever the transmitter starts or stops during an experiment.

D. Experiment Monitoring

1) Automatic Monitoring

All RT programs included in the EROS system check if the commands given from any source are executed correctly. Any detected errors are directly reported to the local site command terminal, in severe cases also to the hardcopy and the log file. Additionally the remote site issuing a command is informed about the error, otherwise the correct command execution is confirmed. If during an experiment the oparator issues a command which can influence the performance of the experiment a confirmation is also given locally and written to the error device and the log file to have later a complete record of system changes.

Additionally some tests are performed automatically and independent of commands: Whenever the computer is up the transmitter status and the status of the heating facility are monitored in regular intervals of a few seconds. After start of an experiment the test intervals are shortend to 2 seconds. During data transfer the status of the involved equipment is checked with every dump: correlator and radar controller performance, tape recording, available tape left etc.

Any problem encountered is reported. Partly EROS tries to cure the problem itself to allow unattended experiments at the remote sites for as long periods as possible. If the problems cannot be cured the staff is alerted, in Tromso via a software alarm bell, in Kiruna and Sdankyla by automatically calling the stand by operator at home. There remote access via modem allows diagnostics and partly also the cure of the problem.

In between data transfers the complete receiver system is checked, found deviations from the intended settings are reported. Whenever an antenna command is given the antenna control unit is checked in 2 second intervals until the antenna is in the intended position.

The communication system is tested about 3 times per minute if no remote information is exchanged inbetween. Any detected communication error is reported to all sites still connected so that EROS at each site knows if remote commands can be transferred successfully: on communication errors remote commands to that site are rejected to prevent overloading of the system. EROS itself tries to establish the connection again.

2) Monitoring by Operator

For experiment supervision EROS offers a set of status print commands each addressing one part of the system. Additionally a compressed status overview is available with the command PRINT-STATUS. For each system part it says OK or ERR, additionally the experiment name (if any) and the amount of tape left is displayed. If an error is indicated the operator should check the corresponding group with the more detailed status request. The most important status informations besides the overview are the PRINT-DMA-STATUS and the PRINT-TAPE-STATUS command. Given twice with the integration time inbetween it shows if the data transfer to the tape is still ok: the sequence numbers should increase from one dump to the next. The correct setting of the LO2's can be tested with the DISPLAY-LO2 command: a frequency counter is then connected to the selected channel and visualises the used frequency, the oscilators themselves can only be checked if they are in computer mode or not, but not read back into EROS.

For more transparency the tracing of the experiment instructions as they are executed can be switched off. Any antenna position change will still be displayed. If more information is wanted on a regular bases, special comments can be used inside the ELAN file. If internal parameters are used and changed their current value with an explaining text can be displayed on the command terminal by including the instruction DISPLAY-PARAMETER into the file

3) Logging of Important Events

Important information concerning either the experiment performance or the geophysical conditions can be recorded in the logfile by the operator and will thereby afterwards accompany the data to their user. This may even be done with the already mentioned broadcast. These informations should also be noted down on the Experiment Summary Form which can make the processing work easier as one has not to read the tape first to find the information.

4) Graphical Monitoring

The most detailed information about the data quality and possible experiment problems are obtained with the graphical monitoring program RTGRAPH. Started from any TEKTRONIX compatible terminal with the command RTGRAPH it displays the measured ACF's and power profiles and allows background subtraction, spectrum display and postintegration of data. Also some alphanumerical information is given about the experiment performance. In Tromso estimates of some

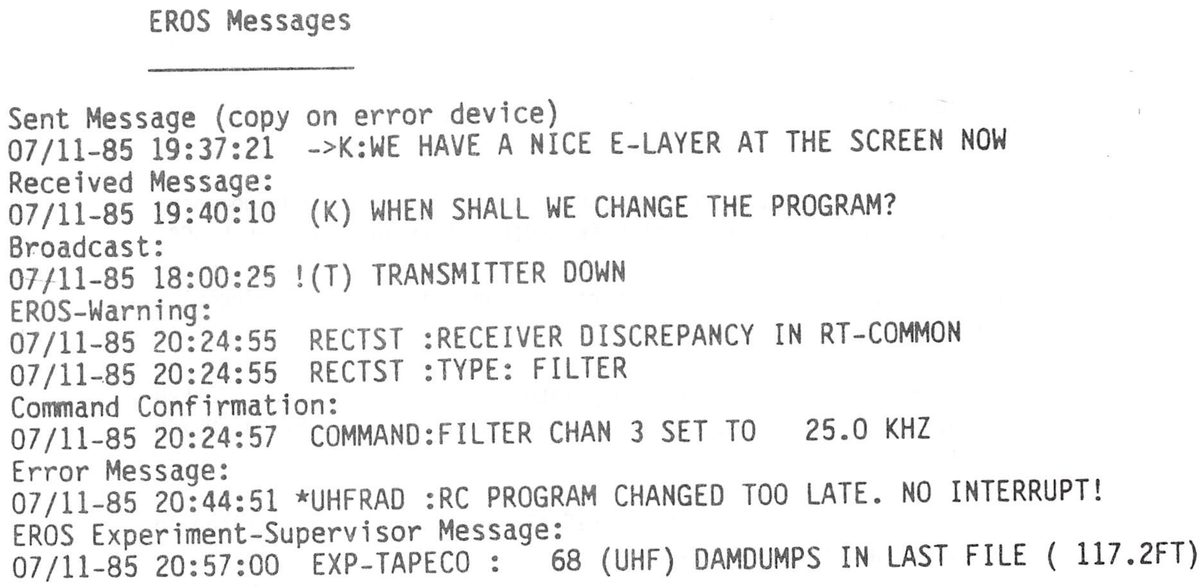

```
          EROS Messages
          _____________

Sent Message (copy on error device)
07/11-85 19:37:21  ->K:WE HAVE A NICE E-LAYER AT THE SCREEN NOW
Received Message:
07/11-85 19:40:10  (K) WHEN SHALL WE CHANGE THE PROGRAM?
Broadcast:
07/11-85 18:00:25 !(T) TRANSMITTER DOWN
EROS-Warning:
07/11-85 20:24:55  RECTST :RECEIVER DISCREPANCY IN RT-COMMON
07/11-85 20:24:55  RECTST :TYPE: FILTER
Command Confirmation:
07/11-85 20:24:57  COMMAND:FILTER CHAN 3 SET TO   25.0 KHZ
Error Message:
07/11-85 20:44:51 *UHFRAD :RC PROGRAM CHANGED TOO LATE. NO INTERRUPT!
EROS Experiment-Supervisor Message:
07/11-85 20:57:00  EXP-TAPECO :   68 (UHF) DAMDUMPS IN LAST FILE ( 117.2FT)
```

Figure 9

physical quantities can be calculated (Ne,Te,Ti,v).A hardcopy device allows the direct documentation of interesting events.

E. Documentation

A more detailed description of EROS and the available EROS commands can be found in the EISCAT USERS GUIDE, available at each EISCAT site and EISCAT Headquarters in Kiruna. Here also the VHF control part, the radar hardware, data formats used and the basic principles of the data analysis are described.

The correlator, available correlator programs and the CORLAN compiler are described in the EISCAT TECHNICAL NOTES 81/24, 82/36 and 85/44.

The geometry of the tristatic EISCAT radar system is described in EISCAT TECHNICAL NOTES 79/13.

For further informations please contact the EISCAT staff.

```
%%%%%%%%%%%%%%%%%%%%%%%%%%%%%%%%%%%%%%%%%%%%%%%%%%%%%%%%%%%%%%%%%%%%%%%%%%(10)
%%
%%  ***  E R O S   P R O G R A M M E   F O R   T R O M S O   ***
%%
%%     COMMON PROGRAM CP-3-E
%%
%%     FILE: (EXP)CP-3-E-T:ELAN
%%
%%     EISCAT MARCH 1986
%%
%%     CONTRIBUTORS: KIRKWOOD, LA HOZ, MARKKANEN,
%%                   SCHMIDT, TURUNEN, VAN EYKEN.
%%
%%     LAST ALTERED 31 MARCH 1986, C. LA HOZ
%%
%%%%%%%%%%%%%%%%%%%%%%%%%%%%%%%%%%%%%%%%%%%%%%%%%%%%%%%%%%%%%%%%%%%%%%%%%%%%%
%
WRITE-EXP-HEAD
%
WRITE-FILE (EXP)CP-3-E-T:ELAN
WRITE-FILE (EXP)CP-3-E-T:TLAN
WRITE-FILE (EXP)CP-3-E:DESC
WRITE-FILE (EXP)CP-3-E-T-SUBR:LIST
SET-PARAMETER R01,275.0
%
    CHANGE-REF-SITE TROMSO,,,,
    POINT-REF-HE   5.0,20.0,R01
%
 LOAD-CORR (EXP)GEN-5-T:CCOD          %MASTER PROGRAM GEN-F-L1U1P2:CLAN  OLD CORREC
%
HOLD 30
SYNC -150
%
%
LOAD-RADAR (EXP)CP-3-E-T
%
TRANSF-NOISE-CONT RAD
%
TRACE-OFF                      %% ALL NECESSARY INFORMATIONS ARE GIVEN
%
SET-LO1 1053.5
%
SET-SIG-PAT ALLX
SET-SIG-ATT X,5
%
SET-CH-ATT 1,5
SET-CH-ATT 2,6
SET-CH-ATT 3,4
SET-CH-ATT 4,2
SET-CH-ATT 5,2
SET-CH-ATT 6,2
SET-CH-ATT 7,3
SET-CH-ATT 8,1
%             NOTE:BALANCE THE CHANNELS FOR GROUPS 1,2,3,4 AND 5,6,7,8
%                  BY CHECKING THE ATTENUATOR VALUES BEFORE THE EXPERIMENT.
SET-LO2 5,94.0
SET-LO2 6,93.5
SET-LO2 7,93.0
SET-LO2 8,92.5
SET-LO2 1,92.0
SET-LO2 2,91.5
SET-LO2 3,91.0
SET-LO2 4,90.5
```

Figure 10

(10/2)

```
%
SET-FILTER 1,BUT,25.0
SET-FILTER 2,BUT,25.0
SET-FILTER 3,BUT,25.0
SET-FILTER 4,BUT,25.0
SET-FILTER 5,BUT,25.0
SET-FILTER 6,BUT,25.0
SET-FILTER 7,BUT,25.0
SET-FILTER 8,BUT,25.0
%
SET-CO-APB 15,15       %VOLUMEINDEX
SET-CO-APB 14,15       %LAGMAX
SET-CO-APB 13,25       %LPNOGATES, SCATTER PART
SET-CO-APB  9,210      %PPNOSAMPLES1 (GATING+1=1)
SET-CO-APB  7,7        %USERREG1,LP SKY NOISE GATE NUMBER
SET-CO-APB  6,2        %USERREG2,LP NOISE INJECTION GATE NUMBER
SET-CO-APB  5,0        %USERREG3, PP GATING CONTROL (0=NO GATING)
SET-CO-APB  0,1        %APBINCR
%
%
SET-CO-APM 15,0        %RESENTRY1, POWERPROFILES   (210=180+24+6; SIG+BAK+CAL )
SET-CO-APM 14,210      %RESENTRY2, LP SIGNAL GATES (400=25*16   ; NGATES*NLAGS)
SET-CO-APM 13,610      %RESENTRY3, LP BACK.  GATES (112= 7*16   ; NBAKGR*NLAGS)
SET-CO-APM 12,722      %RESENTRY4, LP CAL    GATES ( 32= 2*16   ; NCAL   *NLAGS)
SET-CO-APM 11,754      %RESENTRY5, SCANCOUNTADDRESS(754=210+400+112+32          )
%
SET-CO-APM  3,15       %LPMAXLAG
%
SET-CO-APM  0,1        %APMINCR
%
SET-CO-DATAIO 755
SYNC 60
%
SET-BUF-M 2,1620
SET-BUF-M 3,2640
SET-BUF-M 4,3660
SET-BUF-M 5,0000
SET-BUF-M 6,1020
SET-BUF-M 7,2040
SET-BUF-M 8,3060
SET-BUF-M 1,600            % MUST BE THE LAST COMMAND
%                          % THE FIRST UNUSED BUFFER ADDRESS 4080
%
SET-ADC-INT 1,14
SET-ADC-INT 2,14
SET-ADC-INT 3,14
SET-ADC-INT 4,14
SET-ADC-INT 5,14
SET-ADC-INT 6,14
SET-ADC-INT 7,14
SET-ADC-INT 8,14
%
START-CORR
SYNC 50
START-RADAR 10,1,10
%
ENABLE-DMA
%
SYNC 10
%
```

cont. Figure 10

(10/3)

```
DO -1
%
SET-PARAMETER I16,518          %% LENGTH OF LONG PULSES
SET-PARAMETER I17,98           %% LENGTH OF SHORT PULSES
SET-PARAMETER I18,4810         %% START-RANGE FOR LONG PULSES
SET-PARAMETER I19,2250         %% START-RANGE FOR SHORT PULSES
SET-PARAMETER I20,1            %% POSITION COUNTER
START-REC-DATA
DISPLAY-PARAMETER I20,POSITION NO
SYNC 110                       %%  0 +110        POSITION 1
%
POINT-R-H  344.9, 20.0, R01
SET-PARAMETER I20,2
DISPLAY-PARAMETER I20,POSITION NO
SYNC 101                       %%  20+90         POSITION 2
START-RADAR 0,2,10
SYNC   9
%
POINT-R-H  344.9, 24.0, R01
SET-PARAMETER I16,476
SET-PARAMETER I17,98
SET-PARAMETER I18,3300
SET-PARAMETER I19,1900
SET-PARAMETER I20,3
DISPLAY-PARAMETER I20,POSITION NO
SYNC 71                        %%  10+70         POSITION 3
START-RADAR 0,3,10
SYNC  9
%
POINT-R-H  344.9, 28.6, R01
SET-PARAMETER I16,434
SET-PARAMETER I17,91
SET-PARAMETER I18,2900
SET-PARAMETER I19,1650
SET-PARAMETER I20,4
DISPLAY-PARAMETER I20,POSITION NO
SYNC 80                        %%  10+70         POSITION 4
%                                 STOP-REC 2 SEC AFTER LAST DUMP
STOP-REC-DATA
%
? MOVING BACK TO POSITION 1
POINT-R-H    5.,   20.,   R01
SYNC 120                       %%  120+00
%
ENDDO
%
STOP-EXPERIMENT,,,,
```

cont. Figure 10